Master of Science Thesis

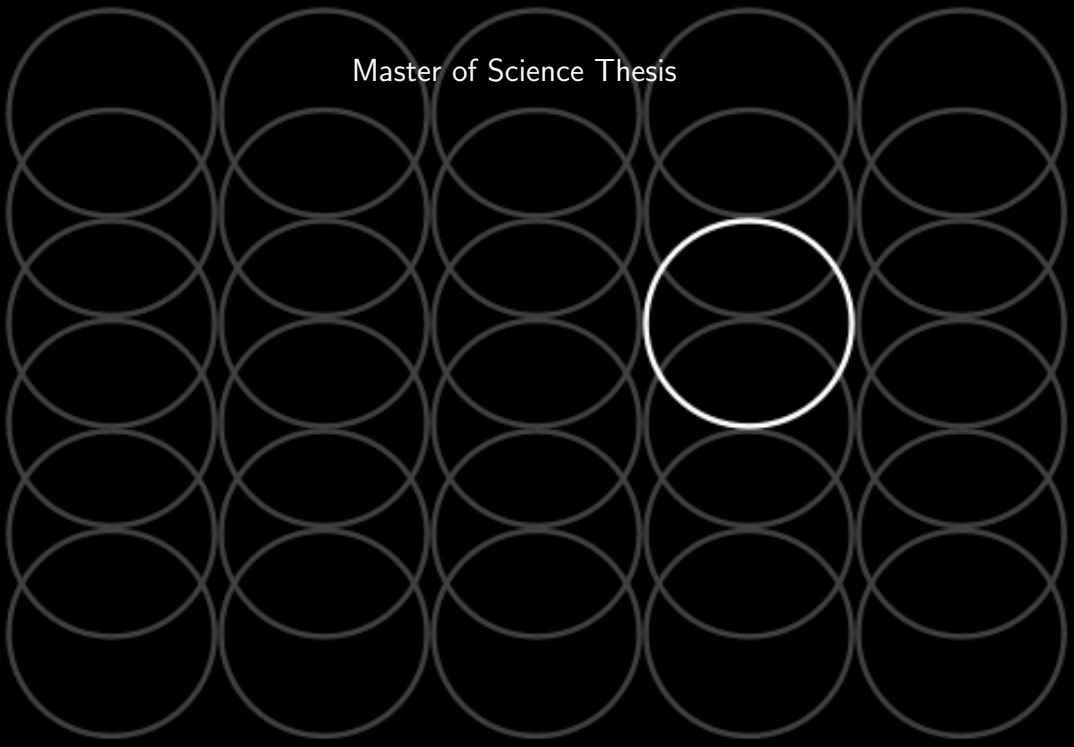

Estimation and reduction of peak-locking errors in PIV measurements

Ankur Kislaya

August 22, 2016

Aerodynamics

TU Delft

Faculty of Aerospace Engineering

Delft University of Technology

Estimation and reduction of peak-locking errors in PIV measurements

Master of Science Thesis

For obtaining the degree of Master of Science in Aerospace Engineering
at Delft University of Technology

Ankur Kislaya

August 22, 2016

Faculty of Aerospace Engineering · Delft University of Technology

Delft University of Technology

DELFT UNIVERSITY OF TECHNOLOGY
DEPARTMENT OF AERODYNAMICS

The undersigned hereby certify that they have read and recommend to the Faculty of Aerospace Engineering for acceptance the thesis entitled **"Estimation and reduction of peak-locking errors in PIV measurements"** by **Ankur Kislaya** in fulfillment of the requirements for the degree of **Master of Science**.

Dated: August 22, 2016

Supervisors:

Prof. Dr. Fulvio Scarano

Dr. Andrea Sciacchitano

Dr. ir. Bart van Rooijen

Dr. ir. Christian Poelma

Acknowledgment

First of all, I would like to express my sincere gratitude to my daily supervisor Dr. Andrea Sciacchitano for his continuous support, motivation, and immense knowledge in the field of measurement errors in PIV. Without his valuable guidance and technical discussions, this thesis would not have been possible. Also my deepest appreciation to my external supervisor Dr. ir. Bart van Rooijen from German Dutch Wind tunnels (DNW). His unwavering enthusiasm for PIV and his eye for details helped me to be more critical of my work.

I would like to thank Prof. Dr. Fulvio Scarano and Dr. ir. Christian Poelma for their insightful comments and encouragement to make this thesis more sound. Also, my sincere thanks to Dr. Bernd Wieneke from LaVision Inc, who provided us with the optical diffuser for wind tunnel testing and for sharing critical information which helped in better understanding of the diffusers.

I am grateful to Alberto, Michel, Fabio, Tanmay, Swaraj and my other friends from TU Delft who helped in making my strenuous graduate life a bit more tolerable and enjoyable.

Last but not the least, no amount of gratitude will be enough for my family who always supported me with my decision to study abroad and for their unconditional love and care.

Abstract

In PIV, the systematic tendency of the measured sub-pixel displacement to be biased towards the integral pixel values is called peak-locking. This occurs when the particle image diameter is less than a pixel. The bias error causes inaccuracy in the measured PIV data which does not reduces with increase in the sample size. Recently developed LaVision's optical diffuser was investigated to determine the reduction in peak-locking. The point-spread-function width of diffuser was examined to calculate the change in the shape and size of the point source under the influence of different parameters. Planar-PIV experiment were carried out in uniform, low-speed and high-speed flow conditions to analyse the effectiveness of the optical diffuser in reducing the bias error and change in the random error. Also, a comparative assessment was done between the use of conventional defocusing and optical diffusers during image acquisition. The use of optical diffusers reduces the bias error and random error by a factor of three. The reduction in the measurement error is similar to the best defocused optical position of the lens which is very difficult to determine. Additionally, an experimental analysis was done with three different camera-lens combination to determine the best relative aperture size for keeping the measurement error minimal for 2D PIV. With the help of optical diffusers, experimentalists can have more accurate PIV measurements which would lead to more realistic capturing of the flow phenomenon. With the use of optical diffusers, it would also help the CFD and theoretical experts to compare their predictions with better experimental benchmark results.

Table of Contents

List of Figures

List of Tables

Nomenclature

Abbreviations

$\bar{d}_{\text{meas}}$	mean measured particle displacement	[pixels]
Δ_t	time separation	μs
δ_z	depth of field	[mm]
ϵ_{bias}	bias error	[pixels]
ϵ_{rand}	random error	[pixels]
η_e	extraordinary refractive index	[-]
η_o	ordinary refractive index	[-]
λ	wavelength	[nm]
μ	dynamic viscosity	[Ns/m^2]
ϕ	relative angle between two diffusers	[deg]
ρ	fluid density	[kg/m^3]
ρ_p	tracer particle density	[kg/m^3]
σ	standard deviation	[-]
τ_p	particle time response	[s]
C	degree of peak locking	[-]
d_τ	particle image diameter	[pixels]
d_{true}	true displacement	[pixels]
d_D	correlation peak width	[pixels]
d_P	actual seeding particle diameter	[μm]
d_p	tracer particle diameter	[pixels]
f	focal length	[mm]
$f_\#$	*f-stop*/f-number	[-]
I_P	average peak intensity	[counts]
IA	interrogation window area	[pixels^2]
M	magnification factor	[-]
N_I	image density	[particles per pixel (ppp)]
q	dynamic pressure	[N/m^2]
R_h	auto-correlation peak	[counts^2]

Re	Reynolds number	[-]
u	velocity component in x-direction	[m/s]
(X, Y)	object plane	[mm]
(x, y)	image plane	[mm]
[A]	mapping function	[-]
[B]	inverse of mapping function	[-]
DVR	Dynamic Velocity Range	[-]
FFT	Fast Fourier Transform	[-]
FOV	Field of View	[-]
HDR	High Dynamic Range	[-]
OA	Optical Axis	[-]
PIV	Particle Image Velocimetry	[-]
PSF	Point Spread Function	[-]
ROI	Region of Interest	[-]
Z_0	object distance	[mm]
z_0	image distance	[mm]

Chapter 1

Introduction

For the things we have to learn before we can do,
we learn by doing.

ARISTOTLE
(384 BC - 322 BC)

In this chapter a general review on fluid dynamics and the motivation to undertake the work in the field of measurement errors is discussed. It will help the reader to get familiar with the thesis topic and its relevance to Particle Image Velocimetry (PIV).

1.1 Introduction to Fluid Mechanics

Fluid Mechanics is a discipline of applied mechanics which deals with the flow of fluid (*i.e.* liquid and gas). Fluid has the property to deform or flow continuously when subjected to the shearing forces. Under the influence of shear flow, fluid particle moves relative to one another which causes adjacent particles to have different velocities. To make the above explanation unambiguous, let us consider the flow over a flat plate as shown in Fig 1.1. When the fluid flows over the leading edge of the flat plate, a laminar boundary layer (*i.e.* steady flow and change in the velocity remains uniform Nancy Hall,NASA Official (2015)) starts to develop. After a certain distance depending on the physical and the flow conditions, small disorderly fluctuation begins to evolve in the fluid field. At a certain point downstream, the flow reaches a transition point, hereafter the flow begins to become turbulent and eventually the boundary layer becomes fully turbulent (*i.e.* unsteady flow and chaotic movement of the flow). The progression of the three regions can be parametrized in terms of the Reynolds number.

$$Re = \frac{\rho u L}{\mu} \tag{1.1}$$

where ρ is the fluid density, u is the velocity, L is the characteristic length and μ is the fluid dynamic viscosity.

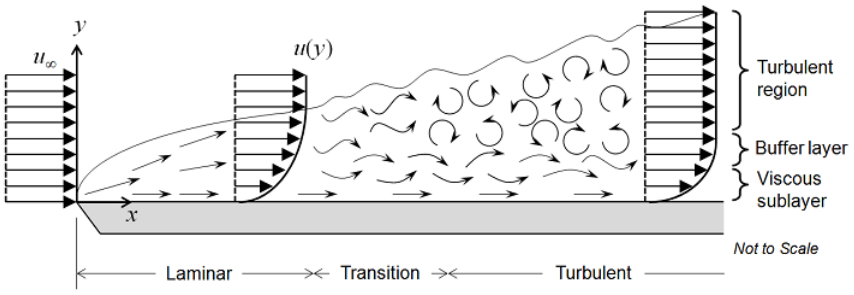

Figure 1.1: Evolution of boundary layer over a flat plate Walter Frei (2013)

Study of the fluid dynamics is often divided into three different areas: Experimental Fluid Dynamics (EFD), Theoretical/Analytical Fluid Mechanics and Computational Fluid Dynamics (CFD). EFD is based on the use of experimental methodologies, instruments and procedures for solving fluids engineering systems. Depending upon the size of the test section of the wind tunnel, full or scaled models can be tested. The models can be tested in various wind tunnels ranging from high/low-speed to supersonic/transonic wind tunnels to get the most realistic results using the knowledge of dimensional analysis. Theoretical Fluid Dynamics is based on the theory of mathematical physics problem formulation in term of control volume and differential equations. The major drawback of this method is that the exact solutions are only possible for problems with laminar flow having simple geometries and elementary initial & boundary conditions. CFD is the science of predicting fluid flow and related phenomena by means of mathematical modelling, numerical methods and software tools. In simple words, CFD helps an aerodynamicist in performing numerical experiment in a virtual wind tunnel by sitting behind a computer.

1.2 Comparison between CFD and EFD

Complex fluid dynamics problem (turbulent flow case) can be solved with either CFD or EFD. However, both the methods have their own merits and demerits.

EFD gives realistic results of the simulated scenario for complex test cases if scaling and dimensional analysis is done rightly. At the same time it is easier to qualitatively and quantitatively understand the flow behaviour around an object using the modern age flow visualisation techniques. The pitfall of EFD is that the experimental setup can be expensive and can take considerable amount of time in setting up the experiment. Also, if the setup needs to be tweaked in between the experiment or if the need arises to get a new apparatus for getting the desired result, it takes profuse amount of time. The experimental setup requires availability and synchronisation of a wide variety of measurement instruments such as pitot tube, temperature and atmospheric pressure sensor, etc.

CFD's colossal benefit lies under the fact that it does not requires any physical experimental setup. Thus, saving a lot of capital investment on the wind tunnel and various measuring instrument. CFD solvers can model most of the physical phenomenons. Also, tweaking the code is comparatively easier to gather data for different cases. However, the method is moderately difficult to understand as it involves advanced mathematics, physics and computer science skills. Simulations done in CFD is highly depended on the availability of the mathematical model. If a test case does not have a mathematical model then a CFD solver cannot be used on it. Most of the complex simulations such as Direct Numerical Simulation (DNS) and Large-Eddy Simulations (LES) cannot be run on a normal PC and requires powerful computers or super computers to do the computation efficiently. Moreover, solving equations on a computer introduces various numerical errors such as truncation error, round-off error, discretization error, etc which adds up and may causes serious error in the solution which does not predict the physical nature of the fluid anymore.

1.3 Significance of EFD

EFD has relatively longer history compared to CFD and therefore many researchers across the globe feels that EFD is more robust and reliable. Although there is a constant increase in the trend of using CFD by industries and the research institutes, still there are few flow cases in which CFD under performs compared to EFD such as predicting separated flow, flow behaviour in highly turbulent flows, etc. Thus, the wind tunnel testing is still the best way to obtain data in complex test cases. In order to validate the CFD solver it needs to be verified by comparing with the experimental results. Moreover, the accuracy of the CFD solution is confined by the goodness of initial condition and boundary conditions provided to the numerical model.

1.4 Brief history of Flow Visualisation

Flow visualization techniques are used to obtain diagnostic information about the fluid flow around a wind tunnel model. Since most fluids of interest (air for aerodynamics, water for hydrodynamics) are optically transparent, recognizing their motion requires the fluid to be tagged by particles which scatters light when illuminated. The widespread use of flow visualization techniques is owed to a number of benefits: it provides the description of the flow field without complicated data reduction and analysis, enables the validation of numerical methods, and it aids in the development and verification of new theories of the fluid flow.

To understand the fluid-structure interaction, the use of flow visualization goes back until the era of Leonardo Da Vinci in the 16th Century. His famous hand drawings were perhaps the world's first accounted documents to use this technique as scientific tool to study complex problem of turbulent flows. Next big step was taken by Ludwig Prandtl, who studied the suspension of mica particles around a 2D object like a cylinder and a prism on the surface of water. Although he was not able to gather any quantitative data but he succeeded to

change various experimental parameters (model & its scaling, incidence angle of the model, flow velocity, etc) using his designed water tunnel M. Raffel, C. E. Willert, S. T. Wereley, J. Kompenhans (2007). His contribution played a pivotal role in shaping the path for modern wind and water tunnels. Today, methods such as oil/smoke visualization, laser doppler velocimetry (LDV), hot wire anemometer (HWA), particle image velocimetry (PIV), shadowgraphy, schlieren method, infrared thermography (IR), etc offers a wide range of technique to address the flow problem in hand.

1.5 Fundamental of Particle Image Velocimetry (PIV)

Particle Image Velocimetry is an optical and quantitative method of flow visualization. The PIV technique measures the velocity of a fluid element indirectly by means of measurement of the displacement of tracer particles. Therefore, the flow must be seeded with tracer particle before the start of an experiment. For the photographic film or the video sensor to have two exposures having sufficient exposure of the scattered light, a high power light source for the illumination of the microscopic tracer particles is required which is illuminated twice. The development of PIV during the last two decades has been characterized by the replacement of analog recording and evaluation techniques by digital techniques.

For the readers who does not have any prior experience in PIV, a simple example would make the principle behind PIV logical. Consider a sunny day and sunlight coming through the window in a dark room. If you're sitting on the bed and you tap the mattress you will see dust particles because they are reflecting sunlight in all the directions. Similarly, PIV uses the same idea but in a more controlled environment. Room is replaced by the Wind tunnel test section, sunlight is replaced by laser sheet and dust particles are replaced by tracer particles which have the desired diameter to follow the flow as much as possible. Camera is used to take pictures of the area of interest. Fig. 1.2 shows the idea of principle behind PIV and the PIV experimental setup.

Figure 1.2: PIV experimental setup in wind tunnel test section explained

For evaluation of the acquired PIV raw images, they are divided into small areas (interrogation

windows). The displacement of the tracer particles in each interrogation window is determined by computational methods (generally by cross-correlation) using the first and second exposure of the camera. The advantage of PIV is its ability to spatially resolve all three component of the velocity vector instantaneously in a two- or three-dimensional plane. The main difference between PIV and other techniques of flow visualization is that PIV produces two-dimensional or even three-dimensional quantitative vector fields while most other techniques measure the velocity at a given point or provide solely qualitative information.

1.6 Peak Locking

As with any measurement, PIV cannot measure the velocity vector with infinite accuracy. Differences between the actual flow field and measured flow field will always be present due to the complexity of the technique. Broadly speaking, errors are introduced through sources such as wrong calibration, errors in experimental setup and measurement error in pixel displacement. Identifying the source of error in PIV images is a complicated task because it depends on various factors. One of the source of error in PIV data is peak locking which is a major source of concern for large scale and high-speed PIV application.

Peak locking is a form of bias error in PIV which causes biasing of the measured displacement towards integer values. This generally occurs when particle image diameter is smaller than the pixel size of the CCD or CMOS camera sensor array. If the particle image diameter is smaller than 1 pixel (1 pixel = chip size of a camera sensor array) it is not possible to determine the sub-pixel displacement as shown in Fig. 1.3(a). This happens because particle position along with the information of its light distribution is lost. However, when particle image diameter is greater (*e.g.* 3 pixels) then it can capture the sub-pixel displacement (see Fig. 1.3(b)). In the former case, due to its inability to measure sub-pixel displacement can lead to positional errors up to 0.5 pixels.

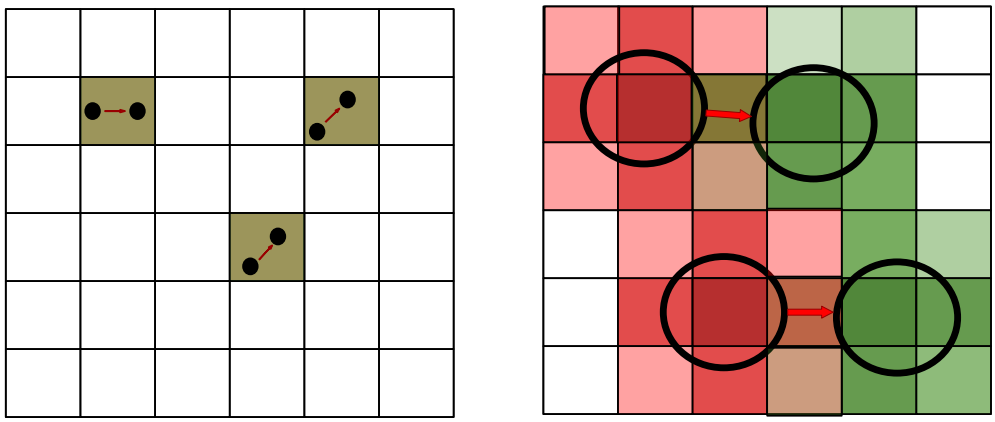

(a) under-resolved particle (b) well-resolved particle

Figure 1.3: Digital imaging of small particles over the camera chip

1.7 Motivation

The motivation to carry out the present work was to improve the accuracy of PIV measurement. The peak locking can be the dominant error source in PIV data. Since the information of the particle displacement is lost during the image acquisition, the error in the results for velocity, pressure, etc after PIV processing gets amplified. Fig. 1.4 shows the result of PIV velocity field for uniform flow (empty test section) where the wind tunnel velocity was 10 m/s. The measured velocity varies by 1% over the image which cannot be possible. This figure gives a clear account of the grim problem an experimentalist can run into when peak locking is present and can lead to wrong conclusions for the flow problem.

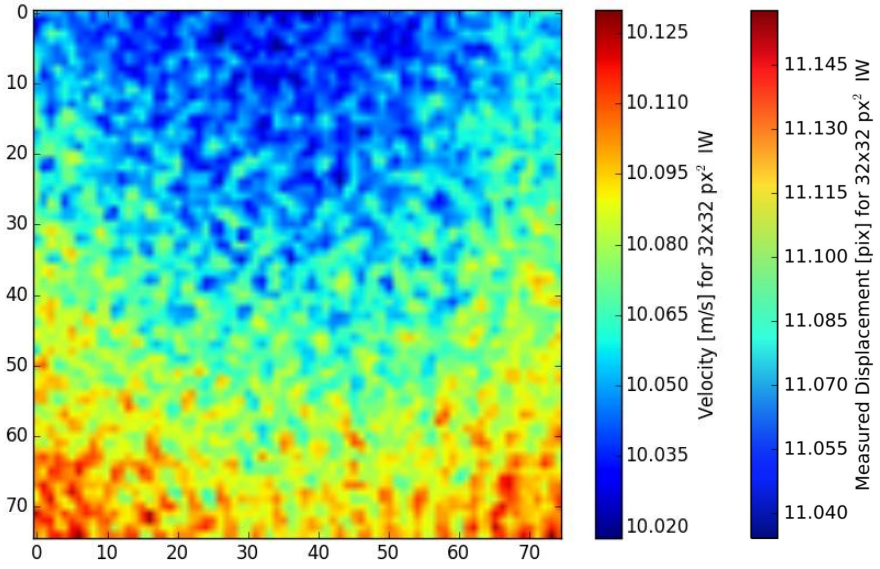

Figure 1.4: Effect of peak locking on PIV measurement of uniform flow

Peak locking as discussed above originates from the under sampling of the correlation peak due to digital imaging. As the magnitude of the peak locking error is dependent on the image particle size, it is often suggested to slightly defocus the image or to increase the lens aperture size. Still an experimentalist can have results influenced by peak locking when subjected to 3D flow such as turbulent flows. The effect of these optical parameters on the bias and random errors has never been studied in detail and only anecdotal evidence supports these solutions. Recently, D. Michaelis, Douglas R. Neal and B. Wieneke (2015) showed that peak locking can be reduced by using an optical diffuser while acquiring the PIV raw images. However, they did not do any wind tunnel testing to see the magnitude of decrement in the bias error. In the present work, their work would be carried forward by further testing diffusers and carrying out experiments to quantify the reduction in the bias error due to peak locking.

1.8 Objective

The main objective of this research is to reduce the bias errors due to peak-locking in PIV measurements. Sub-goals to achieve the main goal are as follows:

1. To study the Point Spread Function (PSF) of the diffuser to determine its performance for different parameters such as the relative aperture size, focal length, the number of diffusers used and the relative rotation between two diffusers.
2. To establish the effect of diffusers on measurement errors under different flow test cases.
3. To quantify the reduction in the bias error when diffusers are used.
4. Experimental assessment of effect of aperture size on the bias error and random error.

1.9 Contents

The present work has been divided into sub-parts in the form of chapters for better understanding of the topic. The thesis contains 7 chapters and they includes the following:

Chapter 2 includes the working principle, physical and technical background of PIV, description of the measurement errors and significant error sources followed by a review on the prior work done on reducing the systematic errors due to peak locking in PIV.

Chapter 3 describes the LaVision's diffuser and the working principle of diffusers in general.

Chapter 4 gives an account of the experimental assessment of point spread function width followed by transmittance study for no, one and two diffusers. Additionally, the synthetic image generator is also modified to include the effects of 0/1/2 diffusers in the PIV synthetic raw images.

Chapter 5 is composed of experimental determination of the bias error and the random error to see the effect of diffuser on peak locking for three different flow test case: uniform flow in empty test section, fully developed turbulent wake of a 2D cylinder, boundary layer of the test section floor.

Chapter 6 assesses results of the bias error and the random error for the different relative aperture sizes. This is done to shed more light on the best practice a PIV experimentalist can take to avoid errors in case of no diffusers.

Chapter 7 comprises of the major conclusion attained from the present work. Also, the future scope of the present work is discussed.

Chapter 2

Background

If I have seen further than others,
it is by standing upon the shoulders of giants

Isaac Newton
(1643-1727)

This chapter accounts the working principle and detailed physical and technical background of PIV. The propagation of measurement error as a function of dominant PIV error sources such as particle image diameter, image density, in-plane displacement and out-of-plane displacement is also reviewed. The chapter concludes with the discussion on previous work done in the field of reducing systematic error due to peak-locking in PIV.

2.1 Flow Seeding

Tracer particles are microscopic particles (having geometrical diameter in microns) employed which ideally follows the exact fluid flow around an object. However, the tracer particle are not able to follow the flow due to particle inertia, particle density, etc. For the tracer particles to faithfully follow the flow, particle response time should be smaller than the smallest time scale of the flow. The particle response time (τ_p) can be calculated using Eq. 2.1.

$$\tau_p = d_P^2 \frac{\rho_P}{18\mu} \tag{2.1}$$

where d_P is actual seeding particle diameter, ρ_P is the density of seeding particle and μ is the fluid dynamic viscosity. In turbulent flow, the fidelity of particle tracers to follow the fluid flow is given by Stokes number. Stokes number is defined as the ratio between the particle response time and the characteristic flow time. It is considered that if the Stokes number is less than 0.1, the PIV measurement yield an error of lower than 1%.

2.1.1 Scattering properties of tracer particles

Another important criteria for tracer particles is the intensity of scattered light when illuminated. The intensity of the scattered light from the particles should be high enough to capture the movement of particles by the imaging system. Fig. 2.1 shows that the ratio of forward to backward scattering increases rapidly. However, due to the limited optical access and the depth of field requirement, images are generally acquired from the sides where the scattered light intensity is least.

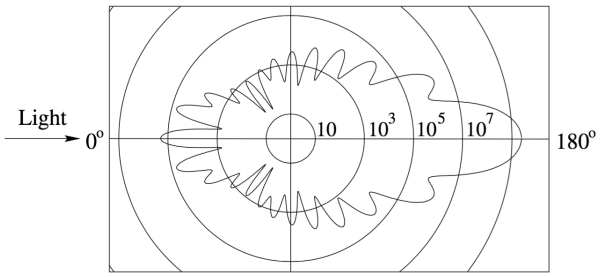

Figure 2.1: Light scattering by a 1μm oil particle in air M. Raffel, C. E. Willert, S. T. Wereley, J. Kompenhans (2007)

2.2 Illumination

From decades of PIV experience, illumination by the laser has been emerged to be the satisfactory choice of light source. This is because lasers can easily be shaped into a thin light sheet. PIV lasers are generally designed as double oscillator system which enables the user to regulate the separation time between the two laser pulses.

2.2.1 Lasers

Two of the most universally used lasers for PIV are discussed in this subsection.

Nd:YAG lasers are widely used for low frequency acquisition (λ = 532nm). They are generally driven in repetition mode because beam quality significantly decreases in case of single pulse. The thermal lensing problem due to thermal effects in laser crystals causes the degradation in the beam quality for single pulse Amir A. Jalali, J. Rybarsyk, and E. Rogers (2013). Nd:YAG lasers have repetition rate of 10 Hz of the two pulses. The pulse energy for each of two pulses is between 3 and 15 mJ.

Nd:YLF lasers or Neodym-YLF lasers used for high frequency acquisition (λ = 526nm) are gaining popularity because of an increasing number of applications in high speed PIV

techniques. Compared to Nd:YAG, the Nd:YLF have weaker thermal distortions which allows the later to have a better beam quality R. Paschotta (2008b) with repetition rates ranging from single pulse to 10 KHz. The maximum pulse energy for each of two pulses is 320 mJ.

2.2.2 Light Sheet formation

A combination of spherical and cylindrical lenses is used to transform the circular cross section of the laser beam into a thin light sheet. Laser sheet may damage the optics if the laser beam is focused before the desired field of view. Hence, care should be taken to have the minimum laser sheet thickness (laser sheet waist) beyond the measurement region.

2.3 Imaging

This section gives an account of the diffraction limited imaging which is due to the optical instrumentation. Various important parameters for the PIV recording are calculated using formulas discussed hereafter.

2.3.1 Image Recording

A crucial element in the PIV setup is the imaging system which captures the tracer particles convecting with the flow. Thus, making it an important aspect of the experimental test setup. The magnification factor is expressed as the ratio between the image size and the object size as shown in Eq. 2.2

$$M = \frac{\text{Pixel size} \times \text{Number of pixels in the sensor}}{\text{Field of View}} \tag{2.2}$$

where, pixel size and number of pixels in the sensor depends on the camera used. Field of view of the camera is decided by the user. The magnification factor can also be written as:

$$M = \frac{z_0}{Z_0} \tag{2.3}$$

where z_0 is the distance between the image plane and the objective lens and Z_0 is the distance between the objective lens and the object plane, as illustrated in Fig. 2.2.

Because the lens thickness of the objective lens is very small compared to the focal length, the thin lens assumption can be used M. Raffel, C. E. Willert, S. T. Wereley, J. Kompenhans (2007). The focal length (f) and the distances z_0 and Z_0 are related by Eq. 2.4.

$$\frac{1}{f} = \frac{1}{z_0} + \frac{1}{Z_0} \tag{2.4}$$

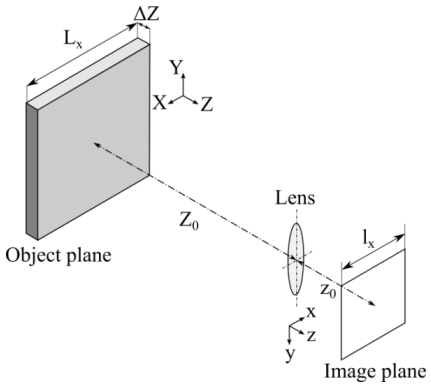

Figure 2.2: Geometric image formation A. Sciacchitano (2014).

To determine the desired focal distance (f), Eq. 2.3 is substituted into Eq. 2.4. The equation can be written as:

$$f = \frac{MZ_0}{1+M} \tag{2.5}$$

According to the geometric optics described above, the particles in the image should ideally have a diameter of

$$d_{\text{geo}} = Md_p \tag{2.6}$$

where d_P is the actual particle diameter. However, for small object geometrical optics does not appear as a point but as a broadened pattern due to the diffraction limit. The pattern can be approximated by the mathematical Airy function. Therefore, considering the diffraction effect, the imaged particle diameter d_{diff} can be obtained from the first zero of the Airy function M. Raffel, C. E. Willert, S. T. Wereley, J. Kompenhans (2007),

$$d_{\text{diff}} = 2.44 f_{\#}(1+M)\lambda \tag{2.7}$$

where $f_{\#}$ is the aperture size/f-number/f-stop which is the ratio between focal length and aperture diameter Joseph W. Goodman (1996). The particle image diameter d_τ appears enlarged in the DPIV images mainly due to four effects Christian J. Kahler , S. Scharnowski, C. Cierpka (2012):

1. diffraction at the limited aperture of the objective lens
2. defocusing
3. lens aberrations
4. discretization and quantization of the continuous image signal into a discrete signal with pixel size S

The resulting particle image diameter d_τ can be approximated MG Olsen, RJ Adrian (2000) by using Eq. 2.8

$$d_\tau = \sqrt{(Md_p)^2 + (2.44 \cdot f_{\#}(1+M)\lambda)^2 + \left(\frac{M \cdot z \cdot D_a}{Z_0 + z}\right)^2} \tag{2.8}$$

where M is the magnification factor, d_p is the particle diameter, λ is the wavelength of the light, z is the object distance from the focal plane, D_a is the lens aperture diameter, and Z_0 is the object distance.

The three terms in the Eq. 2.8 correspond to the geometric, diffraction, and defocusing components. For typical optical PIV parameters, $Md_p \ll d_{\text{diff}}$. Hence, $d_\tau \approx d_{\text{diff}}$ and the diffraction limit therefore dominates the imaged particle size.

The depth of field, δ_z, which is defined as the thickness of the region containing in-focus particles is affected by the *f-stop* and is given as:

$$\delta_z = 4.88 \left(\frac{1+M}{M} \right)^2 f_\#^2 \lambda \tag{2.9}$$

The depth of field should be within the range of the expected laser sheet thickness so that very few particles are out-of-focus.

2.4 Evaluation of particle motion

A computational evaluation is done to extract the displacement of the particle pattern between the two exposures of the PIV images. The cross-correlation can be employed for the evaluation. However, in the flow cases with significant velocity gradients, Richard D. Keane and Ronald J. Adrian (1992) showed that the cross-correlation method improves the dynamic range and removes the gradient bias in the measurements which is present in auto-correlation methods. The basic steps taken for PIV analysis is schematically shown in Fig. 2.3 and briefly discussed henceforth.

1. The PIV raw images are discretized into areas known as the interrogation windows. It is assumed that particles move homogeneously between the two illuminations. The velocity vector is calculated from the pixel displacement by using the time difference between the two illuminations. The size of the interrogation windows must be small enough to resolve reasonably small structures in the flow. A pitfall of using too small window size is the decrease of robustness of the results. If windows are small, less particles will be present in each interrogation window which results in faulty cross-correlation peaks. When the interrogation windows are large, the robustness of the result will be good, but small structures in the flow cannot be resolved.

2. Iterate the interrogation windows and calculate the cross-correlation function for each pair of interrogation windows using the interrogation window at $t = t_0$, denoted as W_1, and the interrogation window at $t = t_0 + \Delta t$, denoted as W_2. The discrete form of cross

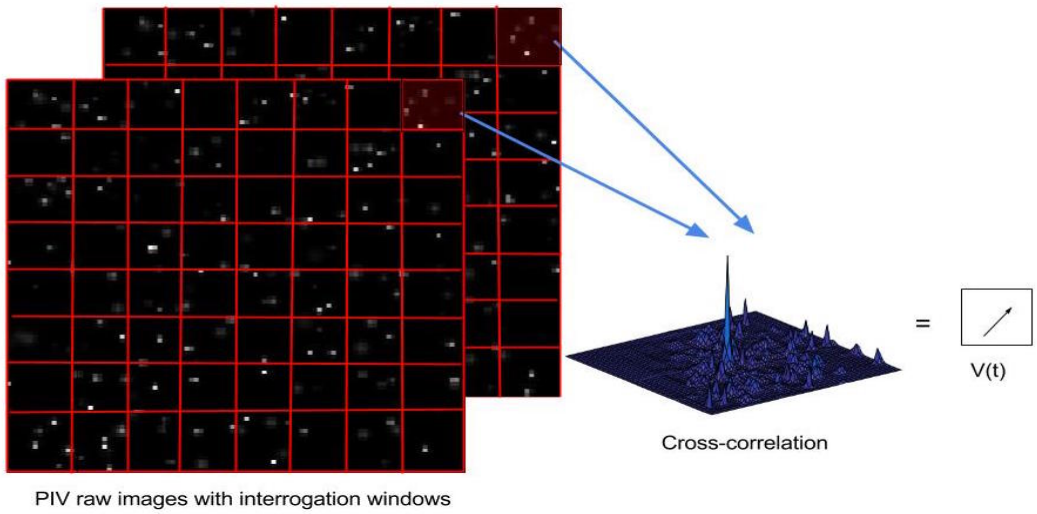

Figure 2.3: Steps for PIV statistical evaluation by cross-correlation

correlation is given as:

$$\phi(m,n) = \frac{\sum_{i=1}^{I}\sum_{j=1}^{J} W_1(i,j) \cdot W_2(i+m, j+n)}{\sqrt{\sum_{i=1}^{I}\sum_{j=1}^{J} W_1^2(i,j) \cdot \sum_{i=1}^{I}\sum_{j=1}^{J} W_2^2(i,j)}} \tag{2.10}$$

where ϕ is a matrix twice the size of I.

3. The locations of the peak of ϕ is established by searching for the maximum intensity peak in each cross-correlation function. The offset of the peak of ϕ from the center of the matrix denotes the displacement in pixel unit. An example of such peaks can be seen in Fig. 2.3.

4. The velocity vector is computed by using the camera pixel pitch, the magnification factor and time separation (Δ t).

2.5 Synthetic Image Generator

A synthetic image generator gives full control in hands of the user to change the image characteristics for parameters such as image dimension, particle image peak intensity, mean particle diameter, image density, laser sheet thickness, out-of-plane displacement, in-plane displacement, displacement gradient, background noise, etc. The synthetic image used here is based on the algorithm discussed by M. Raffel, C. E. Willert, S. T. Wereley, J. Kompenhans (2007). On the pixel array particle are randomly distributed. An individual particle in

synthetic images are described by a Gaussian intensity profile as shown in Eq. 2.11.

$$I(x,y) = I_o exp\left(\frac{-(x-x_o)^2-(y-y_o)^2}{(1/8)d_\tau^2}\right) \tag{2.11}$$

where (x_o, y_o) is the center of particle image and randomly distributed throughout the image. In the above equation, particle image diameter (d_τ) is defined as the e^{-2} intensity value of the Gaussian bell shape which contains 95% of the scattered light. For a light sheet centered at Z = 0 with Gaussian intensity profile for I_o is given as,

$$I_o(Z) = q \cdot exp\left(-\frac{Z^2}{(1/8)\Delta Z_0^2}\right) \tag{2.12}$$

where ΔZ_0 is the laser sheet thickness also measured at e^{-2} intensity waist point of its Gaussian profile.

Hence, for generating the particle image, particle position (X_1, Y_1, Z_1) are randomly generated within the specified laser sheet intensity profile. The peak intensity ($I_o(Z_1)$) is calculated using Eq. 2.12 for Gaussian intensity profile. When all these inputs are fed to Eq. 2.11, it gives the intensity captured by each pixel. To simulate displacement, another image is generated with same process as discussed above but with an offset of the previous image particle location depending on the x, y and z displacement specified by the user.

Background noise in the synthetic image is added as a product of the uniform distribution of random numbers and by the user defined noise intensity. The (white) noise added in an image pixel is uncorrelated with its neighbours and with its counterpart exposure. All the synthetic images created in the present work have image dimension of 500 × 500 px^2.

2.6 Measurement Errors

The measurement error is a combination of outliers, random errors and bias errors H. Huang, D. Dabiri and M. Gharib (1997). These errors and their sources are discussed in details in this section.

2.6.1 Outliers

Outliers are the incorrect data point which are much greater than the other observed data points. The spurious vectors in the data can be present due to inhomogeneous seeding, turbulence, varying intensity of light sheet, etc. The amplitude of this error is generally larger than the other points in the data set as shown in Fig 2.4(a) and are easy to detect. Various literature have been published on the methods to reduce or remove the outliers from the vector field (*See* R. D. Keane and R. J. Adrian (1990), C. E. Willert (1992), H. T. Huang, H. E. Fiedler, J. J. Wang (1993a,b), J. Westerweel (1993b)). Hence, it will not be discussed further and is beyond the scope of the present work.

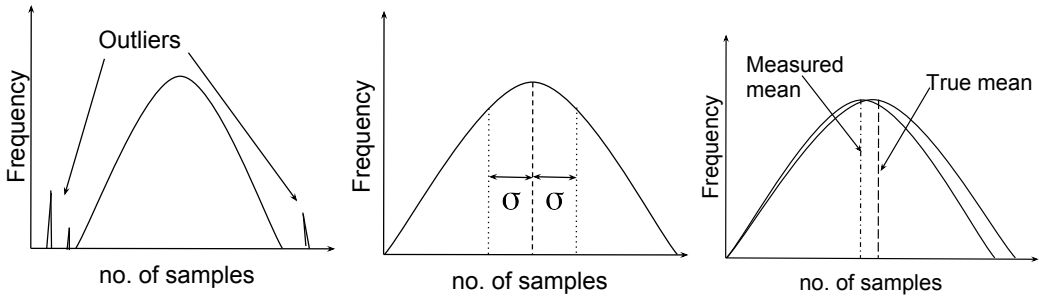

(a) Outliers (b) Random error (c) Bias error

Figure 2.4: Types of Errors

2.6.2 Random Error

The random error or statistical errors are statistical fluctuations in the experimental data. These changes may occur in the measuring instruments or in the experimental test conditions. Generally random errors have a Gaussian data distribution. In such cases the mean of the number of measurements of the same quantity is the best estimate of that quantity, and the standard deviation of the measurements shows the accuracy of the estimate. Fig 2.4(b) shows the Gaussian profile of the data. The dashed-line and dotted-lines shows the mean and the standard deviation (σ) of the data set respectively. The random error is the error in estimating the peak location of the measured particle displacements. It is defined as shown in Eq. 2.13

$$\epsilon_{\text{rand}} = \sqrt{\frac{1}{N} \cdot \sum_{i=1}^{N} \left(d_i - \bar{d}_{\text{meas}}\right)^2} \tag{2.13}$$

where d_i is the result of the i^{th} measurement, $\bar{d}_{\text{meas}}$ is the mean measured value and N is the number of measurements. In present work, the RMS error is also defined by Eq. 2.13.

The random error are different for each measurement and are associated with factors related to image characteristics. They are majorly associated with particle image diameter, inhomogeneous seeding density, displacement gradient and out-of-plane particle motion A. Sciacchitano, Douglas R. Neal, Barton L. Smith, Scott O. Warner, Pavlos P. Vlachos, B. Wieneke and F. Scarano (2015) B. H. Timmins, Brandon W. Wilson, Barton L. Smith and Pavlos P. Valchos (2012). Monte Carlo simulation was done for a-priori error estimation of PIV data. The effect of four major error sources typically in PIV measurement was analysed via synthetic image generation at different conditions. The aim of this simulation was to see the trend of the major error sources.

Particle image diameter: In the current simulation, images were generated with the particle image density of 0.1 ppp with no out-of-plane displacement. The in-plane displacement was constant at 7.5 pixels for all the images. The particle image diameter was varied between

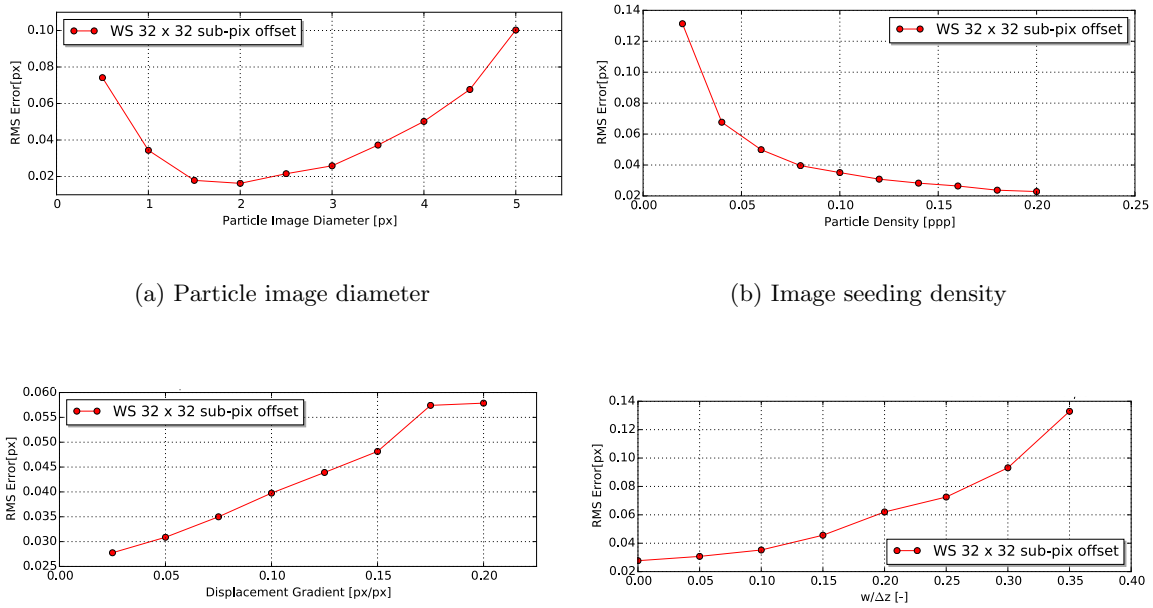

(a) Particle image diameter

(b) Image seeding density

(c) Displacement gradient

(d) out-of-plane

Figure 2.5: RMS error prediction via Monte Carlo simulation

0.5 - 5 pixels. Fig. 2.5(a) shows that the RMS error decreases as the particle image diameter increases till 2 pixels and after this point error starts to increase again. This trend was expected because peak-locking dominates the measurement error for $d_\tau \leq 1$ pixel. And for $d_\tau > 1$ random error starts to dominate which was investigated by J. Westerweel (1997).

Seeding density: The simulated images were generated with the particle image diameter of 3 pixels with no out-of-plane displacement. The in-plane displacement was kept at 7.5 pixels. The image density was varied between 0.02 ppp to 0.2 ppp. Fig. 2.5(b) shows that the RMS error decreases for increasing seeding density. At low seeding density there are less particle pairs in each interrogation window which makes it difficult to determine the true displacement peak. With increase in the seeding density, the number of particle pair increases and the true displacement peak is determined with a higher precision. It can also be seen that after 0.15 ppp adding more seeding leads to a minimal decrease in the magnitude of error.

Displacement gradient: A displacement gradient ranging from 0.02 to 0.2 pixels per pixel is considered in this case. In case of large displacement gradient, the quality of the matching of paired particle images decreases between the interrogation window of the two images, yielding a cross-correlation peak that broadens in the shear direction. The WIDIM algorithm F. Scarano, M. L. Riethmuller (1999) applied in-plane deformation and compensates the gradient effect. As a result, the RMS error is reduced by one order of magnitude F. Scarano, M. L. Riethmuller (2000).

Out-of-plane motion: The measurement error due to out-of-plane motion can be one of the

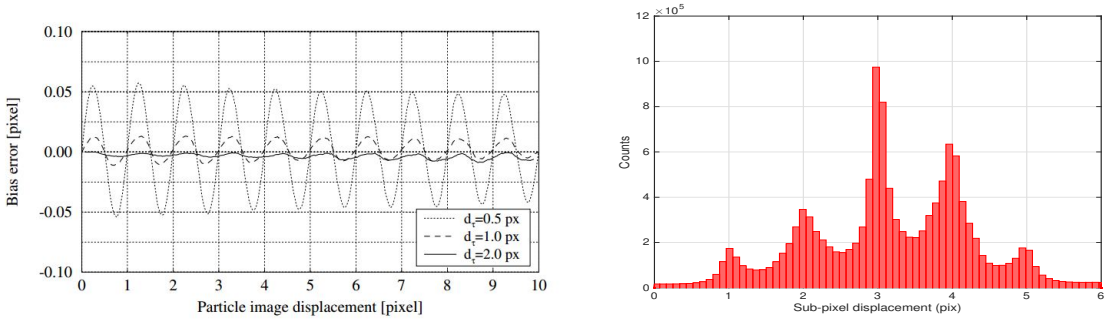

(a) Bias Error M. Raffel, C. E. Willert, S. T. Wereley, J. Kompenhans (2007)

(b) Histogram of PIV data

Figure 2.6: Bias error as a function of displacement associated with insufficient particle size

main source of errors H. Nobach, E. Bodenschatz (2009). The current simulation considers an uniform in-plane displacement of 7.5 pixels and out-of-plane displacement ranging from 0 to 0.35 ΔZ. Fig. 2.5(d) shows an exponential increase in the RMS error with respect to the out-of-plane motion. This happens because of loss of particle pairs in the interrogation area of the two exposures.

2.6.3 Bias Error

The bias error or systematical errors are inaccuracies in the data that are consistently there even though a large sample is averaged for statistical convergence. They are often due to a problem which persists throughout the entire experiment such as erroneous calibration by the experimentalist. Fig 2.4(c) shows the mean of the large number of measured data samples which is not same as the true mean because of systematic errors persistent in the data. The bias error (ϵ_{bias}) is the difference between the mean of the measured displacement ($\bar{d}_{\text{meas}}$) and the true displacement (d_{true}) if the mean is fully converged as shown in Eq. 2.14:

$$\epsilon_{\text{bias}} = \bar{d}_{\text{meas}} - d_{\text{true}} \tag{2.14}$$

The bias errors can be caused by errors during the calibration, low fill ratio, etc. Systematic errors can also occur in the form of peak-locking when the particle image diameter is of the order of one pixel or less J. Westerweel (1997). In this case the particles tends to be biased towards an integer value. The significant effect of bias error due to peak-locking can be clearly seen in the case of sub-pixel displacement as shown in the Fig. 2.6(a). Also, a distorted histogram as shown in Fig. 2.6(b) aids to understand whether the data is biased towards integer values or not.

2.7 Background on peak-locking

The peak-locking error has been a subject of study for almost two decades now. In conventional PIV experiments, the minimum resolvable particle image displacement is typically about 0.1 pixel in magnitude J. Westerweel (1997). K. T. Christensen (2004) showed that the peak-locking error has a significant effect on the calculation of vector field in turbulent flows. Parameters which influence peak-locking are: type of window deformation (window offset or window deformation), iteration type (single-pass, multi-pass or multigrid), correlation technique (standard cross-correlation or phase correlation), sub-pixel interpolation applied (Gaussian, Sinc, etc), pixel interpolation for window deformation (B-Spline, bi-linear, etc) and the characteristic of an image (particle size, magnification, focusing and aperture) D. Michaelis, Douglas R. Neal and B. Wieneke (2015). Various ideas and methodologies have been tried which have led to some major breakthroughs along the way but none of the methods removes peak-locking completely from the PIV measurements. In this section, various methods will be discussed which have been categorized on the basis of methodologies used.

2.7.1 Type of window deformation

J. Westerweel, D. Dabiri, M. Gharib (1997) showed that the interrogation window offset by the integer part of the in-plane displacement is relatively easy and reduces the noise level of the measurement. The evaluation of displacement is done in consecutive stages, the updated shift value is given to the second interrogation window during the cross-correlation until the displacement of less than a pixel is achieved. Numerical and experimental test done using window offset method by them in a flow with low and high turbulence intensity showed that the magnitude of noise is directly proportional to the square of fluctuation in the displacement for low turbulence intensity and have an average value of approximately three (independent from fluctuation in displacement) for high turbulence intensity. F. Scarano, M. L. Riethmuller (2000) demonstrated an effective way to reduce the loss of particles during in-plane motion. A rigid translation of interrogation window by sub-pixel offset, which is equal to the sub-pixel estimate of displacement in the previous iteration. It is well established that iterative window deformation is superior compared to window offset method in reducing measurement error. However, a residual effect from interpolation is still present that leads to peak-locking. Murali R. Cholemari (2007) displayed that the peak-locking is maximum when particle image diameter is 1.2 pixels in 1D optical flow case. Additionally the error increases with a decrease in fill factor and inverse peak-locking can be seen when image saturation is high. His approach is based on the window offset method J. Westerweel, D. Dabiri, M. Gharib (1997) and the fact that the bias errors are always sinusoidal in nature. He used a *stretched* sin function to reduce the bias error by a factor of more than 6.

$$\text{stretched sin function} = \begin{cases} a\sin\left(2\pi\frac{p}{0.25}x\right), & \text{if } |x| < p \\ a\sin\left(2\pi\frac{0.25}{p}\frac{0.5-|x|}{0.5-p}\right)x, & |x| \geq p \end{cases} \tag{2.15}$$

where a is amplitude of sinusoidal function of the bias error, x is the sub-pixel displacement and p is the displacement at peak error which can be determined after executing the window

offset method. This method can further reduce the bias error if the displacement at peak error is determined from iterative window deformation method.

2.7.2 Correlation techniques

J. Chen, J. Katz (2005) introduced a correlation mapping method in which a virtual correlation between the virtual second image and the first image is matched with the actual cross-correlation. Hence, it gives the sub-pixel part of the displacement. The B-spline interpolation is used to create the virtual image because it has lower interpolation errors when sub-pixel displacement is in the vicinity of 0.5 pixels. For comparison, virtual and actual correlation needs to be normalized first. Despite significant reduction in peak-locking, the method is computationally expensive because a new virtual image is created after every iteration to determine the virtual correlation. A. Eckstein and Pavlos P Vlachos (2009) instigated signal-to-noise ratio (SNR) model for digital PIV images. They first considered phase transform (PHAT) filter which results in transformation of cross-correlation into phase correlation. Although the peak of phase correlation peak for PHAT filter is sensitive to noise, a study was done to reduce it. In PIV, Fourier transform of discrete finite signal strength is significant, signal's estimation can be improved by averaging the input signal. Thus, a smoothing filter to the cross-correlation was implemented in the robust phase correlation (RPC), given as:

$$W(k) = \frac{SNR(k)}{|C_{12}(k)|} = \frac{1}{|C_{12}(k)|} \cdot \frac{P_s(k)}{P_s(k)} \tag{2.16}$$

where $P_s(k)$ and $P_n(k)$ are the power spectra of particle image signal and the noise signal respectively. This filter is a product of PHAT filter and SNR. Although the method is computationally efficient because it is a Fourier based cross-correlation but it introduces Fourier-based errors such as it assumes input signals as periodic. The error in RPC due to Fourier transform can be reduced if the cross-correlation is also done in Fourier domain as shown by T. Roesgen (2003) in his investigation on interpolation method. To summarise, O. Pust (2000) showed that the generalized cross-correlation algorithm is computationally expensive but it gives satisfactory results compared to FFT based cross-correlation.

2.7.3 Sub-pixel Interpolation Methods

The discrete cross-correlation of the two exposures of PIV raw images only yields a rough estimate of the particle image displacement and have a resolution of 1 pixel. This was a major drawback of PIV in 1990s. J. Westerweel (1993a) did a mathematical comparative accuracy study of center of mass estimator and Gaussian-fit estimator to estimate fraction displacement from the cross-correlation of the PIV images. His finding suggested that the bias error decreased in the latter, but was not completely removed.

$$\text{Gaussian-fit estimator} = \frac{\ln R_{-1} - \ln R_{+1}}{2(\ln R_{-1} - 2\ln R_0 + \ln R_{+1})} \tag{2.17}$$

where R_0 is the location of the highest peak of the discrete cross-correlation of the two exposures and R_{-1} and R_{+1} is the peak location adjacent to left and right of the highest

peak respectively. The Gaussian filter makes use of the established knowledge that the Airy function of the diffraction-limited particle also have a Gaussian shape. T. Roesgen (2003) introduced *sinc* interpolation algorithm which was directly implemented in the Fourier space. In this method, the Gaussian pulse is interpolated to increase its resolution by a factor of five. The original data is zero-padded with four zeros sequentially following each sample. Nearest neighbor interpolation is executed with a top-hat kernel. This results in *sinc* interpolation in Fourier domain. However, applying *sinc* interpolation in discrete cross-correlation leads to interpolation error. This problem was avoided by doing Fourier transformation of the cross-correlation. Murali R. Cholemari (2007) concurs with Roesgen's claim that *sinc* interpolation is superior to the Gaussian interpolation because it is computationally more efficient and gives a better sub-pixel displacement estimation. However, H. Nobach, N. Damaschke, C. Tropea (2005) claims and showed that Gaussian Interpolation has less RMS error compared to *sinc* interpolation as a function of the particle image diameter. L. B. Fore (2010) developed a simpler yet effective method for reducing mean bias error. He demonstrated that subtraction of means of interrogation area (I_1, I_2) from the discrete cross-correlation function $R(x, y)$ produces cross-covariance function $C(x, y)$.

$$C(x, y) = R(x, y) - I_1 I_2 \tag{2.18}$$

A potential issue with the method is the possibility of negative values of C(x,y) which would lead to a breakdown of Gaussian-fit as the logarithm of negative is undefined. This was resolved by adjusting the peak and neighbouring points in the positive direction prior to the application of Gaussian sub-pixel interpolation. Use of covariance function before interpolation reduces the mean bias error and uniformly distributes the random error across the fractional displacement.

2.7.4 Histogram Equalization methods

G. I. Roth, J. Katz (2000) came up with the modified histogram equalization (MHE) method which maximizes the contrast of the image by mapping the intensity levels in the original image to a new image which has a uniform intensity level throughout the image via transfer function. In MHE algorithm, the user sets the image background percentage r'. Below r' the transfer function maps all the intensities as zero. Histogram equalization is then performed on the values higher than r' values.

$$s'(r) = \begin{cases} 0, & \text{if } r < r' \\ \frac{R}{1-x} \int_{r'}^{r} Pr^{\text{old}}(\omega) d\omega, & r \geq r' \end{cases} \tag{2.19}$$

where r is the intensity of the pixel in the original image, R is the maximum intensity profile, $Pr^{\text{old}}(\omega)$ is the height of the histogram at ω and s' is the MHE transfer function. This method is relatively simpler compared to the other discussed methods and gives a significant reduction in peak-locking. R.J. Hearst, B. Ganpathisubramani (2015) improved the above discussed method. They showed that if the histogram equalization is done for all the vector at once it leads to bias error of its own. They proposed a method to reduce peak-locking by applying histogram equalization on each vector of the image. Nonetheless, drawback of doing so is that this method becomes computationally expensive and cumbersome because

pixel-locking is embedded in all the images separately, and thus one needs to adjust for pixel locking in each image separately for statistical end result. The MHE for all the vectors at once is still better compared to histogram equalization on each vector because the former is computationally cheap and shows small difference in peak-locking reduction in contrast to the latter.

2.7.5 Image Acquisition methods

All the above method shows a reduction in peak locking but the bias error is still present in all the results. This is because peak locking error is an error which gets embedded in the image during the acquisition and once the information is lost none of the methods can bring back the information lost. Hence, the best way to reduce the peak-locking error is to avoid them in the first place *i.e.* during image acquisition.

Conventional wisdom in PIV has it that slightly blurring the image before image acquisition improves the precision of the estimated location. This is a common practice which is still followed to avoid peak-locking. J. Westerweel (2000) showed that the particle size increases with blur which also increases the random error and if proper care is not taken while defocusing it can lead to cancel out the favourable effect of blur. Recently, it was found that the effect of blur still holds to be effective alongside modern interpolation and window deformation algorithms E.F.J. Overmars, N.G.W. Warncke, C. Poelma and J. Westerweel (2010). D. Michaelis, Douglas R. Neal and B. Wieneke (2015) showed that the optical diffuser can be used to avoid peak-locking. They suggests to use an optical diffuser plates which spreads the light intensity equally on the Bayer pattern color sensors. Results from the synthetic image and precision turntable show promising result to avoid peak-locking. However, the performance of the optical diffuser at different focal length, aperture size, angle between two lenses still needs to be studied. Moreover, they did not do any wind tunnel testing to see the magnitude of decrement in the bias error.

In the present work, their work is carried forward by further testing the optical diffusers and carrying out experiments under different flow cases to quantify the reduction in the bias error due to peak-locking.

Chapter 3

Working principle of optical diffusers

Simplicity is the ultimate sophistication.

Leonardo da Vinci
(1452-1519)

This chapter presents the working principle of the diffuser and effects of using one and two diffusers for PIV imaging. The diffuser used in the present work is based on the principle of birefringence which will be discussed hereafter.

3.1 Fundamentals of birefringence

A light wave is an electromagnetic wave that travels alone (*i.e.* does not require any medium) unlike sound waves which requires a medium (air, water, etc) to travel. Basically light waves are produced by acceleration of an electric charge. The nature and properties of electromagnetic waves are beyond the scope of the present work. For our understanding, it is sufficient to acknowledge that an electromagnetic wave is a transverse wave (oscillation of electromagnetic field is perpendicular to the direction of wave propagation) and has an electric component and a magnetic component. A light wave coming from sun, candle or a lamp is unpolarized light because the waves are created by electric charges that oscillate in more than one plane.

Birefringence is defined as the double refraction of light by a material where the refractive index depends on the polarization direction of light. This means that we see two diffracted images at slightly different angle of the same object. Birefringence is a complicated phenomenon and in this section only a particular simple situation is considered to shed more light on its working principle. Let us consider a birefringent crystal with a thickness L as shown in Fig. 3.1. The crystal have a particular direction called the *optical axis* (OA) which

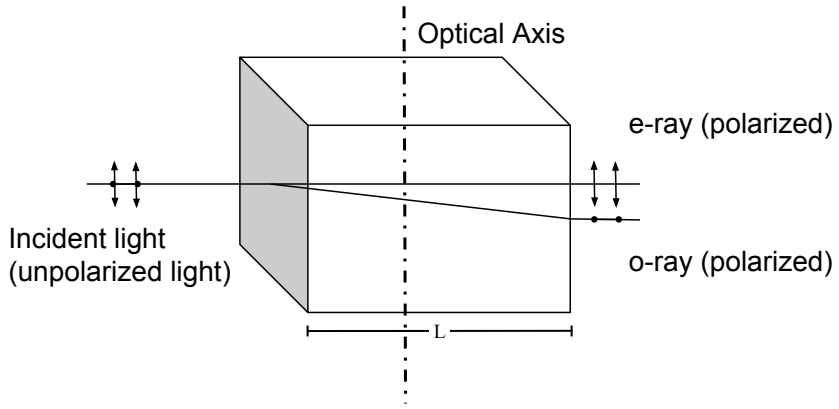

Figure 3.1: Ray diagram of an unpolarized light passing through a birefringent medium which takes one of two paths depending on the polarization of light

is not to be confused with a particular axis such as the principal axis of a lens. Consider the incident light having two polarized components, one which is parallel to the optical axis and one which is perpendicular to the optical axis. It is the property of the birefringent material that the refractive index depends on the direction of the electric-field. When the component of the electric field is aligned with the optical axis, that ray of light experiences extraordinary refractive index (η_e). When the electric field is perpendicular to the optical axis, the ray of light experiences ordinary refractive index (η_o). If the electric field is oblique to the optical axis then a component of the light ray experiences η_e and the other component experiences η_o. The difference between the optical path (Δl) of these two component is given as:

$$\Delta l = (\eta_e - \eta_o) \cdot L \tag{3.1}$$

where L is the thickness of the birefringence plate.

3.2 LaVision's diffuser

LaVision's diffusers consists of two diffusers attached to the M42 lens mount. The distance between the two diffuser is approximately 3mm. Each diffuser consists of two birefringence plates rotated to each other at 90 degrees with a glass plate between them. For an incoherent light ray, the output of a diffuser will give 4 spots of equal intensity. The combination of two diffusers shifts 25% of the light in all the directions when the two diffusers are kept at 45° relative to each other.

Fig. 3.2 shows a diffuser which consist of two birefringent plates. The optical axis of plate 1 is parallel to the surface of the page and the optical axis of plate 2 is perpendicular to the page as shown in the figure. Consider an unpolarized coherent light ray incident on the plate 1. As discussed in section 3.1, the unpolarized light can be broken down into two components:

- Component 1: component of incident light parallel to the optical axis of plate 1.

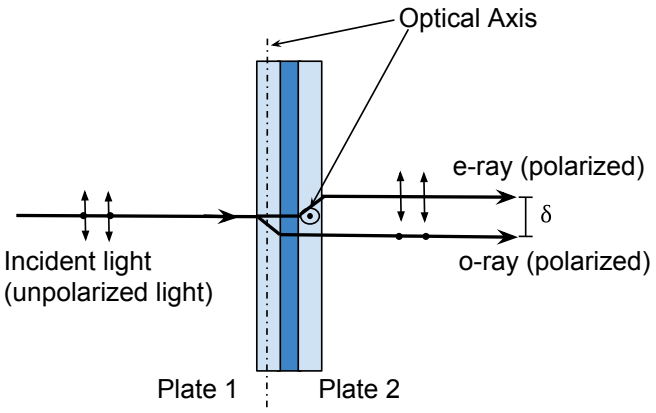

Figure 3.2: Ray diagram showing a coherent unpolarized source of light passing through a diffuser which consist of two birefringent material positioned at a relative angle of 90°

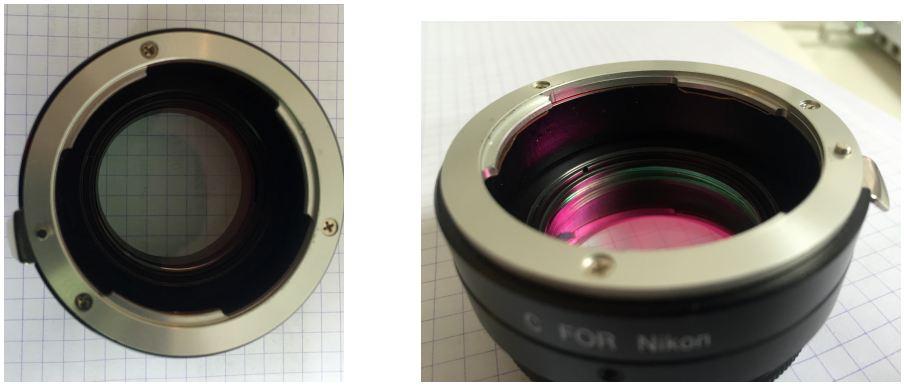

(a) Top View (b) Isometric View

Figure 3.3: LaVision's diffusers

- Component 2: component of incident light perpendicular to the optical axis of plate 1.

For the component 1, the electric field is parallel to the optical axis and will experience the extraordinary refractive index (η_e) of plate 1. As it moves to the plate 2, component 1 will experience the ordinary refractive index (η_o) of plate 2 because it is perpendicular to the optical axis. Thus, the component 1 will go straight from the plate 1 and bend in a particular direction in the plate 2 due to difference in the refractive index of the the glass plate and the plate 2. Similarly, for the component 2, it will see η_o in plate 1 and η_e in plate 2. The light ray of this component will first suffer a particular bend in its path in plate 1 and then come out straight from plate 2. The output rays of light have a lateral shift which is denoted by δ in the figure. For an incoherent source of light, each component will have two linearly polarised components resolved in the direction of component 1 and component 2. Thus, the output of such a source passing through the diffuser will give four rays of equal intensity,

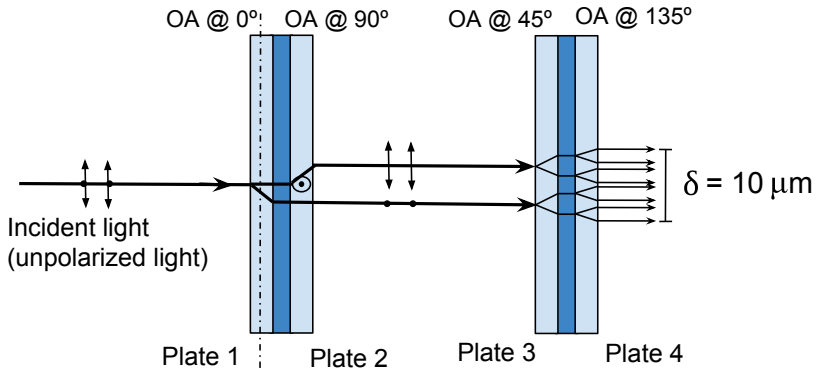

Figure 3.4: Schematic diagram showing the ray diagram for two diffusers kept at a relative angle of 45° for an unpolarized coherent light

Fig. 3.3(a) shows that the size of the pattern seen through the diffuser is same as the pattern size seen without the diffusers. Even by changing the height between the object and diffusers, there was no magnification effect in diffusers on visual inspection. Fig. 3.3(b) shows a purple glare over the lenses which is due to a high grade anti-reflective coating. An anti-reflective coating is applied on diffusers to remove reflections and improve the quality of diffusers.

3.2.1 Using two diffusers

When using two diffusers, the incident ray is refracted to multiple spots on the image sensor within a distance of $10\mu m$. Fig. 3.4 shows the ray diagram for a coherent unpolarized ray of light. The optical axis of plate 2, plate 3 and plate 4 is at an angle of 90°, 45° and 135° relative to plate 1 respectively. The incident rays diffracts into two rays as it comes out from plate 2 (discussed in section 3.2). When these two rays interact with the plate 3, the incident polarised light is at 45° to the optical axis. The incident light breaks down into two linear polarised components: a component parallel to the OA and another component perpendicular to the OA. Thus, the two incoming rays refracts into four rays as it comes out from plate 3 and similarly those rays gets refracted into eight rays when it comes out from the plate 4. Due to the property of the lattice structure, the refracted rays are within the distance of 10μm.

It is advisable to keep the diffuser at a relative angle of 45° with each other because when the incident ray is at an angle of 45° *w.r.t.* to the OA, the intensity of incident ray gets equally divided into two linearly polarised components having the same magnitude and oscillating at exactly the same phase as that of the incident ray Douglas B. Murphy, Kenneth R. Spring , Thomas J. Fellers and Michael W. Davidson (2016).

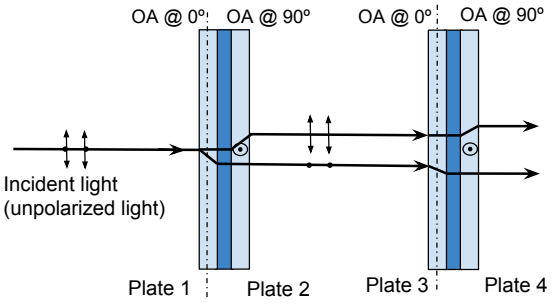

Figure 3.5: Ray diagram for two diffusers at a relative angle of 0°

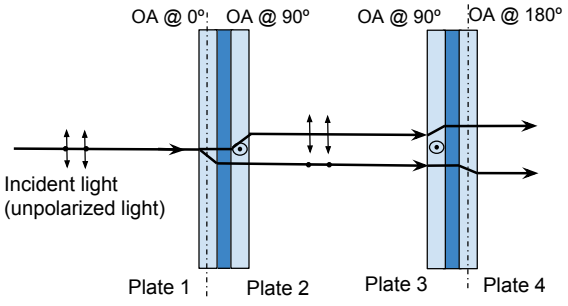

Figure 3.6: Ray diagram for two diffusers at a relative angle of 90°

3.3 Limitations

The system of two diffuser is least efficient when the relative angle between diffusers is 0°, 90°, 180° or 270°. For instance, when the relative angle between diffuser is 0°, the OA of plate 1 & plate 3 and plate 2 & plate 4 are in the same direction as shown in Fig 3.5. Hence, the incident ray follows the same path in plate 3 and 4 as it follows for plate 1 and 2 (discussed in section 3.2). Also, for relative angle of 90° between two diffusers, the OA of plate 1 & plate 4 and plate 2 & plate 3 are in the same direction. The ray diagram for coherent unpolarized light is shown in Fig 3.6. The e-component of light ray experience η_e in plate 1 & 4 and η_o in plate 2 & 4. Similarly, o-component experience η_o in plate 1 & 4 and η_e in plate 2 & 4. In both the cases discussed above, the number of light spots are significantly less compared to diffusers at 45° relative angle (Fig. 3.4).

In Chapter 4 and 5, this favourable effect of birefringence material is used to increase the effective particle image diameter and reduce the peak locking error in PIV measurements.

Chapter 4

Experimental determination of the point spread function & transmittance of diffusers

Nature always tend to act in the simplest way.

Daniel Bernoulli
(1700-1782)

The aim of the experiment in this chapter was to determine the point spread function (PSF) width of the imaging system containing no, one and two diffusers as a function of various relative aperture sizes. The test was carried out for 0/1/2 diffusers and by changing the relative angle of the diffuser for two different focal length lenses. Additionally, a synthetic image generator was used to create the synthetic images with particle image size corresponding to the experimentally determined particle image size of one and two diffusers to predict the particle image diameter for different input parameters when diffusers are used. Moreover, an experiment was conducted to study the transmittance of 0/1/2 diffusers. The setup of experiment, data reduction techniques, results and conclusion are discussed in this chapter hereafter.

4.1 Test Setup

The test setup for the PSF width and transmittance followed by data processing steps are discussed in this section.

4.1.1 Determination of the PSF width

The PSF width experiment was conducted at W-Tunnel of *Delft University of Technology*. An Arc based lamp light source (unpolarized light) was used to illuminate a white screen. The white screen was used to have a uniform distribution of the light intensity on a piece of cardboard with pinholes. To reduce the influence of image noise, more than 50 pinholes were made using a 0.4 mm diameter drill bit on the cardboard. An *ImagerIntense* Camera (CCD, 1376 $\times$ 1040 px^2, 12 bit, pixel pitch 6.45 μm) from LaVision was used to record images. Both the Nikon objective of 35 mm and 50 mm focal length (f) was used in the wind tunnel test. The magnification factor was kept at 0.014. The active sensor size was cropped to 63 $\times$ 127 px^2. In order to have the camera image plane perfectly parallel to the pinhole arrangement, the entire setup was mounted on a series of X-beams as shown in Fig. 4.2

The experiment was performed for no, one and two diffusers with 50 mm lens for all the $f_\#$ values between 2 and 22. In case of one diffuser, the diffuser was rotated from 0° to 180° in steps of 30° and images were recorded for all the $f_\#$. For two diffusers, one diffuser was kept at a constant position of 0° and the other diffuser was rotated from 0° to 180° in steps of 30°. For every relative diffuser angle, images were taken for all the $f_\#$ values. Similarly, the entire experiment was performed for another lens with the focal length of 35 mm. Essential parameters for the experiment are summarized in Table 4.1.

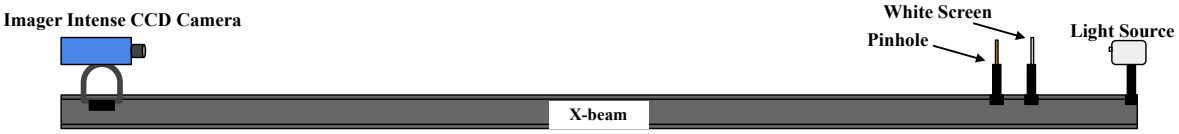

Figure 4.1: Schematic diagram for the PSF experiment

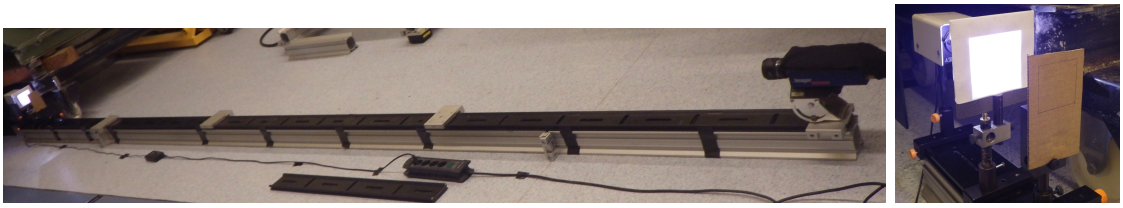

(a) (b)

Figure 4.2: Images from the actual test setup for the PSF experiment

Table 4.1: Essential parameters for determining the PSF width

Object	cardboard with more than 50 pinholes
	0.4 mm diameter
Illumination	Arc based lamp light source (White Light)
Recording device	LaVision's Imager Intense
	(CCD, 1376 × 1040 px^2, 6.45 μm pitch)
Imaging	*Nikon* objectives
	f = 50 mm and 35 mm lenses
Field of view	40 × 60 mm^2, 286 × 428 px^2
Acquisition frequency	25 Hz
Magnification factor	0.014
Number of images	20

4.1.2 Determination of transmittance

For the transmittance, images of the white screen were acquired for no, one and two diffusers. The experiment was conducted at W-Tunnel of *Delft University of Technology*. An Arc based lamp light source was kept at a distance to have a uniform distribution of the light intensity on the screen. An *Imperx Bobcat* Camera (CCD, 1628 × 1236 px^2, pixel size 4.4 μm) was used to record images. The camera was equipped with the Nikon objective of 200 mm focal length and the $f_{\#}$ was set at 8. The magnification factor was 0.48. The setup for this experiment is shown in Fig. 4.3. Essential parameters for the experiment are summarized in Table 4.2.

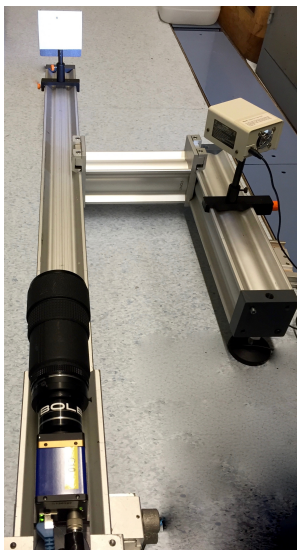

Figure 4.3: Setup of the experiment to determine the transmittance

Table 4.2: Essential parameters for determining transmittance

Object	White Screen
Illumination	Arc based lamp light source (White Light)
Recording device	Imperx Bobcat
	(CCD, 1628 × 1376 px^2, 4.4 μm pitch)
Imaging	*Nikon* objectives
	f = 200 mm lens
Aperture size	$f_\# = 8$
Field of view	18 × 9 mm^2, 178 × 77 px^2
Acquisition frequency	25 Hz
Magnification factor	0.48
Number of images	100

4.1.3 Data Acquisition

For the PSF width study: The PIV software Davis 8.2 was used for PIV processing. For reducing the background noise in the image, a time filter was used to subtract the minimum background intensity from all images. The average of 20 images were taken in the time domain to reduce the random error associated with it.

For the transmittance study: The *Imperx Bobcat* in-house software Bobcat GeV player was used to acquire images. No image pre-processing steps were applied. The mean of 100 images were taken to reduce the random error associated with the arc lamp which have a frequency of 50 Hz.

4.2 Methodology

The PSF is the convolution of a point source and the imaging optic instrument. It can be used to characterize the blurring in images from the optical devices. In present work, the autocorrelation function is used to determine the PSF width of a point source (pinhole). The PSF width and the correlation peak width are related by

$$d_D \cong \sqrt{2d_\tau^2 + \frac{4}{3}a^2} \tag{4.1}$$

where d_D is the width of the autocorrelation peak, a is the gradient parameter which is neglected when correlation width is obtained from autocorrelation Ronald J. Adrian, J. Westerweel (2010) and d_τ is the particle image diameter which is similar to the PSF width as they both represent the diffracted-diameter of a point source.

4.2.1 Autocorrelation

An autocorrelation is the cross-correlation of a signal with itself. In PIV, the height of the autocorrelation peak (R_h) is a function of particle image diameter (d_τ), image density (N_I), average peak intensity of particles (I_P) and interrogation window size (IA).

$$R_h = f(d_\tau, N_I, I_P, IA) \tag{4.2}$$

An autocorrelation map for an interrogation area can be determined using a frequency based correlation by applying the Wiener-Khinchin theorem M. Raffel, C. E. Willert, S. T. Wereley, J. Kompenhans (2007). The autocorrelation can be computed using Fourier transform, given as:

$$R = \mathrm{Re}[FFT^{-1}(FFT^*(IA)FFT(IA))] \tag{4.3}$$

where IA is the interrogation area, FFT is Fast Fourier Transform , FFT* is complex conjugate of FFT and Re is the real part of the complex number.

4.2.2 PSF width

The PSF width is directly proportional to the width of the autocorrelation peak (see Eq. 4.1). In order to find the standard deviation (σ) from the autocorrelation peak, 3 point Gaussian fit is applied to the autocorrelation plane M. Raffel, C. E. Willert, S. T. Wereley, J. Kompenhans (2007). The correlation peak's width is calculated from four times the standard deviation of the Gaussian intensity distribution. This insures that about 99% of the data values are within 4σ R. Paschotta (2008a). The PSF width is then given as:

$$d_\tau \approx 2\sqrt{2}\sigma \tag{4.4}$$

However, this method requires subtraction of the baseline background noise for accurate results. For Gaussian distribution, the 4σ method and $1/e^2$ method gives the same result.

4.2.3 Synthetic Image Generator for 1/2 diffusers

Synthetic image generator was used to numerically create images which have particle image diameter similar to the expected experimental values for one and two diffusers. The working principle for the synthetic image generator is discussed in section 2.5. The numerical particle image diameter was determined by using the brute-force approach. A correction factor of 1.7 was multiplied to the Eq. 2.7 which was decided on the basis of the obtained experimental results.

4.2.4 Transmittance

When the light impinges on a transparent material (optical device), it can be transmitted, absorbed, or reflected. Transmission of light is defined as the amount of light passing through

the medium without getting absorbed. In PIV, the scattered light from the tracer particles is transmitted through the lens to illuminate the camera image sensor. Thus, it is desired to have minimum loss of light through the lens to have a higher contrast of the tracer particles in raw images.

In present work, the transmittance was checked for one and two diffusers with respect to no diffuser to see whether the amount of light entering the image sensor gets affected. The images were acquired for the same FOV. The mean value of all the pixel intensity values were calculated for the three cases having the same region of interest (ROI).

4.3 Results

The analysis of the acquired data in the aforementioned experiments is discussed in this section hereafter.

4.3.1 Effect of diffusers

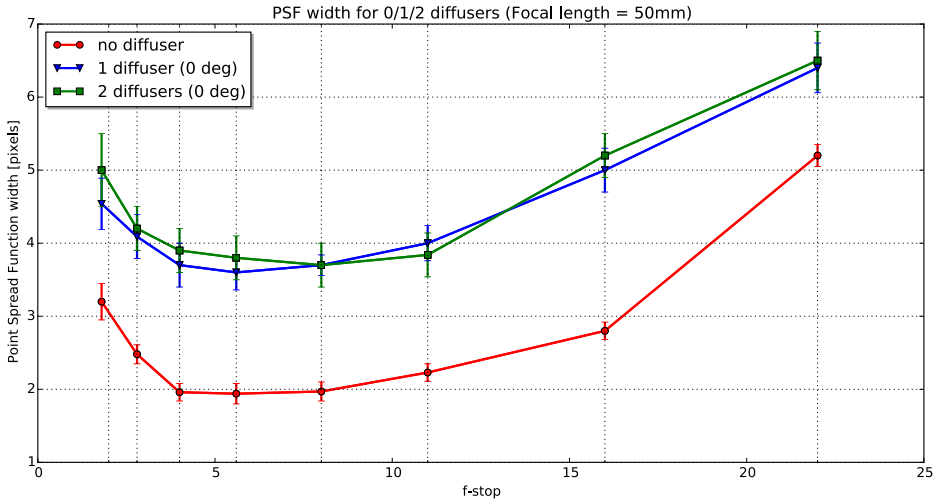

Figure 4.4: PSF width vs. $f_{\#}$ for 0/1/2 diffuser with standard uncertainty

The PSF width as a function of $f_{\#}$ for no, one and two diffusers with the 50 mm lens is shown in Fig. 4.4. For low $f_{\#}$ values, the PSF width is slightly larger possibly due to the lens aberration. For no diffusers, the PSF width decreases until $f_{\#} = 4$ as a result of reduced influence of the aberration. For $f_{\#} > 8$, PSF width starts increasing again as a consequence of the diffraction limit that occurs for small aperture size. In case of one diffuser there is a significant increase in the PSF width for the entire range of $f_{\#}$. For two diffuser with $0°$ relative angle between them, the change in PSF width compared to one diffuser is not marginal.

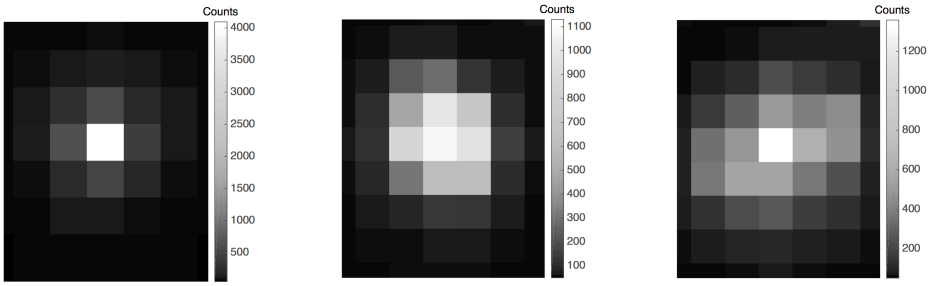

(a) No diffuser (b) One diffuser (c) Two diffuser

Figure 4.5: Image diameter of a pinhole for 0/1/2 diffuser at $f_{\#} = 4$

The image of one of the pinhole acquired during the experiment in case of no, one and two diffusers for $f_{\#} = 4$ is shown in Fig. 4.5. It can clearly be seen that due to favourable effect of diffusers, PSF width broadens for one and two diffusers. Also, the colorbars shows that the maximum peak intensity of the PSF decreases for one and two diffusers as expected.

4.3.2 Rotation of one diffuser

The PSF width as function of $f_{\#}$ for one diffuser at different angles is shown in Fig. 4.6. The diffuser was rotated at angles between 0° to 180° in steps of 30°. From the figure, it can be inferred that no significant increment in PSF width occurs for different angles of one diffuser. For all the angles the PSF width lies in the range of approximately ± 0.5 pixels.

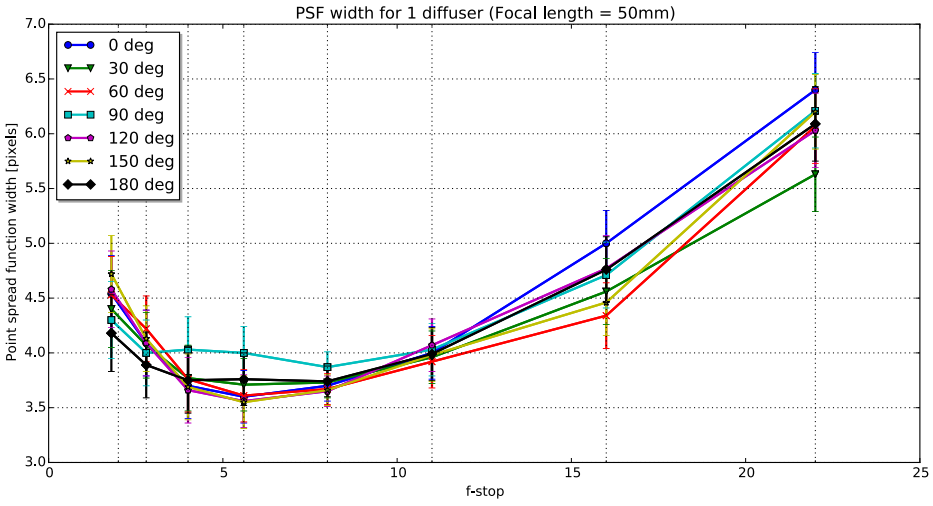

Figure 4.6: PSF width vs. $f_{\#}$ for one diffuser at different angles with standard uncertainty

The image diameter of the pinholes is shown in Fig. 4.7 for different diffuser angles at $f_{\#} = 4$.

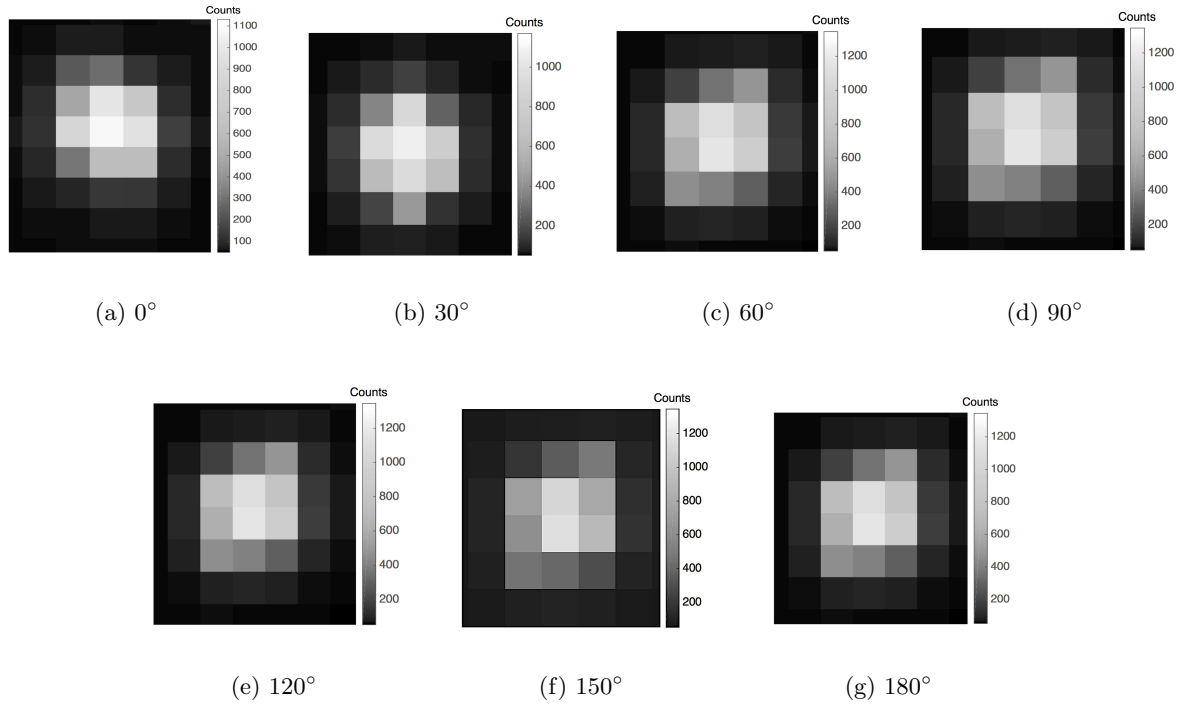

(a) 0° (b) 30° (c) 60° (d) 90°

(e) 120° (f) 150° (g) 180°

Figure 4.7: Image diameter of a pinhole for one diffuser for different angles at $f_{\#} = 4$

There is neither much change in the effective PSF width nor in the peak intensity values for different diffuser angles.

4.3.3 Relative rotation between two diffusers

The PSF width as a function of $f_{\#}$ for different relative angles (ϕ) of two diffusers is shown in Fig. 4.8. One of the diffuser was fixed and the angle of the second diffuser was varied from 0° to 180° in steps of 30°. The figure shows that change in relative angle of diffusers indeed have a significant effect on the PSF width. For the entire range of $f_{\#}$, the PSF width is least and maximum for relative angle of 90° and 150° respectively.

The image diameter of a pinhole for different relative angles of diffusers at $f_{\#} = 4$ is shown in Fig. 4.9. In few cases, there is a slight shift in the position of maximum intensity in the PSF. Also, there is a change in the shape of the PSF width. For instance, the PSF width at $\phi = 90°$ looks skewed in vertical direction.

Similar test was performed for 35 mm lens. The results were similar to the results shown in this section. For interested readers, results of the PSF width as a function of relative aperture for 35 mm lens is presented in Appendix A.

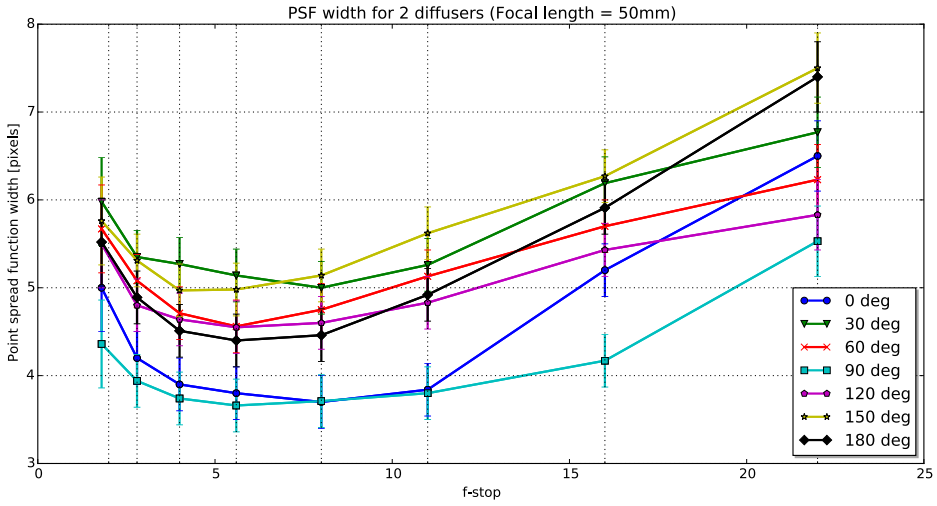

Figure 4.8: PSF width vs. $f_{\#}$ for two diffusers at different angles with standard uncertainty

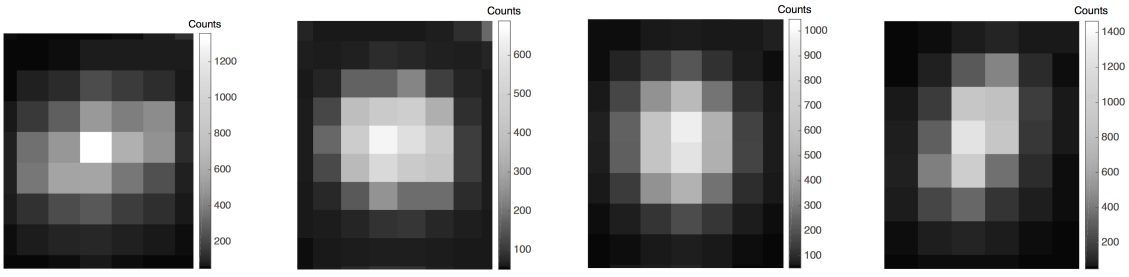

(a) 0° (b) 30° (c) 60° (d) 90°

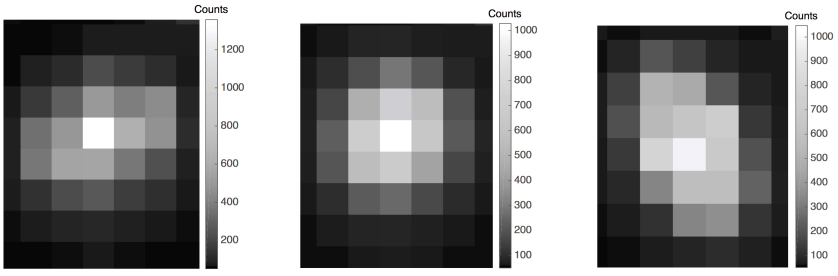

(e) 120° (f) 150° (g) 180°

Figure 4.9: Image diameter of a pinhole for two diffusers for different angles at $f_{\#} = 4$

4.3.4 Synthetic Image Generator for diffusers

The synthetic images were generated with similar property as discussed in Table 4.1. This was done to test if the synthetic image generator code can predict the particle image diameter

for no, one and two diffusers for various inputs.

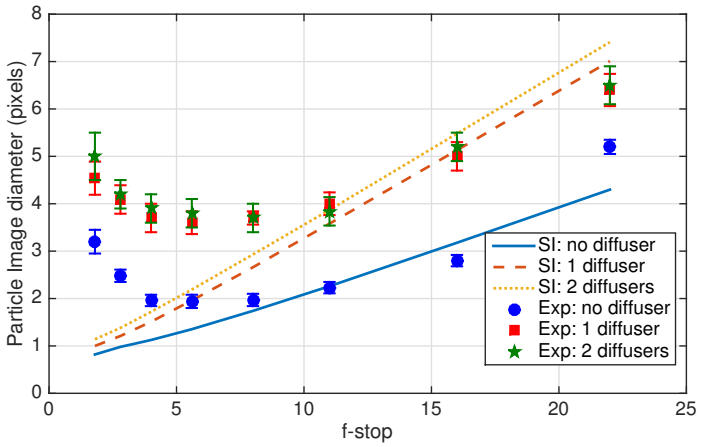

Figure 4.10: Numerical and experimental (with standard uncertainty) PSF width as a function of $f_\#$ for 0/1/2 diffusers

The PSF width as a function of $f_\#$ is shown in Fig. 4.10. The figure shows that the numerically assessed particle image diameter shows good agreement with its experimental counterpart for higher $f_\#$ values ($f_\# > 11$). The experimental PSF width is considered from the experimental test case where the lens with 50 mm focal length was used. The geometrical diameter of the pinhole was 0.4 mm. For larger aperture size ($f_\# < 5.6$), spherical aberration of the lens in experimental case leads to defocused and higher particle image diameter. This effect is not captured by the numerical method because it does not take into account the lens aberration. The image of the simulated particle in case of no, one and two diffusers for $f_\# = 16$ is shown in Fig 4.11.

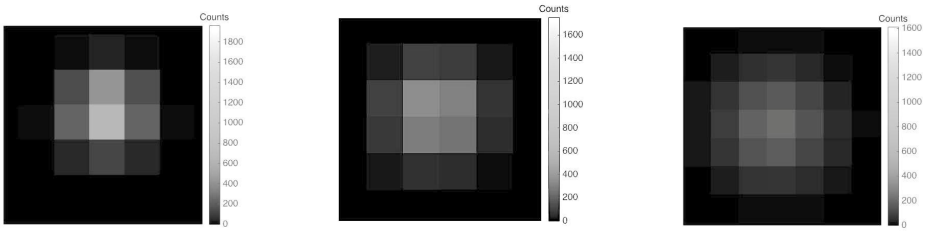

(a) No diffuser (b) One diffuser (c) Two diffuser

Figure 4.11: PSF width from synthetic image for 0/1/2 diffuser at $f_\# = 16$

4.3.5 Transmittance

The transmittance test was done to see the amount of light passing through the diffuser to the image sensor. If less light passes through the diffusers, the image quality gets affected and the random error would increase. With *daylight filter*, all the test cases have nearly same transmittance (*see* Fig. 4.12(a)). However, for no *daylight filter* as shown in Fig 4.12(b), the transmittance of no diffuser is slightly higher (by 10 counts) compared to one and two diffuser. Table 4.3 shows that the transmittance of one and two diffusers to be above 95% relative to no diffusers.

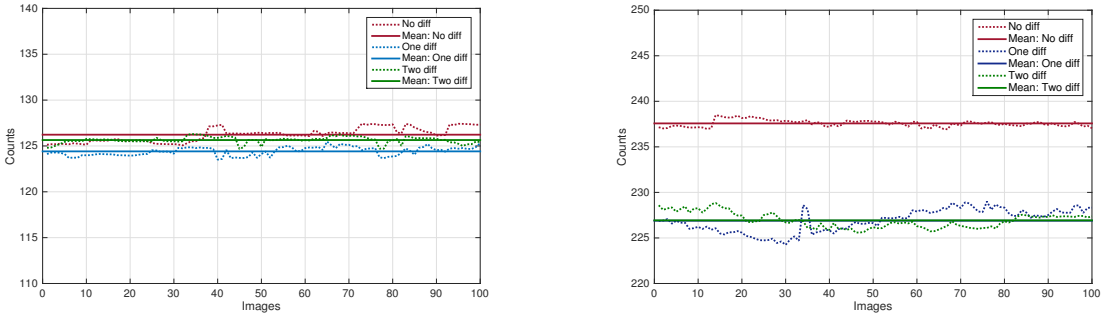

(a) With daylight filter

(b) Without daylight filter

Figure 4.12: Transmittance of 0/1/2 diffuser

Table 4.3: Change in image intensity for 0/1/2 diffusers

	With *daylight* filter	Without *daylight* filter
no diffuser	126.2 counts	237.2 counts
	(–)	(–)
1 diffuser	124.5 counts	226.9 counts
	(98.7%)	(96%)
2 diffuser	125.6 counts	226.9 counts
	(99.1%)	(96%)

4.4 Discussion

The PSF width as a function of relative aperture is shown in Fig. 4.4 where all the curve shows the same trend *w.r.t.* the change in relative aperture. The PSF width is higher for lower $f_{\#}$ because rays parallel to the principal axis at different distances from the principal axis fails to converge to a single point for large aperture diameter (also known as spherical aberration). As $f_{\#}$ increases (*i.e.* aperture diameter decreases) spherical aberration reduces.

For higher $f_{\#}$, light rays passing through a small aperture begins to diverge and interfere with one another, thus enlarging the PSF width. For one diffuser, the rays coming through the lens are diffracted which leads to an increase in the PSF width for all the apertures but has the same trend as discussed above. For two diffusers ($\phi = 0°$), change in the PSF width is not significant compared to one diffuser. However, for higher f/# (>16), the PSF width for two diffusers is similar compared to one diffuser because at small aperture the diffraction limit dominates the favourable effect of the two diffusers.

The rotation of one diffuser along optical axis showed that the effective PSF width remains almost same ($\pm$ 0.5 pixels) which is shown in Fig. 4.6. By changing the angle, the position of the diffracted rays also gets changed which can be seen in the PSF width of a point source as presented in Fig. 4.7. The relative rotation of two diffusers showed that the PSF width in this case gets convoluted with the diffraction rays from the first and second diffuser. From Fig. 4.9, it can be noticed that the PSF is more uniform in all the direction for $\phi = 30°$ and 150° and hence they have higher PSF width throughout the range of relative aperture sizes as shown in Fig.4.8.

The synthetic image generator showed good approximation for higher $f_{\#}$ (see Fig. 4.10) but smaller $f_{\#}$ the diffraction equation (Eq. 2.7) is not able to simulate the spherical aberration. Numerically generated PSF width have an offset of 0.8 pixels because the inputs are taken from the Table 4.1. Hence, due to magnification factor of 0.014, camera pixel pitch of 6.8 μm and geometrical diameter of 0.4 mm, the synthetic PSF width with no diffraction effect is 0.8 pixels.

The transmittance of diffusers when subjected to the white light were inspected with and without the *daylight filter*. The *daylight filter* allows only the green light to pass through them. Without the *daylight filters*, the transmittance of one and two diffusers were approximately 96% *w.r.t.* no diffusers. For *daylight filters*, there was almost no change in the transmittance of one and two diffusers compared to no diffusers. Hence, for PIV applications diffusers does not absorb any part of incident green light passing through them. The decrease in transmittance for diffusers without the *daylight filter* shows that the diffusers are sensitive to some other wavelength of light apart from the green light.

4.5 Conclusion

The diffusers have a significant effect on the particle image size compared to no diffusers. The particle image size increases by 40% and 55% for one and two diffusers ($\phi = 30°$ and 150°) respectively compared to no diffusers for the entire range of relative aperture. The change in the particle image size for different relative angles between the two diffusers was noteworthy. It was noticed that 30° and 150° have the largest PSF width because the diffraction of the incident ray on the camera image sensor was in all the directions. Also, the modified synthetic image generator showed a good agreement of the numerically assessed PSF width with its experimental counterpart for higher *f-stops*. The study of transmittance for one and two diffusers showed that 99% of the green light is retained by them compared to no diffusers.

Chapter 5

Experimental assessment of diffusers

Nothing takes place in the world whose meaning is not that of some maximum or minimum.

Leonhard Euler
(1707-1783)

The aim of the experiment presented in this chapter was to determine the efficiency of the optical diffusers in reducing the peak-locking error for actual PIV experiments. The experiments were carried out using planar PIV in an empty test-section (uniform flow), in the wake of a 2D cylinder (high-speed flow) and on the boundary layer of the test-section floor (low-speed flow). The test setup, data reduction techniques, results and conclusion for no, one and two diffusers under different experimental test cases are discussed in this chapter.

5.1 Test Setup

The test setup for the three test cases are described in this section. If d_τ <1 in uniform flow case, then the error due to peak locking is the most dominant source of error in the measured flow field. Hence, the experiment was done in uniform flow to clearly see the reduction in the magnitude of the bias error due to diffusers. The second experiment was done on the fully-developed wake of a 2D cylinder because peak-locking error is a major source of error in such 3D flows. Different relative angles for two diffusers were also tested in this test case. The third experiment was done on the boundary layer of the test section floor for two diffusers with 45° relative angle which showed a significant reduction in peak locking in the previous experiment. Also, a comparative study was done to see the efficiency of diffusers *w.r.t* defocusing.

5.1.1 Empty test-section

The PIV displacement estimation of a uniform flow in the empty test-section was analysed to see the effect of using no, one and two diffusers on the magnitude of the peak locking error. The experiment was conducted in the W-Tunnel of *Delft University of Technology* at a free-stream velocity of 15 m/s. A planar PIV setup was implemented with a *Quantronix Darwin-Duo* laser (Nd:YLF diode pumped, $\lambda = 527$ nm) mounted on a X-beam structure below the test-section to illuminate the field of view. A mirror directed the laser beam by 90° vertically upwards into the test-section. A negative spherical lens was used before the cylindrical lens to focus the laser sheet above the measurement plane. The laser sheet was illuminated at 2 mm offset (away form the camera) from the center of the test-section. A continuous seeding of the water-glycol droplet with a diameter of around 1 μm was used. Images were recorded from LaVision's *High Speed Star* 6 camera (CMOS, 1024 × 1024 pixels, 12 bits, pixel pitch 20 μm). The camera was equipped with a Nikon objective of 105 mm focal length. The magnification factor was 0.2. The active sensor size was cropped to 512 × 512 px^2. The time separation varied from 10 μs to 20 μs in steps of 2 μs for the $f_\# = 4$ and $f_\# = 8$.

A reference measurement was taken with slightly defocused particles at $f_\# = 11$ with time separation of 340 μs for better estimation of the in-plane displacement. For every test case, 500 images were acquired. Essential parameters of the experiment are summarized in Table 5.1.

Table 5.1: Essential parameters for the test case of empty test-section

Seeding	water-glycol droplet, 1 μm diameter
Illumination	Quantronix Darwin-Duo Nd:YLF laser
Recording device	LaVision High Speed Star 6
	(CMOS, 1024 × 1024 px^2, 20 μm pitch)
Imaging	*Nikon* objectives
	f = 105 mm lens
$f_\#$	4 and 8
Field of view	73 × 73 mm^2, 512 × 512 px^2
Acquisition frequency	0.25 kHz
Magnification factor	0.2
Number of images	500

5.1.2 Wake of a 2D cylinder

The PIV displacement estimation of a fully developed turbulent flow in the wake of a 2D cylinder was analysed to see the effect of using no, one and two diffusers on the magnitude of the peak locking error. The experiment was conducted in the W-Tunnel of *Delft University of Technology* at a free-stream velocity of 15 m/s. A *Quantronix Darwin-Duo* laser (Nd:YLF

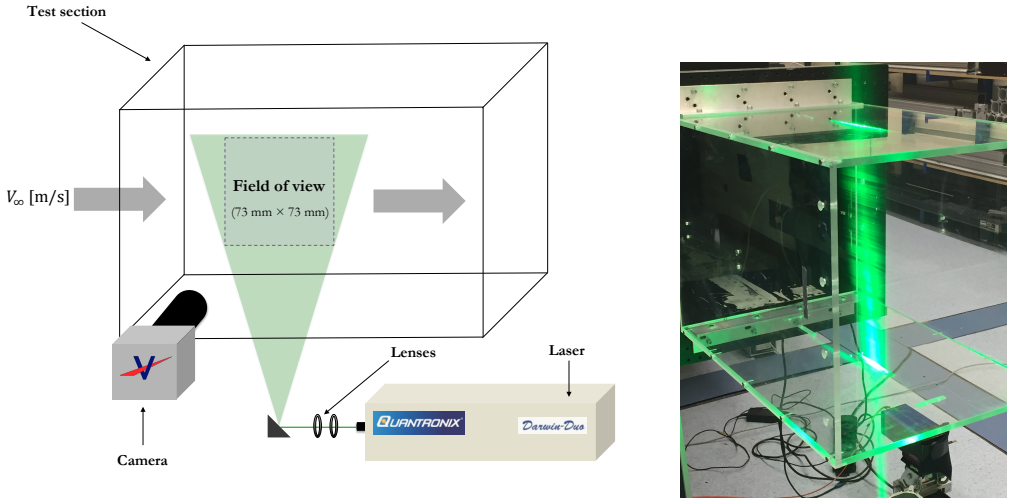

(a) Schematic test setup

(b) Actual test setup

Figure 5.1: Test Setup for the test case of empty test-section

diode pumped, $\lambda = 527$ nm) and the water-glycol droplets having an approximate diameter of 1 μm as the tracer particles was used. The PIV setup is similar to the empty test-section experiment as described in section 5.1.1. The FOV is positioned in the wake of the cylinder at a distance of 32 cm (4 times the diameter of the cylinder) from the center of the cylinder because the wake becomes highly turbulent in this region D. Jeon, M. Gharib (2004). The experiment was carried out for no, one and two diffusers at the time separation of 40 μs for the $f_\#$ values between 4 and 16.

For reference data, a Nikkon lens with 200 mm focal length was used for having higher dynamic range compared to the measurement data. Also, particles were slightly defocused with $f_\# = 11$ and the time separation of 100 μs was chosen for better estimation of the in-plane displacement. The magnification factor for reference data was 0.37. For every test case, 2000 images were acquired. Essential parameters of the experiment are summarized in Table 5.2.

5.1.3 Boundary layer of test-section floor

To study the effect of the diffuser and defocusing on the magnitude of peak locking error, an experiment in the boundary layer was carried out. The experiment was conducted in the W-Tunnel of *Delft University of Technology* at a free-stream velocity of 20 m/s. A *Mesa* PIV laser (Nd:YAG diode pumped, $\lambda = 532$ nm) and the water-glycol droplet having diameter of 1 μm as the tracer particles was used. The setup consists of a zig-zag tape on the test-section floor at a distance of 6.5 cm from the test-section's beginning edge. Images were recorded from LaVision's *High Speed Star* 6 camera (CMOS, 1024 × 1024 px^2, 12 bits, pixel pitch 20 μm). The camera was equipped with a Nikon objective of 105 mm focal length. The

Table 5.2: Essential parameters for the test case of wake of a 2D cylinder

Seeding	water-glycol droplet, 1 μm diameter
Illumination	Quantronix Darwin-Duo Nd:YLF laser
Recording device	LaVision High Speed Star 6
	(CMOS, 1024 $\times$ 1024 px^2, 20 μm pitch)
Imaging	*Nikon* objectives
	f = 105 mm lens (for measurement data)
	f = 200 mm lens (for reference data)
$f_\#$	4, 5.6, 8, 11 and 16
Field of view	73 $\times$ 73 mm^2, 512 $\times$ 512 px^2
Magnification factor	0.2 (for measurement data)
	0.37 (for reference data)
Acquisition frequency	0.25 kHz
Number of images	2000

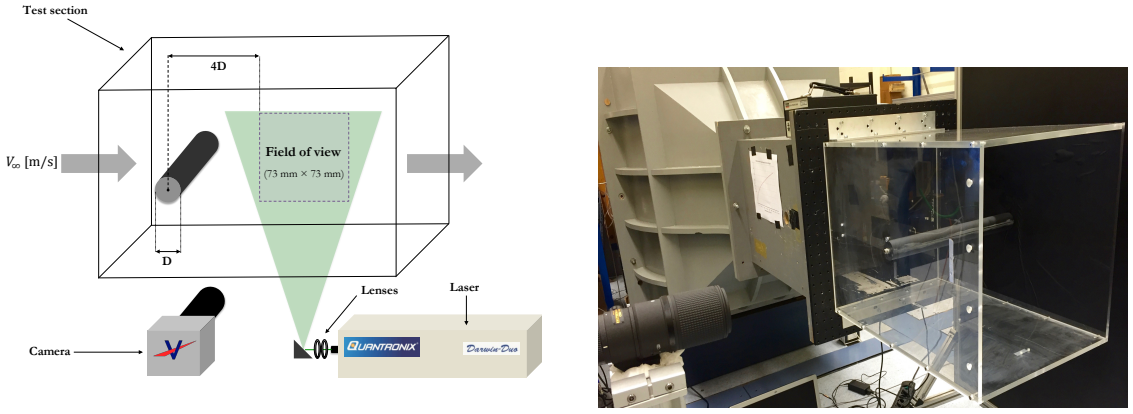

(a) Schematic test setup

(b) Actual test setup

Figure 5.2: Test Setup for the test case of wake of a 2D cylinder

magnification factor was 0.2. The active sensor size was kept at 512 $\times$ 512 px^2. The FOV is positioned on the center line of the test-section floor at a distance of 48.5 cm from the beginning edge of the test-section. The experiment was carried out for no and two diffusers at the time separation of 20 μs for $f_\# = 4$, 5.6 and 8. For reference data, time separation was kept as 80 μs for better estimation of the in-plane displacement. The particles were slightly defocused with $f_\# = 5.6$.

To study the effect of defocusing on the random error and the bias error, the camera was first focused on the laser sheet and the entire camera setup was shifted back from its initial position up to 25 mm. The data was acquired after every 5 mm shift of the camera position. The $f_\# = 4$ was used to keep a small depth of field (δz = 10 mm). For every test case, 2000 images were acquired. Essential parameters of the experiment are summarized in Table 5.3.

Table 5.3: Essential parameters for the test case of boundary layer of the test-section floor

Seeding	water-glycol droplet, 1 μm diameter
Illumination	Mesa PIV Nd:YAG laser
Recording device	LaVision High Speed Star 6
	(CMOS, 1024 $\times$ 1024 px^2, 20 μm pitch)
Imaging	*Nikon* objectives
	f = 105 mm lens
$f_\#$	4, 5.6 and 8
Field of view	73 $\times$ 73 mm^2, 512 $\times$ 512 px^2
Magnification factor	0.2 (for measurement data)
Acquisition frequency	0.25 kHz
Number of images	2000

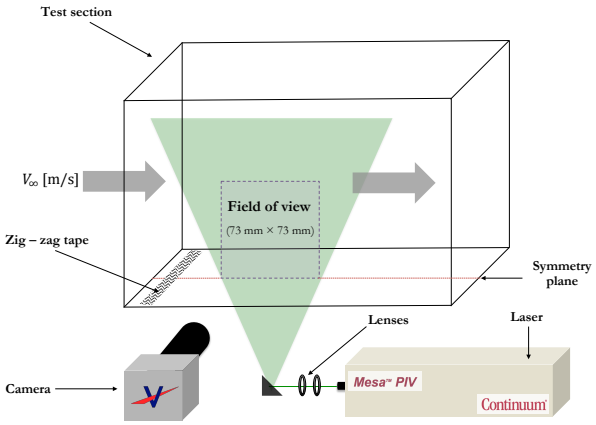

(a) Schematic test setup

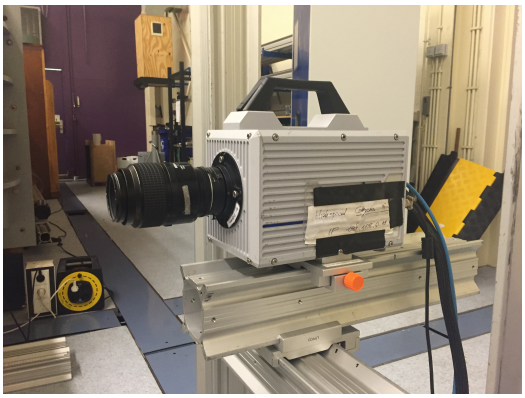

(b) Camera mounting for defocusing

Figure 5.3: Setup for the test case of boundary layer of the test-section floor

5.1.4 PIV Processing

The PIV software Davis 8.3.0 was used for PIV processing of the entire data acquired during experiments mentioned in section 5.1. For reducing the background image, a time filter was used to subtract the minimum intensity from all images. A window deformation iterative and multi-grid method (WIDIM) was used, starting with round window size of 64 $\times$ 64 px^2 with 50% overlap and ending with round window size of 16 $\times$ 16 px^2 with 75% overlap for the measurement data. For the reference data, WIDIM starts with round window size of

256 × 256 px^2 with 75% overlap and ends with round window size of 32 × 32 px^2 with 75% overlap. The multigrid algorithm uses a pyramid approach by starting off with a large interrogation window and refines to smaller window size after every pass. Also on the final multigrid pass, image deformation was used to enhance the spatial resolution of the image. This was done by sub-pixel image shifting based on the B-spline interpolation of order 6. The PIV interrogation windows were cropped from all the sides to eliminate any adverse edge effect of the PIV images.

5.2 Methodology

Various methodologies implemented to perform the objectives mentioned in the beginning of this chapter are described in this section. The bias error is determined from the difference between the mean of the measured displacement and the true displacement. Hence, it is important to calculate the true displacement satisfactorily to get a good estimation of the bias error.

5.2.1 True displacement for uniform flow

For the uniform flow case in an empty test-section, the reference displacement was acquired using a large time separation Δt (almost 30 times higher than the measurement case) for the wind tunnel speed which was kept constant throughout all the measurement cases. The particle displacement can be calculated as:

$$\Delta X_P \approx M v_p \Delta t \tag{5.1}$$

where X_p is the displacement position in image plane at the location p, M is the magnification factor, v_p is velocity vector at position p Ronald J. Adrian (1997) which is determined from the PIV processing. Higher Δt corresponds to larger displacement in the image plane, thus significantly reducing the impact of peak locking errors. Also the image was slightly defocused to increase the particle image diameter, which has been previously shown by J. Westerweel (2000) to reduce the bias error. Hence, with larger in-plane displacement and optimum image diameter, reference flow-field velocity is computed. Using Eq. 5.1 with different Δt, the expected true displacement was computed for all the measurement data.

5.2.2 True displacement for turbulent flow

In order to obtain the reference data for turbulent flow case, a dual range measurement was conducted with a measurement system and high dynamic range (HDR) system. This was done because they have 3-4 times higher digital imaging resolution compared to the measurement system. Also, the particle image diameter were kept at approximately two pixels. Thus improving the dynamic velocity range (DVR) nearly by a factor of 5 A. Sciacchitano (2014).

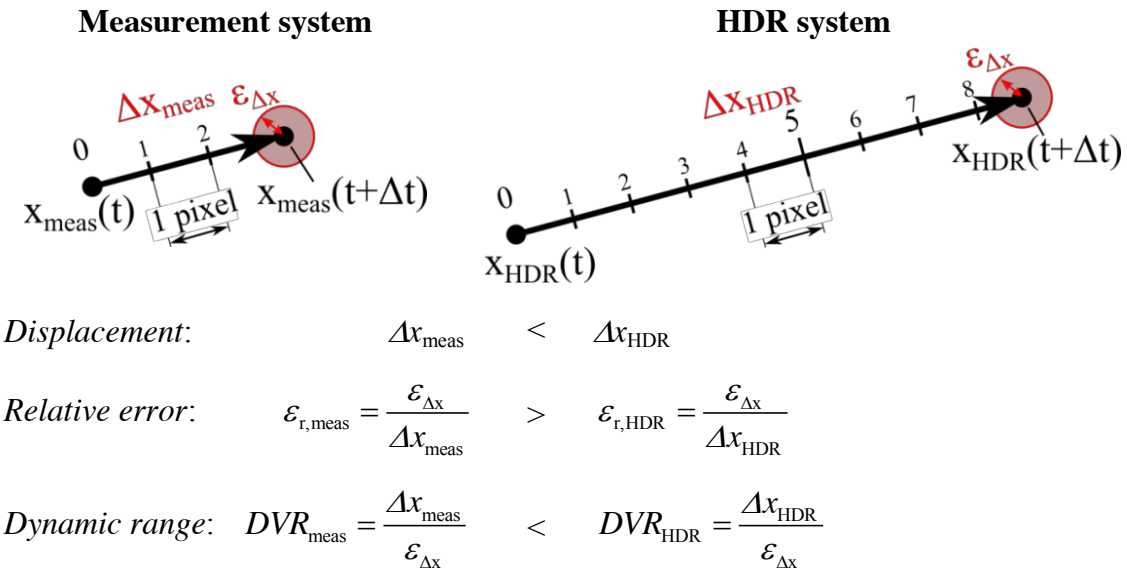

Figure 5.4: Comparison between measured and HDR system A. Sciacchitano (2014)

Fig. 5.4 shows that for the HDR system, a larger particle displacement in the image plane is discretized compared to the measurement system. Higher DVR in HDR system helps in reducing the error due to spatial discretization. Thus, with higher DVR and optimum particle image size, the velocity field retrieved from the HDR system can be considered as the reference velocity measurement.

5.2.3 True displacement for boundary layer

For the boundary layer, the reference data was acquired using slightly defocused particles and a large time separation Δt as discussed in section 5.2.1. This gives the true displacement for each interrogation window in the FOV of the boundary layer which starts from the test-section floor and ends at the point where the flow velocity asymptotically reaches the mean free stream velocity.

5.2.4 Diameter estimation

As discussed earlier, peak locking error highly depends on the particle image diameter. Hence, it is important to have an estimate of the particle image diameter from the PIV raw images for better understanding of measurement error propagation due to peak locking. The approach of Scot O. Warner (2012) is incorporated in the present work. Fig 5.5 shows the algorithm to estimate the mean particle image diameter.

The image was divided into interrogation window size of 32 $\times$ 32 px^2. An auto-correlation

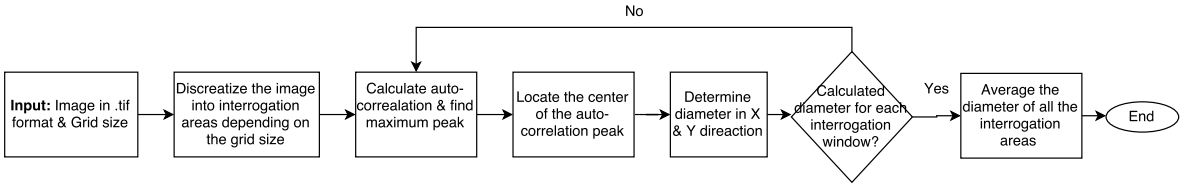

Figure 5.5: Flowchart for calculating particle image diameter

followed by the particle image diameter estimation is implemented in each window area independently. The theory related to the auto-correlation and particle image diameter estimation is explained in sub-section 4.2.1 and 4.2.2 respectively. The mean of particle image diameter from all the interrogation window is taken as the final value for better statistical convergence.

5.2.5 Degree of Peak locking

In a 1-D histogram of displacement, effect of peak locking can be distinctly observed. It evidently exhibits that the displacement is bias towards the integer values. The degree of pixel locking (C) helps quantifying peak locking in a universal way irrespective of the particle in-plane displacement range and particle counts E.F.J. Overmars, N.G.W. Warncke, C. Poelma and J. Westerweel (2010). Thus, helping in executing a comprehensive comparative study of different data sets. Eq. 5.2 shows the mathematical representation of the degree of peak locking.

$$C = 1 - \frac{N_{\min}}{N_{\max}} \tag{5.2}$$

where $N_{\min}$ and $N_{\max}$ are the lowest and highest number of particle counts in the fractional histogram, as illustrated in Fig 5.6. For better statistical result of the degree of peak locking, an entire range with in-plane displacement between 1 and 5 pixels is taken to have higher number of samples. By subtracting the nearest lower integral pixel value from every displacement values in the image helps in plotting a histogram which shows the peak-locking effect for the entire user-defined range of the in-plane displacement.

When C = 0, it indicates no peak-locking, while C = 1 is an indication of very severe peak-locking. Degree of peak-locking is classified into four stages, and are stated as follows,

1. C $<$ 0.2 : No peak locking
2. 0.2 $<$ C $<$ 0.4 : Mild peak locking
3. 0.4 $<$ C $<$ 0.6 : Strong peak locking
4. C $>$ 0.6 : Severe peak locking

A major limitation of this method is that it only works for turbulent flows where there is a higher range of particle displacement due to irregular fluctuations in the flow.

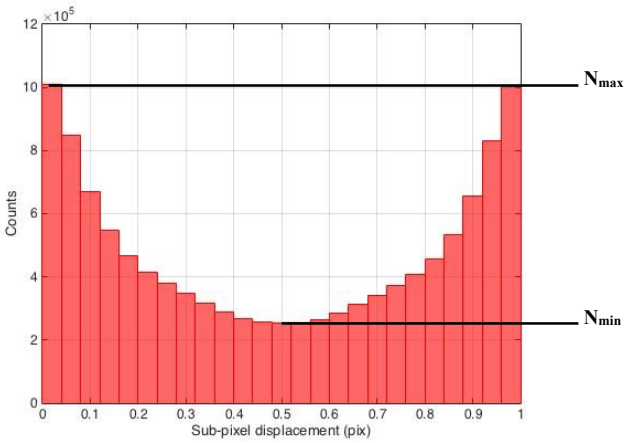

Figure 5.6: 1D histogram showing fractional displacement in pixel units with a bias towards integer value

5.3 Results

The outcome of diffusers on reducing the peak locking error under different flow cases and image diameter validation is presented in this section.

5.3.1 Image diameter estimation

In order to see how well does the particle image diameter estimation method works for various input parameters, synthetic images were generated with densities ranging from 0.01 ppp to 0.09 ppp in steps of 0.01 ppp and with particle image peak intensity constant at 1000 counts. The diameter estimation of a theoretical particle image diameter of 1 pixel and 3 pixels is shown in Fig. 5.7(a) and Fig. 5.7(b) respectively. From the figures, it is evident that for theoretical $d_\tau = 1$ pixel, the estimated d_τ is over-estimated by almost 60% throughout the image density values. However, in case of theoretical $d_\tau = 3$ pixels, the estimated diameter overshoots only by 20-25%.

5.3.2 Empty test-section

The consequence of diffuser on the bias error and the random error followed by change in particle image diameter and RMS velocity profile are discussed hereafter.

Bias error vs. sub-pixel displacement

The bias error as a function of sub-pixel displacement for $f_\# = 4$ and $f_\# = 8$ is shown in Fig. 5.8(a) and Fig. 5.8(b) respectively. Both the plots clearly indicates that the bias error is lowest at the integer values of displacement and significantly increases in case of sub-pixel

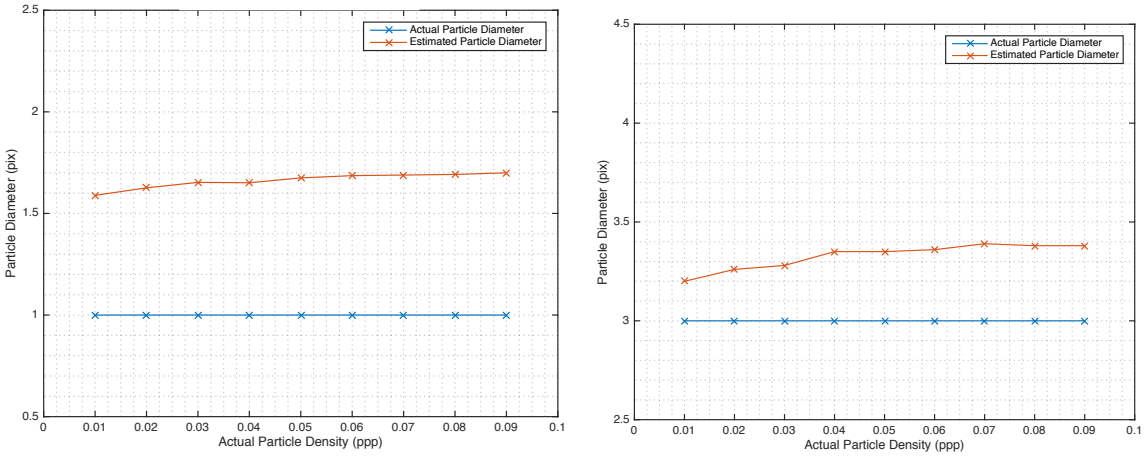

(a) Theoretical $d_\tau = 1$ pixel

(b) Theoretical $d_\tau = 3$ pixels

Figure 5.7: Estimated diameter as a function of image density

displacement. For no diffuser the bias error is the maximum which leads to severe bias error in the flow field results. In case of one and two diffusers, the amplitude of the bias error curve decreases by a factor of roughly two and three compared to no diffuser respectively. For $f_\# = 4$, the maximum amplitude of bias error is 0.13 pixels for no diffusers which decreases to 0.075 pixels and 0.04 pixels for one and two diffusers respectively. Similarly, for $f_\# = 8$, the maximum amplitude of bias error is 0.25 pixels for no diffusers which decreases to 0.12 pixels and 0.05 pixels for one and two diffusers respectively. Thus, showing a promising favourable effect of diffusers.

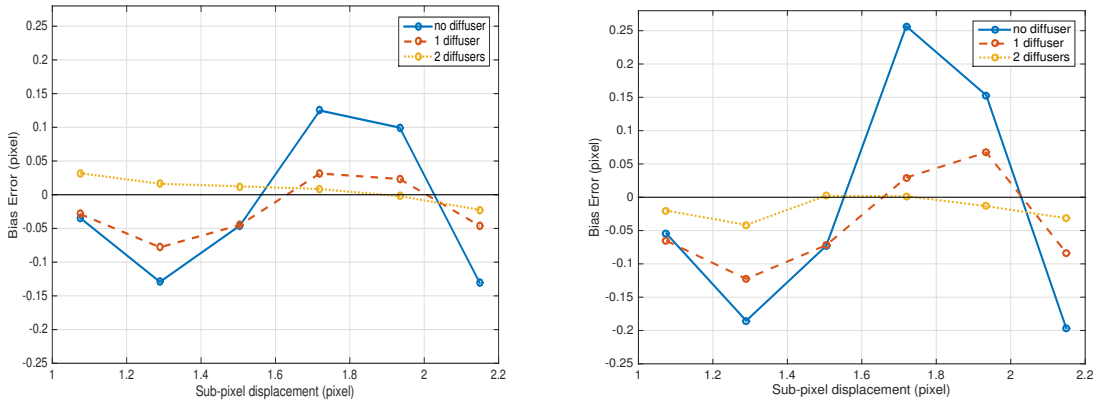

(a) $f_\# = 4$

(b) $f_\# = 8$

Figure 5.8: Bias error vs. sub-pixel displacement for 0/1/2 diffusers

Random error vs. sub-pixel displacement

The random error as a function of sub-pixel displacement with standard uncertainty S. Ahn and Jeffrey A. Fessler (2003) for $f_{\#} = 4$ and $f_{\#} = 8$ is shown in Fig. 5.9(a) and Fig. 5.9(b) respectively. For $f_{\#} = 4$, the maximum magnitude of the random error associated with no diffusers is 0.12 pixels which decreases to 0.058 pixels and 0.04 pixels for one and two diffusers respectively. For $f_{\#} = 8$, the maximum magnitude of the random error for no diffuser is 0.16 pixels which decreases to 0.11 pixels and 0.06 pixels for one and two diffusers respectively. Since the effective particle image diameter was kept as focused as possible, $d_\tau \approx 1$ pixels. The random error associated with smaller d_τ in the PIV images is notably higher (discussed in Section 2.6.2). Due to the effect of the diffuser, particle image diameter increases which causes the random error associated with the particle image diameter decrease.

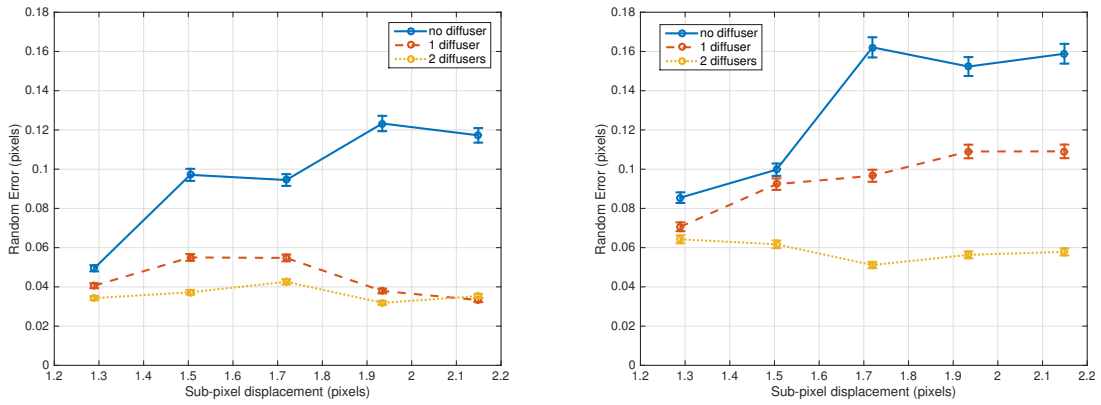

(a) $f_{\#} = 4$ (b) $f_{\#} = 8$

Figure 5.9: Random error vs. sub-pixel displacement for 0/1/2 diffusers with standard uncertainty

Diameter Estimation

The particle image diameter is estimated using the diameter estimator algorithm discussed in the section 5.2.4. The diameter was estimated for no, one and two diffuser for the PIV images at $f_{\#}$ equal to 4 and 8. The estimated particle image diameter as a function of $f_{\#}$ is shown in Fig. 5.10(a), where d_τ for two diffusers is significantly higher compared to no diffusers. Moreover, during the experiment, PIV images were taken at a very low seeding density to clearly see the increase in particle image diameter. A small cropped section of PIV raw images for no, one and two diffusers are shown in the Fig. 5.10(b), Fig. 5.10(c) and Fig. 5.10(d) respectively.

A captivating result was observed in Fig. 5.10(a) in which the particle image diameter is greater for $f_{\#} = 4$ and lower for $f_{\#} = 8$. This completely contradicts the directly proportional relation between the relative aperture size and the particle image diameter as shown in Eq. 2.8. In order to understand this anomaly, the autocorrelation function for one of the interrogation

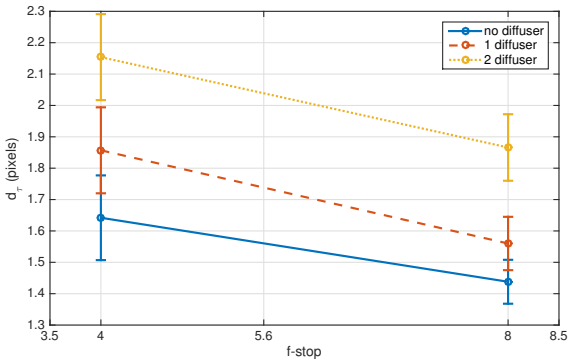

(a) Estimated d_τ vs. $f_\#$ with standard uncertainty

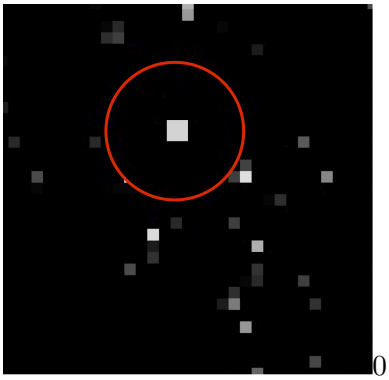

(b) No diffusers at $f_\# = 4$

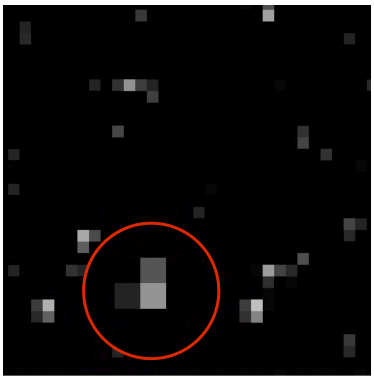

(c) One diffusers at $f_\# = 4$

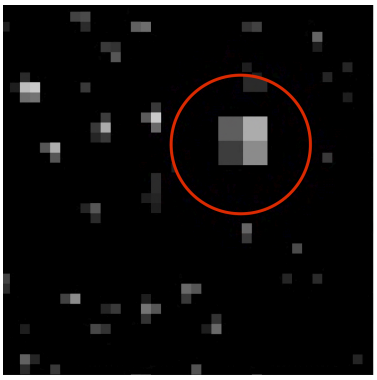

(d) Two diffusers at $f_\# = 4$

Figure 5.10: Diameter estimation for 0/1/2 diffusers when PIV image is peak-locked. For better visualization, a particle in each of these image is magnified which are encircled by the red band which clearly shows an increase in particle image diameter.

window is shown in Fig 5.11(a) and Fig 5.11(b) for $f_\# = 4$ and 8 respectively. The diameter is calculated at e^{-2} width because it comprises of 99% data values of the Gaussian curve. At $Y = e^{-2}$, it can clearly be seen that due to higher background noise the tail of the autocorrelation function for $f_\#$=8 is concealed in the background noise. Thus, the estimated diameter shows smaller d_τ for $f_\# = 8$. This effect of background noise was present in all the images for no, one and two diffusers at $f_\# = 8$.

RMS Velocity profile

The RMS velocity profile for uniform flow in an empty test-section is shown in Fig. 5.12. The velocity fluctuation is approximately 0.16 pixels for no diffuser due to peak-locking. For one and two diffusers, the velocity fluctuation decreased to 0.14 pixels and 0.07 pixels. This shows that the two diffusers helps in reducing the peak-locking error better compared to one diffuser. For reference velocity field there is a very minimal velocity fluctuation over the entire

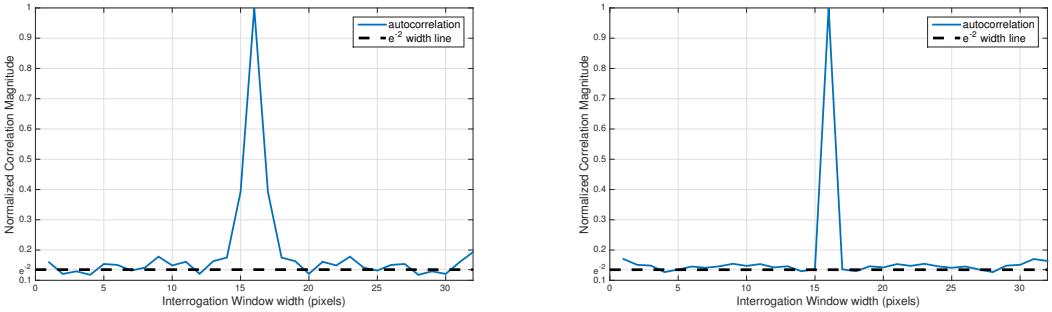

(a) $f_{\#} = 4$ (b) $f_{\#} = 8$

Figure 5.11: Normalized autocorrelation for no diffusers without the 3-point Gaussian fit

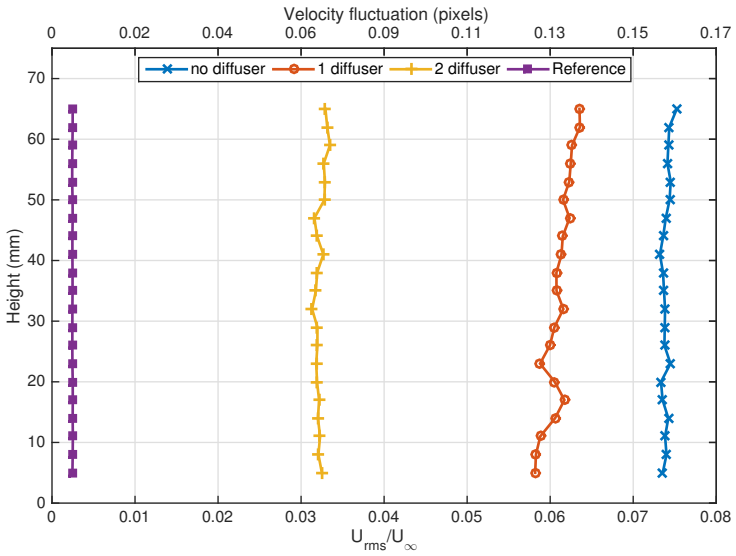

Figure 5.12: RMS Velocity profile for uniform flow in an empty test-section at $f_{\#} = 4$

height of the field of view.

5.3.3 Wake of a 2D cylinder

The consequence of one and two diffusers on the bias error and the random error for the wake of a 2D are presented in this subsection.

Histogram of PIV data for diffusers

The effect of peak locking at $f_{\#} = 8$ on the wake of a 2D cylinder for no, one and two diffusers are shown in the Fig. 5.13(a), Fig. 5.13(b) and Fig. 5.13(c) respectively. The sub-

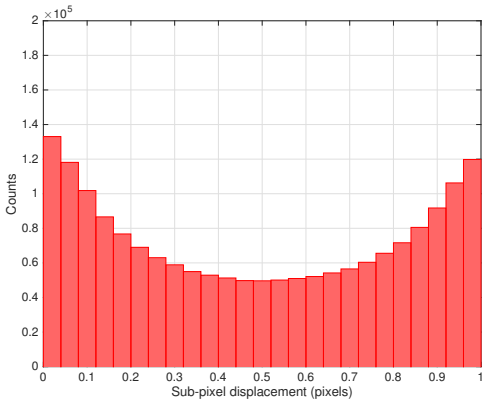

(a) No diffuser: C = 0.60

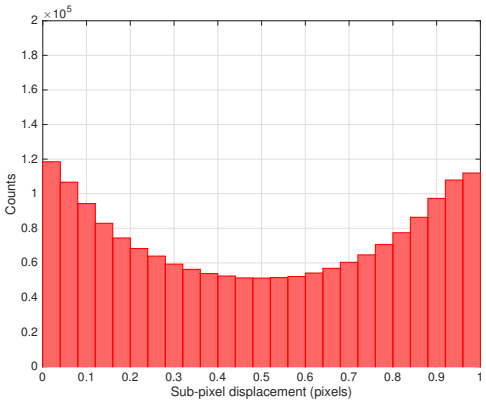

(b) One diffuser: C = 0.55

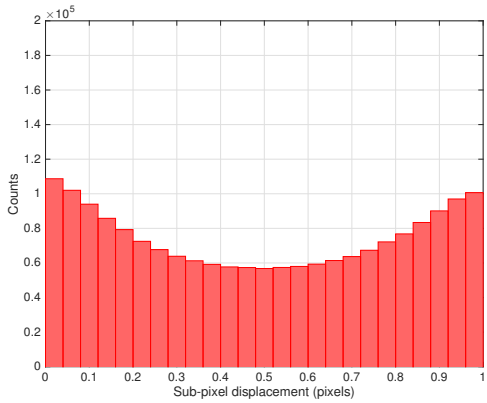

(c) Two diffuser ($\phi = 0°$): C = 0.45

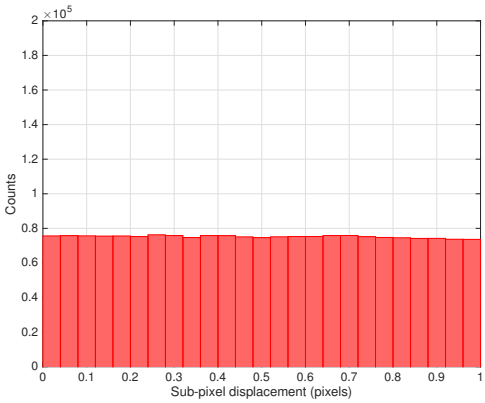

(d) Reference: C = 0.05

Figure 5.13: Histogram for sub-pixel displacement at $f_{\#} = 8$

pixel displacement range between 1 pixel to 5 pixels was considered for the calculation of 1D histogram. The reference measurement as discussed in section 5.2.2 is shown in Fig. 5.13(d). A strong peak at integral values of sub-pixel displacement is shown in Fig. 5.13(a). Thus, showing that the PIV data is severely peak locked. In Fig. 5.13(b), the peak strength decreases and the histogram slightly flattens because of the favourable effect of one diffuser. Nonetheless, the PIV data is dominated by peak-locking error. Fig. 5.13(c) shows the histogram for two diffusers at $\phi = 0°$, the difference between histogram of one and two diffuser is relatively small and does not help much in reducing the peak strength at integral values. Fig. 5.13(d) shows that the PIV data has a flattened histogram in the sub-pixel range. This shows that the reference velocity field has no peak locking.

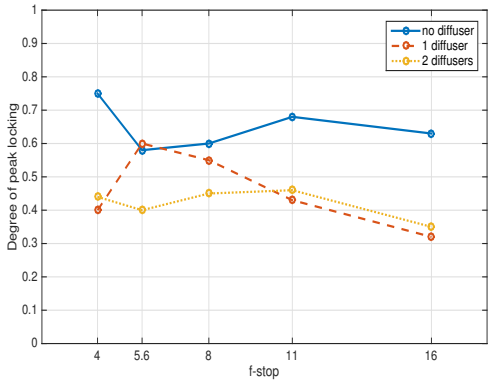

Figure 5.14: Degree of peak locking vs. *f-stop*

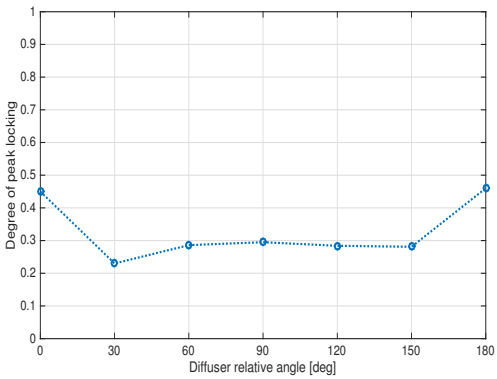

Figure 5.15: Degree of peak locking for different diffuser angles at $f_{\#} = 8$

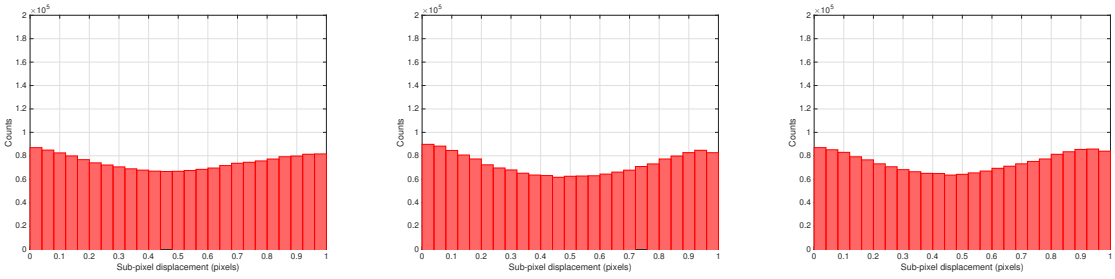

(a) $\phi = 30°$: C = 0.23 (b) $\phi = 60°$: C = 0.29 (c) $\phi = 90°$: C = 0.30

Figure 5.16: Histogram for two diffusers with relative angle (ϕ) at $f_{\#} = 8$

Degree of peak locking for diffusers

The degree of peak locking was calculated from the histograms as shown in Fig.5.13. It was calculated for 0/1/2 diffusers for all the $f_{\#}$ between 4 and 16 as shown in Fig. 5.14. From the graph, it is noticeable that the decrease in degree of peak locking is same for one and two diffusers for $f_{\#} > 11$. For $f_{\#} = 5.6$ and 8, the degree of peak locking is least for two diffusers.

Degree of peak locking for varied diffuser angles

For $f_{\#} = 8$, the change in degree of peak locking was also studied for the relative angle of the two diffusers between 0° and 180° in steps of 30° as shown in Fig. 5.15. The degree of peak locking is approximately 0.23 for 30° which is considered as very mild peak locking (*refer* section 5.2.5). Also, a symmetric nature of degree of peak locking can be seen about the vertical axis at $\phi = 90°$.

A 1D histogram for two diffusers at $\phi = 30°$, $60°$ and $90°$ at the $f_{\#} = 8$ on the wake of a 2D cylinder is shown in Fig. 5.16(a), Fig. 5.16(b) and Fig. 5.16(c) respectively. At $\phi = 30°$, the histogram is almost flattened and shows the highest reduction in peak-locking error.

RMS Velocity profile

The RMS velocity profile for the wake of 2D cylinder is shown in Fig. 5.17. The data for no, one and two diffusers at $\phi = 0°$ and $30°$ is taken at $f_{\#} = 8$. The velocity fluctuation in case of no diffuser have highest amplitude which is due to peak-locking. However for the use of diffusers, it is difficult to make any concrete inference because the range of the RMS profile is too small.

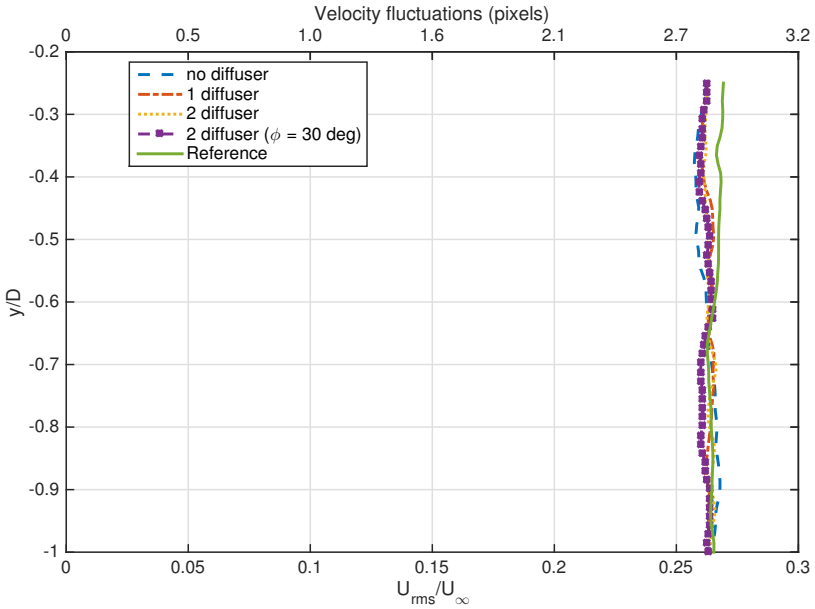

Figure 5.17: RMS Velocity profile for turbulent flow in the wake of 2D cylinder at $f_{\#} = 8$

5.3.4 Boundary layer of the test-section floor

The results of the effect of two diffusers ($\phi = 45°$) and defocusing on the bias error and random error for the boundary layer of the test-section floor is discussed hereafter.

Degree of peak locking

The degree of peak locking was calculated for 0/2 diffusers and different camera position for defocusing as shown in Fig 5.18 and Fig. 5.19 respectively. In Fig. 5.18, no diffuser test case have a severe peak locking which remains constant for all the $f_{\#}$. For two diffusers ($\phi = 45°$), the degree of peak locking decreases with respect to no diffusers and further reduces as $f_{\#}$ increases. As the camera is moved from focused position (0 mm) to defocused position (25

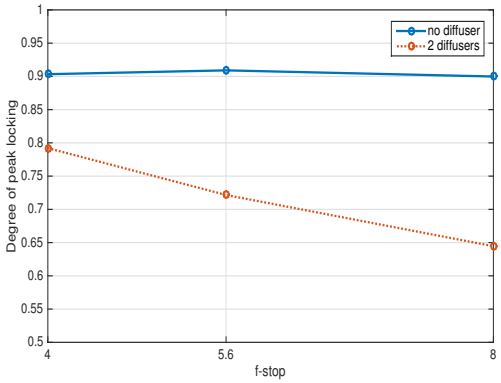

Figure 5.18: Degree of peak locking vs. $f_{\#}$ for no and two diffusers

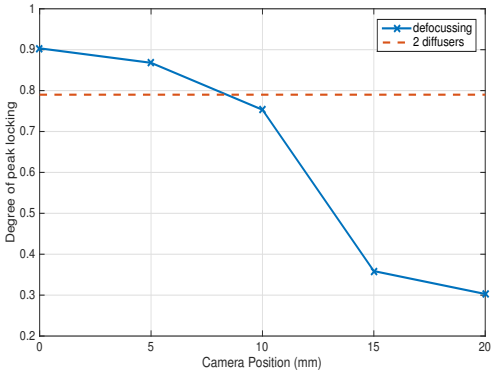

Figure 5.19: Degree of peak locking at $f_{\#} = 4$ for camera positions without diffuser and for two diffusers at 0 mm camera position

mm), the degree of peak locking for $f_{\#} = 4$ significantly reduces as shown in Fig. 5.19. The dashed red line shows the degree of peak locking for the camera at 0 mm position with two diffusers at $f_{\#} = 4$. The degree of peak locking is 0.79 for two diffusers ($\phi = 45°$) is slightly higher compared to 0.77 for the camera position 3 (10 mm).

Random error vs. f-number and camera positions

To shed more light on the comparative assessment of diffusers and defocusing, the random error was calculated for 0/2 diffusers and different camera position as shown in Fig. 5.20 and Fig. 5.21 respectively. In Fig. 5.20, the diffraction limit tends to increase aberrations leading to a larger and asymmetric particle image diameter in the image M. Megerle, V. Sick and David L. Reuss (2002) which causes the random error to gradually increases when $f_{\#}$ increases. The particle image diameter are slightly bigger due to diffusers and the random error associated with it is also higher compared to no diffusers. In Fig. 5.21, the random error decreases from 0.05 pixels to 0.035 pixels when the camera is moved from 0 mm to 5 mm because peak locking is dominant at 0 mm position which gives erroneous displacement values. When camera is moved from 5 mm to 10 mm, the random error remains almost the same and then shoots up as the camera is moved from 10 mm to 25 mm position. This behaviour of the random error shows that it has no significant effect when the images are slightly defocused. But as the defocusing increases there is an exponential jump in the random error because defocusing further enlarges the images and reduces the image quality. The random error for two diffuser is practically same compared to the camera position 3 (10 mm).

Bias error vs. sub-pixel displacement

The bias error as a function of true displacement for no diffusers, two diffusers and camera position 3 for $f_{\#} = 4$ is shown in the Fig. 5.22. For no diffusers, a sinusoidal nature of the bias error can be seen where bias error is minimum towards integer displacement values. The

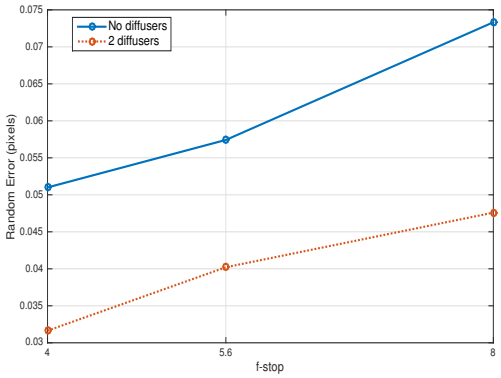

Figure 5.20: Random error vs. $f_\#$ for no and two diffusers

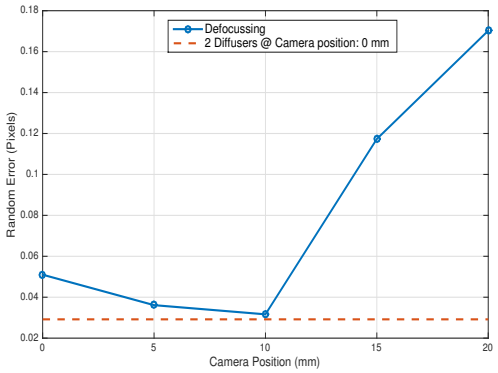

Figure 5.21: Random error at $f_\# = 4$ for camera positions without diffusers and two diffuser at 0 mm camera position

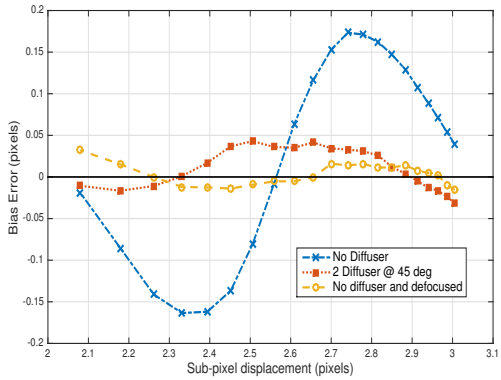

Figure 5.22: Bias error for no diffuser, 2 diffusers and defocusing at $f_\# = 4$

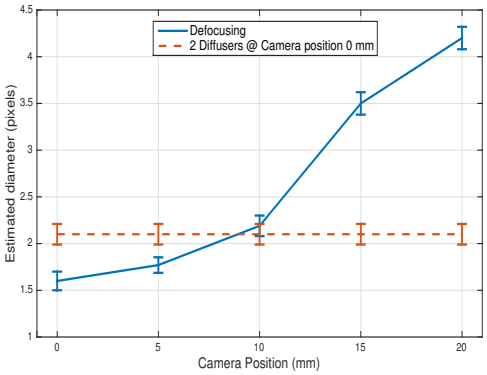

Figure 5.23: Diameter estimation for camera positions and 2 diffusers at $f_\# = 4$ with standard uncertainty

amplitude of the bias error is 0.18 pixels in sub-pixel displacements. For two diffuser and camera position 3, the amplitude of the bias error is almost 0.05 pixels. In this case, d_τ = 2.2 pixels and 2.1 pixels for two diffusers and defocusing respectively.

Diameter Estimation

The particle image diameter is estimated for various camera positions shown in Fig. 5.23 using the diameter estimator algorithm discussed in section 5.2.4. The estimated d_τ gradually increases from 1.5 pixels at camera position 1 (0 mm) to 2.2 pixels camera position 3 (10 mm). The particle image diameter increases exponentially to 3.5 pixels and 4.2 pixels for camera position 4 (15 mm) and 5 (20 mm) respectively. The sudden increase in particle image diameter is due to the fact that images were acquired at $f_\# = 4$ which have $\delta z = 10$ mm. Thus, the image becomes blur and reduces the image quality marginally when the camera

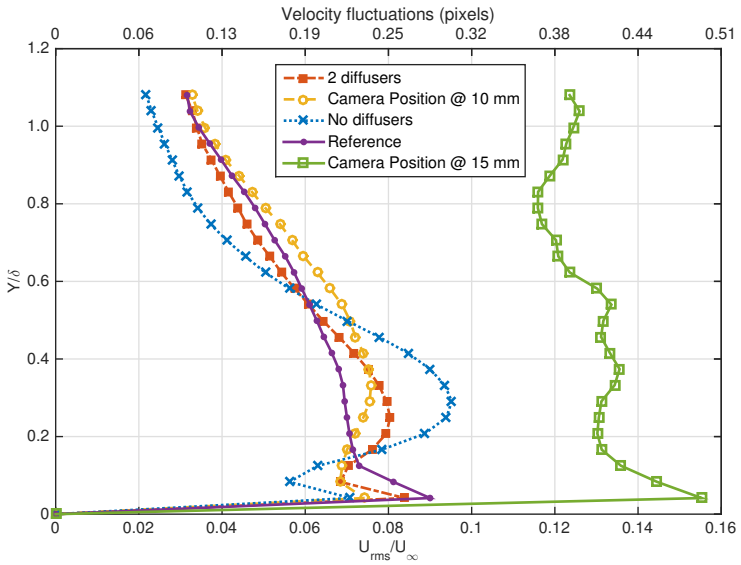

Figure 5.24: RMS Velocity profile for boundary layer of the test-section floor @ $f_{\#} = 4$

is moved past the 10 mm position. The estimated diameter for two diffusers at the camera position of 0 mm and $f_{\#} = 4$ is 2.1 pixels.

RMS Velocity profile

The RMS profile for no diffusers, two diffusers, camera position 3 (10 mm) and 4 (15 mm) for $f_{\#} = 4$ is shown in Fig. 5.24. The shear velocity in the boundary layer decreases as one moves away form the floor. At the floor ($Y/\delta = 0$) shear velocity is zero because of the no-slip condition. The velocity fluctuations in the second peak is highest for no diffuser due to peak-locking error. For two diffusers and camera position 3 the velocity fluctuation is lesser compared to no diffusers. In both cases, there is still some peak locking effect present when compared to the reference data. For the camera position 4, the RMS profile is completely incorrect because excessive defocusing reduces image quality and reduces signal-to-noise ratio in the image.

5.4 Discussion

The important results and anomalies in the results are discussed in this section.

5.4.1 Image diameter Estimation

The estimated particle image diameter for actual $d_\tau = 1$ pixel is overestimated (see Fig. 5.7(a)) because of the mathematical limit of the Gaussian fit and is explained hereafter. Mathemat-

ically Gaussian fit can be written as:

$$f(x) = e^{\frac{-x^2}{2\sigma^2}} \tag{5.3}$$

where x is the input variable and σ is the standard deviation. Let us consider theoretical d_τ = 1 pixel. The autocorrelation for this case would have maximum intensity at the center of the correlation plane ($x = 0$) and the 3-point Gaussian fit will take the coinciding correlation points ($x = 1$ and $x = -1$) from the center into account as well. Thus, at $y = e^{-2}$ width, x $\approx$ 1 which can be written using Eq. 5.3 as follows:

$$e^{-2} = e^{\frac{-1}{2\sigma^2}} \tag{5.4}$$

After simplifying the above equation and putting it in Eq. 4.4, the estimated diameter for theoretical $d_\tau = 1$ pixel is:

$$\text{estimated } d_\tau \approx \sqrt{2} \text{ pixels} \tag{5.5}$$

However, when d_τ >1 pixel, adjacent peaks to the autocorrelation peak are also the component of the actual particle image diameter and hence gives a realistic estimation of the particle image diameter as shown in Fig. 5.7(b).

5.4.2 Empty test-section

A strong effect of the bias error on the true displacement displacement was seen for no diffuser in Fig. 5.8(a) and Fig. 5.8(b). For actual pixel displacement 1 <ϵ_{bias} <1.5 pixels, the bias error is negative which means that the measured displacement is biased towards 1 pixel. For actual pixel displacement 1.5 <ϵ_{bias} <2 pixels, the bias error is positive which means that the measured displacement is biased towards 2 pixels. For one and two diffusers the amplitude of bias error decreases because of the favourable effect of the optical which increases the particle image diameter without altering the magnification factor. An interesting feature was noted in the bias error for $f_\# = 4$ and $f_\# = 8$, the amplitude of bias error was higher for the latter compared to the former. Also the d_τ of the $f_\# = 4$ was higher which contradicts the direct relationship between particle image diameter and f-number. This was explained by their autocorrelation function shown in Fig. 5.11(a) and Fig. 5.11(b) which clearly showed that due to higher level of background noise the tails of the function was submerged in the background noise. This could have been avoided by increasing the laser power during the image acquisition. However, due to lower d_τ at $f_\# = 8$, the bias error and random error have higher amplitude of error compared to the error estimation for $f_\# = 4$. The random error for no diffuser as shown in Fig. 5.9(a) and Fig. 5.9(b) is higher compared to one and two diffuser because there is a higher uncertainty in the location of particle with respect to true displacement while calculating the random error using Eq. 2.13.

5.4.3 Wake of a 2D cylinder

The degree of peak locking significantly reduced from 0.60 for no diffusers to 0.23 for two diffusers at $\phi = 30°$. In Fig. 5.14, the degree of peak locking showed reduction in peak

locking with the use of one and two diffusers. An anomaly in the trend of degree of peak locking was noticed for $f_{\#}$ between 4 and 8. Also, two diffusers at $\phi = 0°$ did not show marginal reduction the in peak-locking error compared to one diffuser. From the results of Fig. 5.15, it was noticed that the two diffusers at a relative angle of 30° works better in reducing the peak locking error. The RMS velocity profile shown in Fig.5.17 failed to show a clear indication of reduction in velocity fluctuation for two diffusers. This might be due to the fact that there are higher flow velocity fluctuations of 2.5 - 3 pixels due to von Karman vortex sheet present in the fully developed turbulent wake of the cylinder which overshadows the peak locking velocity fluctuation of 0.5 pixels.

5.4.4 Boundary layer of the test-section floor

This experiment was designed based on the results obtained by the previous test case of the 2D cylinder. In order to have a test case where peak locking is the dominant error source, boundary layer test case was considered as it has lower flow velocity fluctuations. Also, the degree of peak locking was again checked for $f_{\#}$ between 4 and 8 which did not show a clear trend in the previous test case. Moreover, a comparative test was done for the two diffusers and defocusing to check the significance of using the former over the latter. In Fig. 5.18, the degree of peak locking for no diffuser is almost constant for increasing *f-stop* because the theoretical d_τ is <1 for $f_{\#} = 4$ to 8. Hence, the actual particle image diameter is approximately 1 pixel in all the three cases. For two diffusers, the degree of peak locking decreases with increase in $f_{\#}$ because d_τ is directly proportional to f-number and d_τ >1 pixel in this case. Fig. 5.19 and Fig. 5.21 shows that the defocusing marginally reduces peak-locking but in turn increases random error because of enlarged particles as discussed by J. Westerweel (1997). Larger d_τ leads to lower signal-to-noise ratio, the cross-correlation function is no longer able to determine the particle displacement accurately. The RMS velocity profile in Fig.5.24 shows that the velocity fluctuation for two diffuser ($\phi = 45°$) at camera position 1 (0 mm) and for no diffusers at camera position 3 (10 mm) is closest to the velocity fluctuations of the reference data.

5.5 Conclusion

In this chapter, a detailed experimental study on the effect of diffusers for different flow cases was performed. The amplitude of the bias error in Fig. 5.8 for uniform flow decreased by factor of two and three for one diffuser and two diffusers respectively with respect to no diffusers. Also in Fig. 5.9 a reduction in random error by a factor of approximately three for two diffusers with respect to no diffusers was noticed. In Fig. 5.10 because of the beam splitting property of diffusers, an increase in the particle image diameter for one and two diffusers was captured in PIV images with low seeding. Further analysis of diffusers in turbulent flow case showed that the decrease in degree of peak locking is relatively less for one and two diffusers ($\phi = 0°$) compared to no diffusers. Moreover, degree of peak locking was similar for one and two diffusers for $f_{\#}$ higher than 11 as showed in Fig. 5.14. However, it was interesting to notice in Fig. 5.15 that there was mild peak-locking when relative angle (ϕ) between two diffusers

was 30° and 150°. Later it was notified by LaVision that relative angle of 45° gives the best result in reducing peak locking which concurred with the results obtained in the present work. Thus, the experiment on the boundary layer of the test section floor was done using two diffusers ($\phi = 45°$) and was compared to the conventional defocusing method which is generally used to reduce the peak locking error. The final result showed that the effect of two diffusers at an angle of 45° is almost similar to the perfect defocusing of the tracing particles. The bias error and the random error decreased by a factor of three. The RMS velocity profile also showed that both of them have similar velocity fluctuations compared to the reference data. The main advantage of using two diffusers is that it saves the experimentalist from the tricky defocusing of the lens which is very important to keep the errors minimal.

Chapter 6

Experimental assessment of the measurement error due to peak-locking

Nature laughs at difficulties of integration.

Pierre-Simon Laplace
(1748-1827)

The aim of the experiment was to see the effect of the random errors and the bias errors for various $f_{\#}$ in a planar PIV setup using two different CCD cameras. This chapters contains the test setup, data reduction techniques, results and conclusion of the experiment.

6.1 Test Setup

The uniform flow in an empty test section was analysed to see the magnitude of the peak-locking effect. The experiment was conducted in *German Dutch Wind tunnel*'s (DNW) commercial closed loop Low-Speed Wind Tunnel (LST) at the free-stream velocity of 10 m/s and 20 m/s. A *Quantel Evergreen Bigsky* laser (Nd:YAG diode pumped, $\lambda = 527$ nm) was mounted on the tunnel ceiling. The laser sheet was generated using a 60 mm cylindrical lens. A positive and a negative spherical lenses were used before the cylindrical lens to focus the light sheet below the measurement plane. A mirror directed the sheet down to the tunnel through a small slot in the upper turntable. The sheet was aligned with the tunnel flow direction. A Laskin nozzle seeding generator using the DEHS (Di(2-ethylhexyl)sebacate, sebacic acid) resulting in particle diameter of almost 1 μm was used for flow seeding. Seeding was applied for a short amount of time in the tunnel since the seeding remains in the circuit for a long time. For velocity reference, a pitot tube was installed at 50 cm behind the center of the PIV plane.

The camera was mounted at an angle of 35° at the height of 100 mm above the tunnel floor on the port side of the wind tunnel wall. A *PCO 2000* (CCD, 2048 × 2048 px^2, 14 bits, pixel pitch 7.4 μm) as well as a *PCO Sensicam QE* camera (CCD, 1376 × 1040 px^2, 12 bits, pixel pitch 6.45 μm) were used separately for the experiment. The cameras had free optical access to the plane through an opening in the wind tunnel wall. The optical axis was pointed to a point x: -100 mm and z: 0 mm compared to the tunnel center. A scheimplfug adapter was mounted to the camera. Cameras were rotated 90° around their optical axis. Also a 532 nm bandpass filter was used in all the test cases. Both the 200 mm and 100 mm focal length Nikon objectives were used in the wind tunnel test. A calibration grid (grid pitch 5 mm) was used to correct for perspective distortion. Upon inspection, the grid pitch was measured with a ruler to be slightly smaller (34.92 cm instead of 35 cm). The experiment was carried for three different camera setup, namely *PCO 2000* with f = 200 mm, *PCO 2000* with f = 100 mm and *PCO Sensicam* with f = 100 mm. For all the cases, 80 images were acquired at all the available relative apertures between 2 and 11. Essential parameters of the experiment are summarized in Table 6.1.

Table 6.1: Essential parameters for uniform flow with camera at 35° angle

Seeding	DEHS, 1 μm diameter
Illumination	Quantel Evergreen Bigsky Nd:YAG laser
Recording device	PCO 2000 (CCD, 2048 × 2048 px^2, 7.4 μm pitch)
	PCO Sensicam QE (CCD, 1376 × 1040 px^2, 6.45 μm pitch)
Imaging	*Nikon* objectives
	f = 100 mm and 200 mm lenses
Field of view	100 × 100 mm^2, 2048 × 2048 px^2 (for *PCO 2000*)
	60 × 45 mm^2, 1376 × 1040 px^2 (for *PCO Sensicam QE*)
Magnification factor	0.15
Number of images	80

6.1.1 PIV Processing

The PIV processing software used for this experiment is PIVview (PIVTEC, Gottingen, Germany). Throughout the chapter, same PIV processing steps are used. No filters were used in the image pre-processing. The window deformation iterative and multi-grid method was used having initial sampling window size of 128 × 128 px^2 with 50% overlap and going down to final window size of 32 × 32 px^2 with 50% overlap. This was done by sub-pixel image shifting based on B-spline interpolation of order 6. The PIV interrogation windows were cropped from all the sides to eliminate any adverse edge effect of the PIV images.

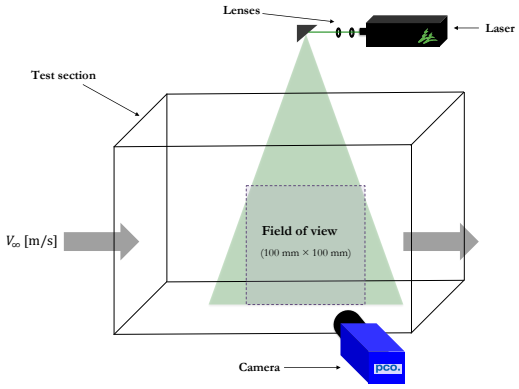

(a) Schematic test setup

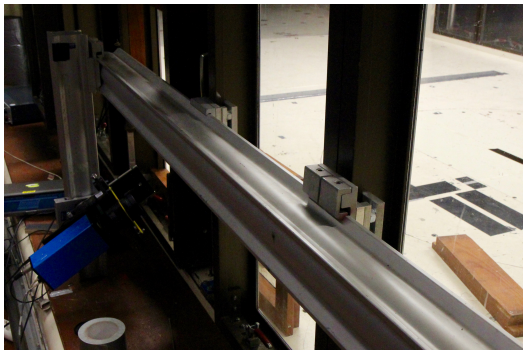

(b) Camera mounted at 35° *w.r.t.* the test-section floor

Figure 6.1: Test Setup for experiment on the measurement error due to peak-locking

6.2 Methodology

For determining the bias error, the true displacement must be known. The true displacement can be directly calculated using Eq. 5.1 and the wind tunnel speed. Since the camera was fixed at an angle *w.r.t.* z-axis, the local magnification on the image plane is different at each point due to perspective distortion. To determine the bias error in this case, the true displacement value was calculated from inverse of the transformation matrix and compared to the displacement from the PIV interrogation of the raw image.

This approach was implemented because using PIV raw images directly does not require image re-sampling F. Scarano, L. David, M. Bsibsi, D. Calluaud (2005). Resampling causes a change in the pixel dimensions of an image due to either by down-sampling or by up-sampling which changes the measured particle displacement during the image acquisition. Hence, it is necessary to avoid interpolation of the image to study the peak locking effect in sub-pixel displacement.

The implemented algorithm and intermediate results for better understanding of the steps taken is shown in Fig. 6.2. The reconstruction and calibration of the image is based on the approach proposed by S. M. Soloff, R. J. Adrian and Z-C Liu (1997). The mapping function (A) maps the coordinates from the object plane to the image plane. The coefficients of mapping function is determined from a calibration plate image. The nine unknown coefficients are determined using least square approach. Next, the image space (x, y) was created which contains the coordinates of user-defined interrogation windows placed equidistantly. To determine the coordinates of the interrogation windows in the object plane, inverse of mapping function is multiplied to the image plane as shown in Eq. 6.1

$$\begin{bmatrix} X \\ Y \end{bmatrix} = [B] \cdot \begin{bmatrix} x \\ y \end{bmatrix} \tag{6.1}$$

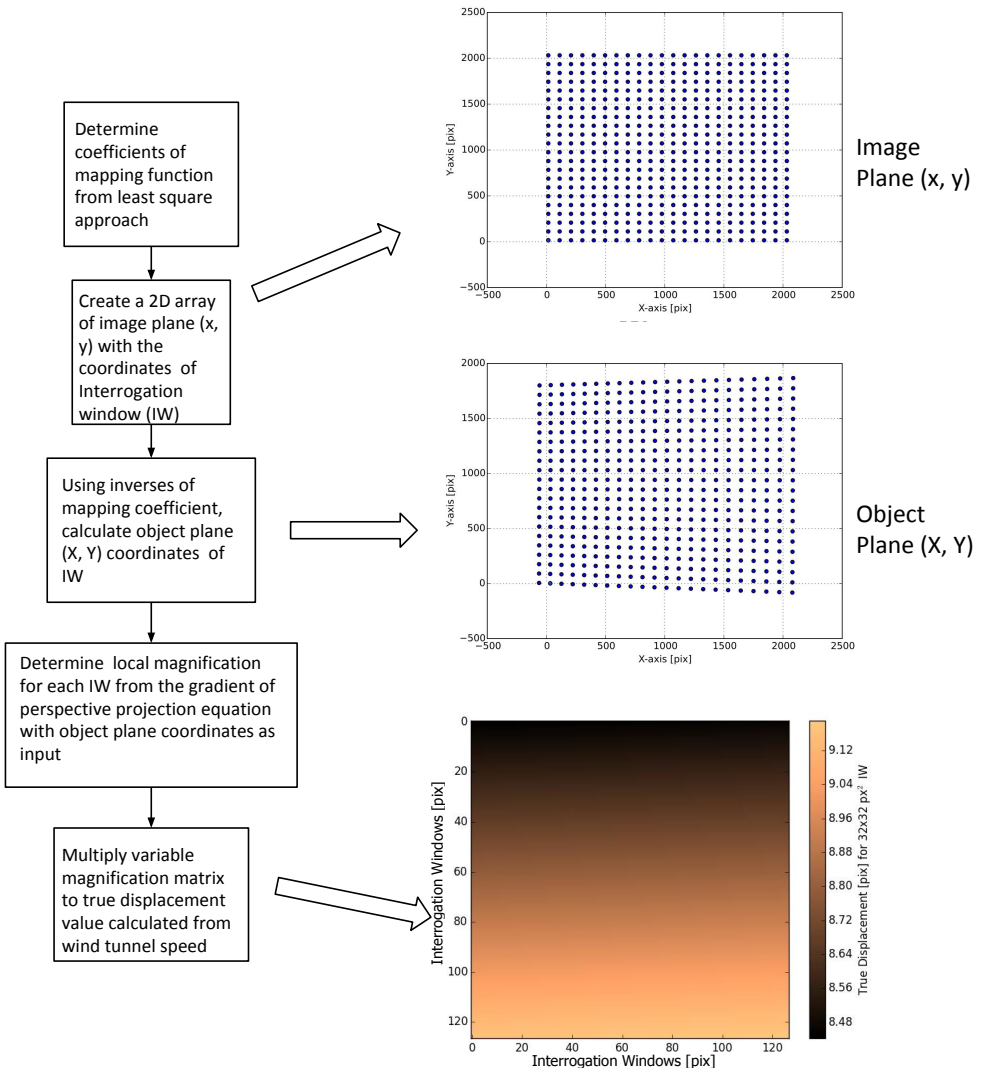

Figure 6.2: Flowchart for calculating true displacement with variable magnification

where,

$$[B] = [A]^{-1} \tag{6.2}$$

Eq 6.1 can be expanded as:

$$X = \frac{b_{11}x + b_{12}y + b_{13}}{b_{31}x + b_{32}y + b_{33}} \tag{6.3}$$

$$Y = \frac{b_{21}x + b_{22}y + b_{23}}{b_{31}x + b_{32}y + b_{33}} \tag{6.4}$$

To determine the local magnification for each interrogation window in image plane, gradient of perspective projection of the object plane in y-direction *w.r.t.* to x-direction is calculated. The equation is expressed as:

$$y = \frac{a_{21}X + a_{22}Y + a_{23}}{a_{31}X + a_{32}Y + a_{33}} \tag{6.5}$$

$$\frac{\partial y}{\partial X} = \frac{\partial}{\partial X} \cdot \left(\frac{a_{21}X + a_{22}Y + a_{23}}{a_{31}X + a_{32}Y + a_{33}} \right) \tag{6.6}$$

$$\frac{\partial y}{\partial X} = \frac{a_{21} \cdot (a_{31}X + a_{32}Y + a_{33}) - a_{31} \cdot (a_{21}X + a_{22}Y + a_{23})}{(a_{31}X + a_{32}Y + a_{33})^2} \tag{6.7}$$

By multiplying $\frac{\partial y}{\partial X}$ with true displacement calculated from the wind tunnel speed gives the true displacement with variable magnification throughout the image.

6.3 Results

The bias error and random error results calculated from the data acquired in this experiment is discussed hereafter.

6.3.1 Bias Error

The bias error as function of sub-pixel displacement for the different camera and lens combinations for $f_{\#}$ of 5.6 are shown in Fig. 6.3(a), Fig. 6.3(b), Fig. 6.3(c). In all the three cases, it is evident that bias error is minimal towards integer displacement values and significantly increases in case of sub-pixel displacement. Each data set in the aforementioned figure represents the gradient of velocity field present over the entire image. In the Fig. 6.3(b), there is a clear offset in the graph, which might be due to incorrect calibration plate measurement. For visual reference a corrected bias error is plotted on the right-hand side Y-axis of the figure. The *Data Set 1* and *Data Set 2* does not represent the true nature of the amplitude of bias error for a relative aperture. Hence, they will be considered as an anomaly and would not be contemplated in making any conclusions from figures. In Fig. 6.3(a), Fig. 6.3(b) and Fig. 6.3(c), the magnitude of bias error is lowest for *PCO Sensicam* at 0.04 pixels followed by 0.05 pixels for *PCO 2000* with 200 mm focal length lens. And the the maximum magnitude of bias error is shown by *PCO 2000* with 100 mm lens at 0.12 pixels.

The amplitude of bias error as a function of relative aperture size is shown in Fig 6.3(d). The fitting line shows the general trend of bias error which was seen for all the three configurations. As expected, the bias error is low for $f_{\#} < 4$ because of spherical aberration. Again for $f_{\#} > 8$, the bias error starts to decrease because the diffraction limit of the lens is reached.

6.3.2 Random Error

The random error as function of sub-pixel displacement for the different camera and lens combinations for $f_{\#}$ of 5.6 are shown in Fig. 6.4(a), Fig. 6.4(b), Fig. 6.4(c). The random

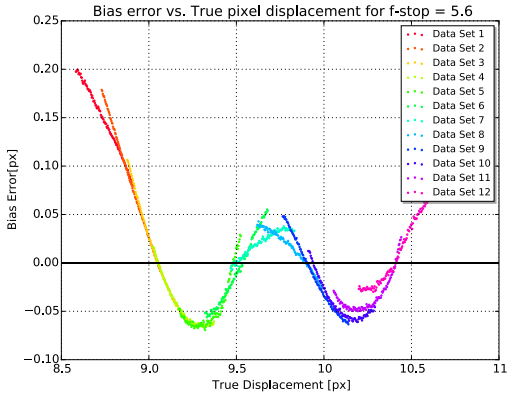

(a) *PCO 2000* (f= 200 mm) @ $f_{\#}$ = 5.6

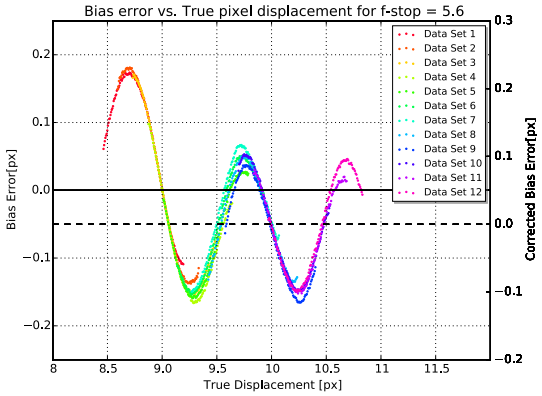

(b) *PCO 2000* (f= 100 mm) @ $f_{\#}$ = 5.6

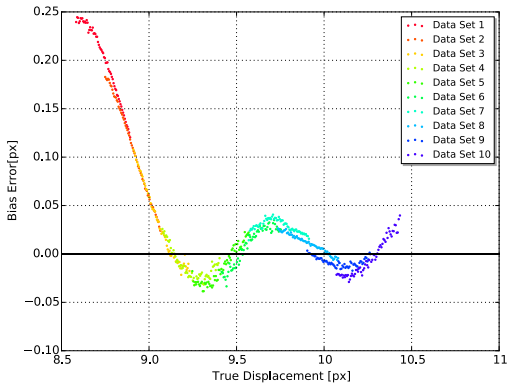

(c) *PCO Sensicam* (f= 100 mm) @ $f_{\#}$ = 5.6

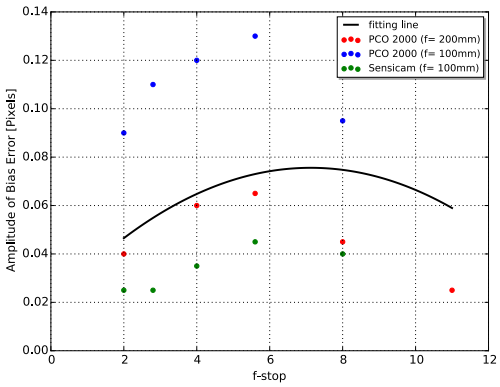

(d) Bias Error vs. $f_{\#}$

Figure 6.3: Bias Error for different camera settings

error is minimal towards the integer displacement values. The random error shows a periodic behaviour having oscillation with a periodicity of one pixel F. Scarano, M. L. Riethmuller (1999), it increases for 0 - 0.5 pixel displacement which is followed by a steady decline in the range 0.5 - 1 pixel. Each data set in the aforementioned figure represents the gradient of random error present over the entire image. In Fig. 6.4(a), Fig. 6.4(b) and Fig. 6.4(c), the magnitude of random error is lowest for *PCO 2000* with 200 mm focal length lens at 0.08 pixels, 0.1 pixels for *PCO 2000* with 100 mm focal length lens. The maximum magnitude of random error is shown by *PCO Sensicam* with 100 mm lens at 0.2 pixels.

The amplitude of random error as a function of $f_{\#}$ is shown in Fig. 6.4(d). It was observed that the random error is less for small $f_{\#}$ and increases significantly as the effect spherical aberration decreases. For higher $f_{\#}$ values, the random error again starts to decrease due to the diffraction limit of the lens.

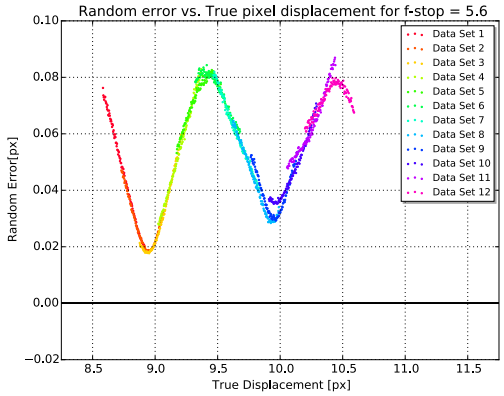

(a) *PCO 2000* (f= 200 mm) @ $f_{\#} = 5.6$

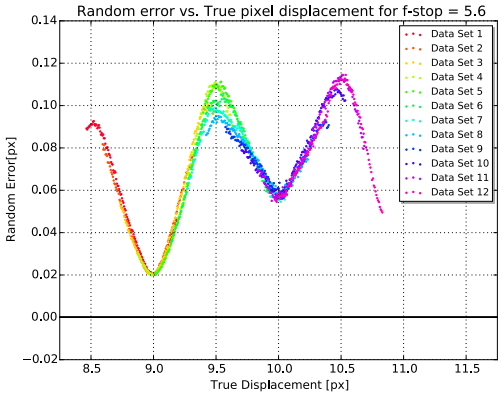

(b) *PCO 2000* (f= 100 mm) @ $f_{\#} = 5.6$

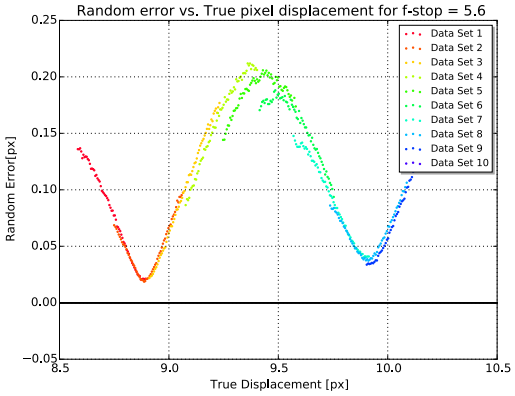

(c) *PCO Sensicam* (f= 100 mm) @ $f_{\#} = 5.6$

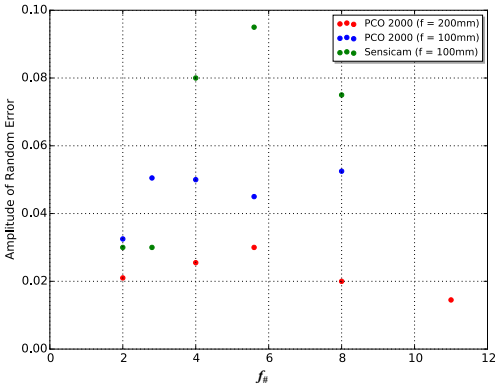

(d) Random Error vs. $f_{\#}$

Figure 6.4: Random Error for different camera settings

For interested readers, figures of the bias error and the random error as a function of sub-pixel displacement for various $f_{\#}$ for three different camera-lens setting is shown in Appendix A.

6.4 Discussion

Three different camera and lens combinations were used to determine the bias error and the random error shown in Fig. 6.3 and Fig. 6.4 respectively. In all the three cases, there was an unexpected behaviour of the bias error, the amplitude of the curve was slightly tilted away from the higher displacement values. This bias effect could be due to the slight variation of Δt while acquiring images. The aforementioned effect was removed from figures by rotating all the bias error values by a certain angle using the rotation matrix. Moreover, *Data Set 1*

and *Data Set 2* have a very high magnitude and does not represent the true nature of the amplitude of bias error. The reason for this effect is still unknown and requires more analysis. However, their effect on the magnitude of bias was not considered in making any conclusions. Fig. 6.3(d) shows that the magnitude of bias error for all the relative aperture was highest for *PCO 2000* with 100 mm lens because the particle image diameter was the smallest compared to other camera-lens combination at the same $f_{\#}$. The magnitude of bias error was lesser for *PCO 2000* with 200 mm lens because with higher focal length the digital image resolution increases when image distance and object distance is unchanged. The magnitude of bias error over the entire relative aperture range was least for *PCO Sensicam* because it has a pixel pitch of 6.45 μm compared to 7.4 μm of *PCO 2000*. With smaller pixel pitch the image resolution further improves and reduces the bias error due to peak-locking.

Smaller image particle diameter causes higher uncertainty in the location of particle with respect to the mean measured displacement which leads to higher random error. Since particle image size is smaller for *PCO 2000* with 100 mm lens ($d_\tau = 1.5$ pixels at $f_{\#} = 5.6$) compared to *PCO 2000* with 200 mm lens ($d_\tau = 1.8$ pixels at $f_{\#} = 5.6$), the random error is higher by 0.02 pixels for the former compared to the latter as shown in Fig. 6.4(b) and Fig. 6.4(a). Although the particle image diameter for *PCO Sensicam* ($d_\tau = 2$ pixels at $f_{\#} = 5.6$) is higher compared to *PCO 2000*, the random error is significantly higher for the former compared to the latter. On further investigation it was found out that the image density for *PCO Sensicam* was approximately 0.03 particles per pixels (ppp) compared to 0.11 ppp and 0.17 ppp for *PCO 2000* with 200 mm lens and 100 mm lens respectively.

6.5 Conclusion

This chapter gives a comprehensive account on the measurement errors for different relative aperture sizes. From Fig 6.3(d) and Fig 6.4(d), it can be concluded that $f_{\#}$ between 4 and 8 have the highest random and bias error. For $f_{\#} < 4$, error due to peak locking is less because spherical aberration effects are dominant. For $f_{\#} > 8$, the random and bias error gradually decreases because diffraction limit of the lens is reached. However, with smaller aperture size, the amount of light entering the camera sensor reduces which demands higher laser power to capture the position of the seeding particles. For 2D PIV setups, *f-stop* < 4 can be an ideal choice for experimentalists which will help them to keep the bias error and the random error minimal.

Chapter 7

Conclusion

A metaphysical conclusion is either a false conclusion or a concealed experimental conclusion.

Hermann von Helmholtz
(1821-1894)

The chapter contains a summary of the primary findings of the thesis and proposed future work for the continued development of the optical diffuser and PIV.

7.1 Properties of diffusers

An experimental analysis to see the the point spread function (PSF) width and the transmittance of no, one and two diffusers has been presented.

7.1.1 PSF width

The PSF width increases by 40% and 45% for one diffuser and two diffusers with 0° relative angle respectively compared to no diffusers for the entire range of the relative aperture sizes. It was noticed that change in relative angle of the diffusers had a significant effect on the particle image size. For two diffusers, $\phi = 30°$ and $150°$ have the largest PSF width with an increment of approximately 60% *w.r.t* no diffusers. This effect is due to more scattering of light by the diffusers on the camera image sensor.

7.1.2 Transmittance

The transmittance was studied to determine the amount of light passing through one and two diffusers. The results showed that throughout the visible light spectrum more than 95% of the light passes through one and two diffusers *w.r.t.* no diffusers. There was no change in the transmittance of diffusers in comparison with no diffusers for the wavelength of green light. Thus for the PIV experiments, the diffusers can be used without worrying about the transmissivity of the optical diffusers.

7.2 Advantages of using diffusers

Three experiments were done in different flow cases, namely uniform flow (empty test-section), high speed flow (wake of a 2D cylinder) and low speed flow (boundary layer of the test-section) with the aim to determine the reduction in peak locking errors. The major conclusion to drawn from these experiments were that there is a decrease in the magnitude of bias error by a factor of three for two diffusers ($\phi = 45°$) compared to no diffusers. Also, the magnitude of random error decreases by a factor of two - three for two diffusers.

7.2.1 Empty test-section

Since the particle image diameter was kept about 1 pixel in the empty test-section flow case, the peak locking error was the most dominant source of error in the vector flow field. The amplitude of bias error decreased by factor of two and three for one diffuser and two diffusers with relative angle (ϕ) of 0° respectively in comparison with no diffusers. Also, the amplitude of random error showed a reduction of almost a factor of three for two diffusers (ϕ= 0°) *w.r.t* no diffusers. Thus, showing that diffusers have a positive effect in reducing the measurement errors. The reduction in the bias error due to increase in particle image size concurred with the findings of J. Westerweel (2000). The RMS profile showed that the velocity fluctuates within the range of 0.15 to 0.17 pixels for no diffusers due to severe peak locking. The velocity fluctuation for one and two diffusers decreased to 0.13 pixels and 0.07 pixels respectively.

7.2.2 Wake of a 2D cylinder

Further investigation of diffusers were done on the fully-developed wake of a 2D cylinder because peak-locking is a major source of error in 3D turbulent flows. The decrease in the degree of peak locking is relatively less for one and two diffusers (ϕ=0°) compared to no diffusers. However, for two diffuser at $\phi = 30°$, the degree of peak locking significantly reduced from severe peak-locking (for no diffusers: C = 0.60) to a very mild peak-locking (C = 0.23). Later, it was notified by LaVision that the relative angle of 45° gives the best result in reducing the peak locking which concurred with our finding of lower peak locking at 30°

relative angle between the two diffusers. The RMS velocity profile for turbulent wake failed to show a clear indication of reduction in velocity fluctuation for two diffusers. This was due to the fact that there are higher flow velocity fluctuations of 2 - 3 pixels due to von Karman vortex sheet present in the fully developed turbulent wake of the cylinder which overshadows the peak locking velocity fluctuation of 0.5 pixels.

7.2.3 Boundary layer of the test-section floor

The experiment on the boundary layer of the test-section floor was conducted to have a test case where peak locking is the dominant error source with lower velocity fluctuations. Also, a comparative test was done for the two diffusers ($\phi = 45°$) and defocusing to check the significance of using the former over the latter. The degree of peak locking and random error for two diffuser ($\phi = 45°$) reduced by factor of approximately two compared to no diffuser. The conventional defocusing of the lens showed that the defocusing marginally reduces peak-locking but in turn increases random error because of enlarged particles as discussed by J. Westerweel (1997). The RMS velocity profile showed that velocity fluctuation for two diffuser ($\phi = 45°$) and for perfect defocusing is closest to the velocity fluctuations of the reference data. However, in practice getting the perfect defocusing of the lens is very difficult to achieve.

7.3 Measurement error due to peak locking without using diffusers

Additional experiment were carried out to see the effect of the random errors and bias errors for various $f_{\#}$ in a planar PIV setup using three different combination of CCD cameras and lenses. The three combinations used were *PCO 2000* with 100 mm lens, *PCO 2000* with 200 mm lens and *PCO Sensicam QE* with 100 mm lens. From the analysis it can be concluded that $f_{\#}$ between 4 and 8 have the highest random and bias error. For $f_{\#} < 4$, error due to peak locking is less because spherical aberration effects are dominant. For $f_{\#} > 8$, the random and bias error gradually decreases because diffraction limit of the lens is reached. However with smaller aperture size, the amount of light entering the camera sensor reduces which demands higher laser power to capture the position of the seeding particles. Thus, *f-stop* < 4 can be an ideal choice for experimentalists which will help them to keep the bias error and the random error minimal for 2D PIV setups.

7.4 Future work

The future development in increasing the accuracy of PIV by using diffusers are identified as following:

1. Different positioning of the diffuser between the lens and the camera image sensor can

be tried to see the best position for reducing the measurement errors in PIV. Also, one or both the diffusers can be flipped to see if they have any significant effect on the particle image diameter.

2. In stereoscopic PIV, the diffusers can be employed to the cameras to see the reduction in the measurement error. It would be interesting to see the effect of diffusers when images are re-sampled by mapping function for getting the three components of vector field.

3. Large scale PIV experiments in which the magnification factor are very small, the use of diffusers can be beneficial. An experiment can be performed with and without the optical diffusers to determine the reduction in the measurement error.

4. Throughout the present work, error estimation methods developed for 2D PIV were used to determine the measurement error. However, no such methods has been developed for tomographic PIV yet. Hence, error estimation methods for tomographic PIV needs to be developed for better end results and minimizing the measurement errors.

Bibliography

A. Eckstein and Pavlos P Vlachos. Digital particle image velocimetry (DPIV) robust phase correlation. *Measurement Science and Technology*, 20(5), 2009.

A. Sciacchitano. *Uncertainty Quantification in Particle Image Velocimetry and Advances in Time-Resolved Image and Data Analysis*. PhD thesis, Delft University of Technology, 2014.

A. Sciacchitano, Douglas R. Neal, Barton L. Smith, Scott O. Warner, Pavlos P. Vlachos, B. Wieneke and F. Scarano. Collaborative framework for PIV uncertainty quantification: comparative assessment of methods. *Measurement Science and Technology*, 26(7), 2015.

Amir A. Jalali, J. Rybarsyk, and E. Rogers. Thermal lensing analysis of TGG and its effect on beam quality. *Optical Society of America*, 21(11):13741–13747, 2013.

B. H. Timmins, Brandon W. Wilson, Barton L. Smith and Pavlos P. Valchos. A method for automatic estimation of instantaneous local uncertainty in particle image velocimetry. *Experiments in Fluids*, 53(4):1133–1147, 2012.

C. E. Willert. *The interaction of modulated vortex pairs with a free surface*. PhD thesis, California University, San Diego, 1992.

Christian J. Kahler , S. Scharnowski, C. Cierpka. On the resolution limit of digital particle image velocimetry. *Experiments in Fluids*, 52:1629–1639, 2012.

D. Jeon, M. Gharib. On the relationship between the vortex formation process and cylinder wake vortex patterns. *J. Fluid Mech.*, 519:161–181, 2004.

D. Michaelis, Douglas R. Neal and B. Wieneke. Peak-locking reduction for Particle Image Velocimetery. *11 Int Symposium on Particle Image Velocimetry*, 2015.

Douglas B. Murphy, Kenneth R. Spring , Thomas J. Fellers and Michael W. Davidson . Principles of Birefringence. http://www.microscopyu.com/techniques/polarized-light/principles-of-birefringence accessed on 10-08-2016, 2016.

E.F.J. Overmars, N.G.W. Warncke, C. Poelma and J. Westerweel. Bias errors in PIV: the pixel locking effect revisited. *15 International Symposium on Laser Techniques Applied to Fluid Mechanics*, 2010.

F. Scarano, L. David, M. Bsibsi, D. Calluaud. S-PIV comparative assessment: image dewarping+misalignment correction and pinhole+geometric back projection. *Measurement Science and Technology*, 39(2):257–266, 2005.

F. Scarano, M. L. Riethmuller. Advances in iterative multigrid PIV image processing. *Experiments in Fluids*, 29:51–60, 2000.

F. Scarano, M. L. Riethmuller. Iterative multigrid approach in PIV image processing with discrete window offset. *Experiments in Fluids*, 26(6):513–523, 1999.

G. I. Roth, J. Katz. Five techniques for increasing the speed and accuracy of PIV interrogation. *Measurement Science and Technology*, 12(3):238–245, 2000.

H. Huang, D. Dabiri and M. Gharib. On errors of digital particle image velocimetry. *Measurement science and technology*, 8(12):1427, 1997.

H. Nobach, E. Bodenschatz. Limitation of accuracy in PIV due to individual variations of particle image intensities. *Experiments in Fluids*, 47:27–38, 2009.

H. Nobach, N. Damaschke, C. Tropea. High-precision sub-pixel interpolation in particle image velocimetry image processing. *Experiments in Fluids*, 39(2):299–304, 2005.

H. T. Huang, H. E. Fiedler, J. J. Wang. Limitation and improvement of PIV, Part I: Limitation of conventional techniques due to deformation of particle image patterns. *Experiments in Fluids, Volume 15*, pages 168–174, 1993a.

H. T. Huang, H. E. Fiedler, J. J. Wang. Limitation and improvement of PIV, Part II: Particle image distortion, a novel technique. *Experiments in Fluids*, 15(4):263–273, 1993b.

J. Chen, J. Katz. Elimination of peak-locking error in PIV analysis using the correlation mapping method. *Measurement Science and Technology*, 16(8):1605–1618, 2005.

J. Westerweel. Effect of Sensor Geometry on the Performance of PIV interrogation. *Laser Techniques Applied to Fluid Mechanics*, pages 37–55, 2000.

J. Westerweel. Analysis of PIV interrogation with low-pixel resolution. *Optical Diagnostics in Fluid and Thermal Flow, 624*, pages 1–12, 1993a.

J. Westerweel. Fundamentals of Digital particle image velocimetry. *Measurement science and technology*, 8(12), 1997.

J. Westerweel. *Digital particle image velocimetry theory and application PhD Thesis*. PhD thesis, Technical University of Delft, 1993b.

J. Westerweel, D. Dabiri, M. Gharib. The effect of a discrete window offset on the accuracy of cross-correlation analysis of digital PIV recordings. *Experiments in Fluids*, 23:20–28, 1997.

Joseph W. Goodman. *Introduction to Fourier Optics*. THE McGRAW-HILL COMPANIES, INC., 1996.

K. T. Christensen. The influence of peak-locking errors on turbulence statistics computed from PIV ensembles. *Experiment in Fluids*, 36(3):484–497, 2004.

L. B. Fore. Reduction of peak-locking errors produced by Gaussian sub-pixel interpolation in cross-correlation digital particle image Velocimetry. *Measurement Science and Technology*, 21(3), 2010.

M. Megerle, V. Sick and David L. Reuss. Measurement of digital particle image velocimetry precision using electro-optically created particle-image displacements. *Measurment Science and Technology*, 13:997–1005, 2002.

M. Raffel, C. E. Willert, S. T. Wereley, J. Kompenhans. *Particle Image Velocimetry: a Practical Guide*. Springer, 2007.

MG Olsen, RJ Adrian. Out-of-focus effects on particle image visibility and correlation in microscopic particle image velocimetry. *Experiments in Fluids*, 29:166–174, 2000.

Murali R. Cholemari. Modelling and correction of peak-locking in digital PIV. *Experiments in Fluids*, 42(6):913–922, 2007.

Nancy Hall,NASA Official. Boundary Layers. https://www.grc.nasa.gov/www/k-12/airplane/boundlay.html, 2015. Online; accessed 19 April 2016.

O. Pust. PIV: Direct Cross-Correlation compared with FFT-based Cross-Correlation. *10th International Symposium Laser Techniques Applied to Fluid Mechanics*, 2000.

R. D. Keane and R. J. Adrian. Optimization of particle image velocimeters. I. Double pulsed systems. *Measurement Science and Technology*, 1(11):12021215, 1990.

R. Paschotta. Beam Radius. https://www.rp-photonics.com/beam_radius.html accessed on 05-08-2016, 2008a.

R. Paschotta. YLF lasers. https://www.rp-photonics.com/ylf_lasers.html accessed on 21-05-2016, 2008b.

Richard D. Keane and Ronald J. Adrian. Theory of cross-correlation analysis of PIV images. *Applied Scientific Research*, 49(3):197–215, 1992.

R.J. Hearst, B. Ganpathisubramani. Quantification and adjustment of pixel-locking in particle image velocimetry. *Experiments in Fluids*, 56(10):1–5, 2015.

Ronald J. Adrian. Dynamic range of velocity and spatial resolution of particle image velocimetry. *Measurement Science and Technology*, 8(12):1393–1398, 1997.

Ronald J. Adrian, J. Westerweel. *Particle Image Velocimetry*. Cambridge University Press, 2010.

S. Ahn and Jeffrey A. Fessler. Standard Errors of Mean, Variance, and Standard Deviation Estimators. https://web.eecs.umich.edu/~fessler/papers/files/tr/stderr.pdf accessed on 05-08-2016, 2003.

S. M. Soloff, R. J. Adrian and Z-C Liu. Distortion compensation for generalized stereoscopic particle image velocimetry. *Measurement Science and Technology*, 8(12):14411454, 1997.

Scot O. Warner. *Autocorrelation-Based Estimate of Particle Image Density in Particle Image Velocimetry*. PhD thesis, Utah Sate University, 2012.

T. Roesgen. Optimal subpixel interpolation in particle image velocimetry. *Experiment in Fluids*, 35(3):252–256, 2003.

Walter Frei. Boundary Layers. https://www.comsol.com/blogs/which-turbulence-model-should-choose-cfd-application/, 2013. Online; accessed 19 April 2016.

Appendix A

A.1 Effect of diffusers

In Chapter 4, the effects of no, one and two diffusers on the PSF width as a function of *f-stop* was discussed for 50 mm *focal length* lens. The effect of diffusers on PSF width was also tested for 35 mm *focal length* lens which is discussed in this section.

A.1.1 0/1/2 diffusers

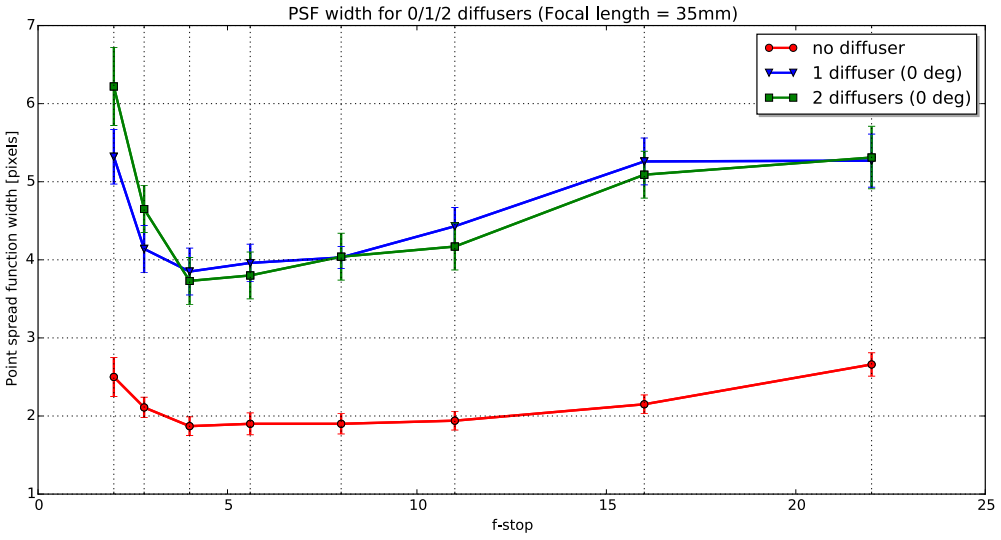

Figure A.1: PSF width vs. *f-stop* for 0/1/2 diffuser with standard uncertainty

The PSF width as a function of $f_{\#}$ for no, one and two diffusers with the 35 mm lens is shown in Fig. A.1. The PSF width first decreases until $f_{\#} = 4$ as result of reduced influence of spherical aberration. For $f_{\#}$ between 4 and 8, the PSF width is constant and again starts to gradually increase as a consequence of the diffraction limit of the lens is reached that

occurs for the smaller apertures (higher $f_{\#}$). The diffuser helps in better spreading of the light intensity on the image sensor which introduces slightly defocused particles. In case of one diffuser, there is a significant increase in the PSF width over the entire range of relative aperture sizes. For two diffuser ($\phi = 0°$), the PSF width is practically same as that of the one optical diffuser.

A.1.2 Relative rotation between two diffusers

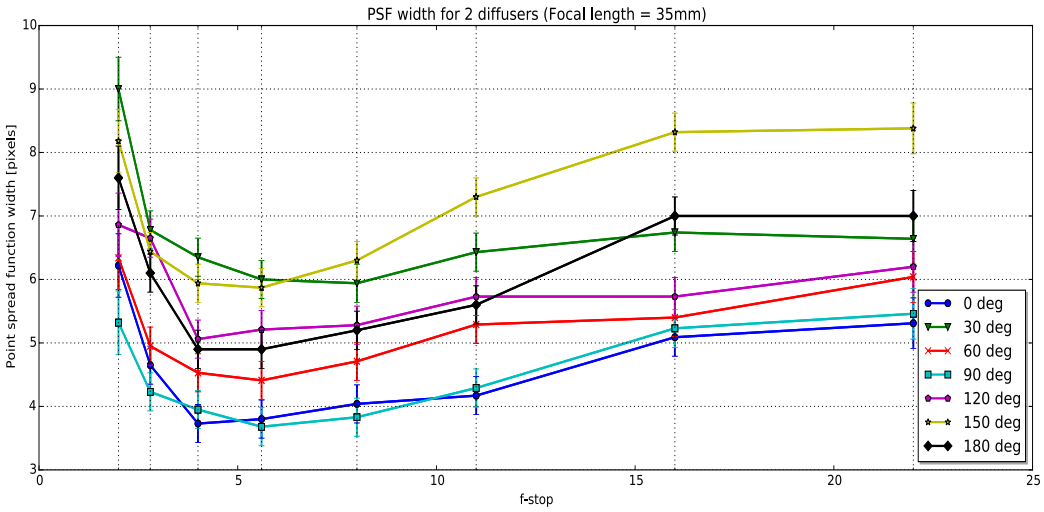

Figure A.2: PSF width vs. *f-stop* for two diffusers at different relative angles with standard uncertainty

The PSF width as a function of *f-stop* for different relative angles of two diffuser is shown in Fig. A.2. One diffuser was fixed at a position and the angle of second diffuser was varied from 0° to 180° in steps of 30° with respect to the optical axis of the first diffuser. The figure shows that change in the relative angle of diffusers have a significant effect on the PSF width. The PSF width over the entire range of $f_{\#}$ is least and maximum for the relative angle (ϕ) of 0° and 150° respectively. For $f_{\#} > 5.6$, the PSF width is higher for $\phi = 150°$ compared to 30°.

A.2 Measurement error due to peak locking

In Chapter 6, a comprehensive study has been presented to show the effect of the bias error and the random error in peak-locked data for various relative aperture sizes. Three different combinations of CCD cameras and lenses was used, namely *PCO 2000* with 200 mm lens, *PCO 2000* with 100 mm lens and *PCO Sensicam* with 100 mm lens. The results for above mentioned configuration are discussed hereafter.

A.2.1 Bias Error

The propagation of the bias error over the sub-pixel displacement for three different camera-lens settings are shown in this section. In all the three cases, there was an unexpected behaviour of the bias error, the amplitude of the curve was slightly tilted away from the higher displacement values. This bias effect could be due to slight variation of Δt during image acquisition and was removed by rotating all the bias error values by a certain angle using a rotation matrix. Also, *Data Set 1* and *Data Set 2* have a very high magnitude and does not represent the true nature of the amplitude of bias error. The reason for this effect is still unknown and requires more analysis. However, their effect on the magnitude of bias was not considered in making any conclusions.

PCO 2000 camera with 200 mm focal length lens

The bias error as a function of sub-pixel displacement for $f_{\#}$ values between 2 and 11 is shown in Fig. A.3. The camera used for this measurement was *PCO 2000* (CCD, 2048 $\times$ 2048 px^2, 14 bits, pixel pitch 7.4 μm) with a 200 mm focal length lens. The amplitude of bias error is low for $f_{\#} < 4$ because the particle image diameter is higher due to spherical aberration. For $f_{\#} > 8$, the bias error starts to decrease because the diffraction limit of the lens increases diffraction effect of the particle image diameter. The highest amplitude of the bias error was recorded for $f_{\#}$ of 5.6 and 8 at 0.5 pixels and 0.47 pixels respectively.

PCO 2000 camera with 100 mm focal length lens

The bias error as a function of sub-pixel displacement for *f-stops* values between 2 and 8 is shown in Fig. A.4. The *PCO 2000* camera with a 100 mm focal length lens was used. The amplitude of bias error is lower for $f_{\#} = 2$ and 8 at 0.08 pixels and 0.07 pixels respectively. For *f-stop* 2.8 and 4, the amplitude of bias error was maximum at 0.1 pixels approximately.

There is a clear offset in the graph, which might be due to incorrect calibration plate measurement. For visual reference a corrected bias error is plotted on the right-hand side Y-axis of the figures.

PCO Sensicam camera with 100 mm focal length lens

The bias error as a function of sub-pixel displacement for *f-stops* values between 2 and 8 is shown in Fig. A.5. The *PCO Sensicam QE* camera (CCD, 1376 $\times$ 1040 px^2, 12 bits, pixel pitch 6.45 μm) with a 100 mm focal length lens was used. The amplitude of bias error is 0.02 pixels for $f_{\#} \leq 2.8$. For $f_{\#}$ of 5.6 and 8, the amplitude of bias error was maximum at 0.04 pixels.

Similar to PC0 2000 with 100 mm lens test case, a clear offset was noticed and a corrected bias error axis was made for better visual reference.

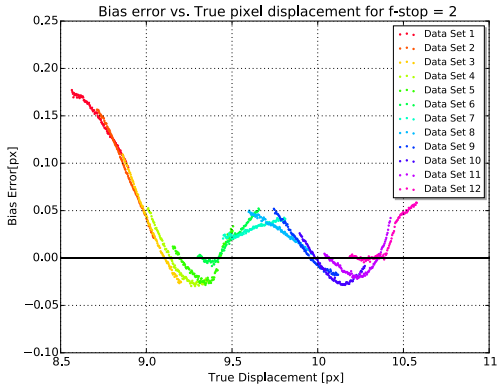

(a) *f-stop* = 2

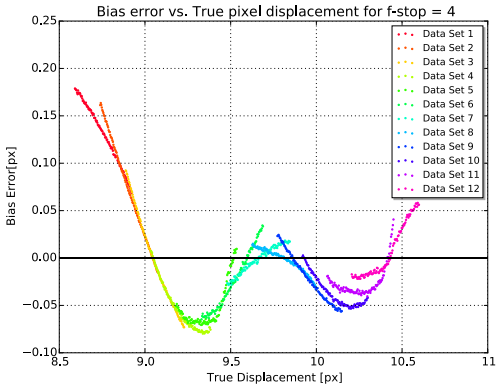

(b) *f-stop* = 4

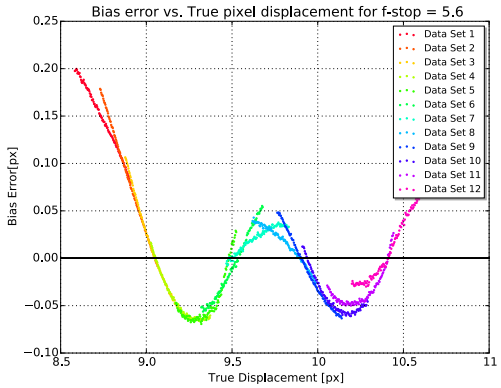

(c) *f-stop* = 5.6

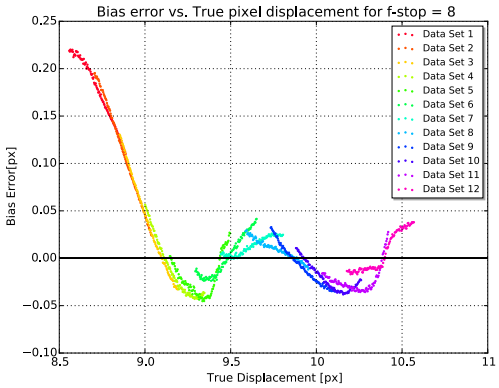

(d) *f-stop* = 8

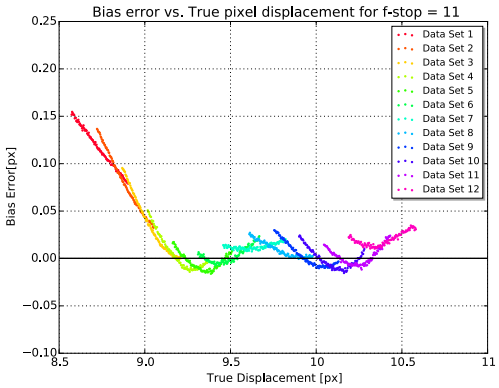

(e) *f-stop* = 11

Figure A.3: Bias Error for *PCO2000* with 200 mm lens

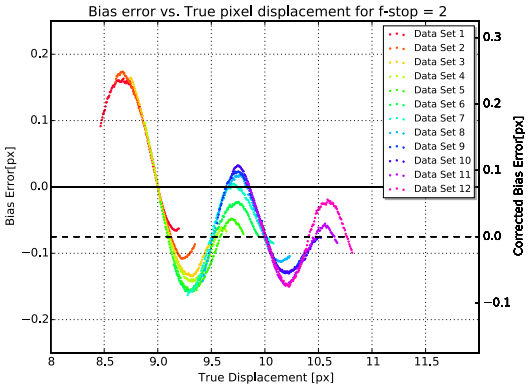

(a) *f-stop* = 2

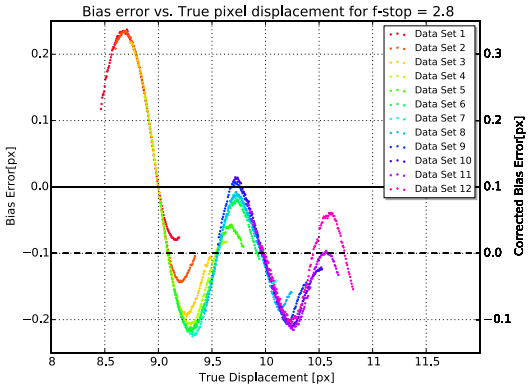

(b) *f-stop* = 2.8

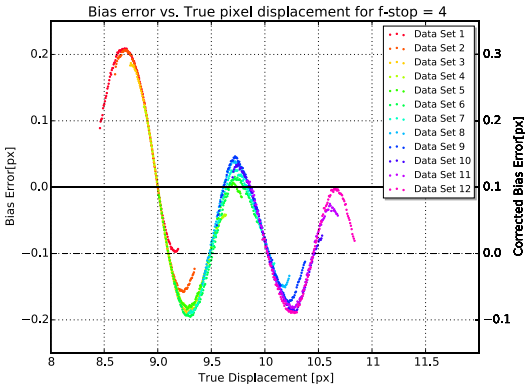

(c) *f-stop* = 4

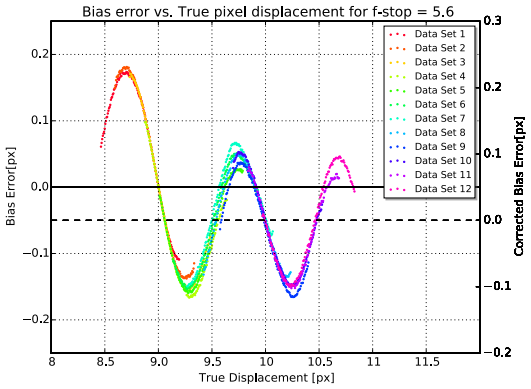

(d) *f-stop* = 5.6

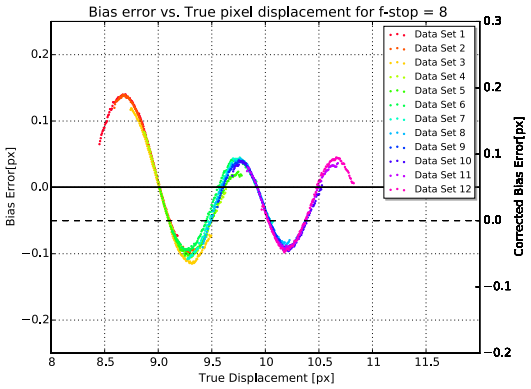

(e) *f-stop* = 8

Figure A.4: Bias Error for *PCO 2000* with 100 mm lens

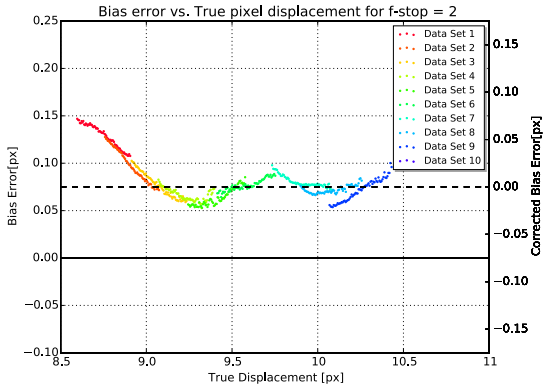

(a) *f-stop* = 2

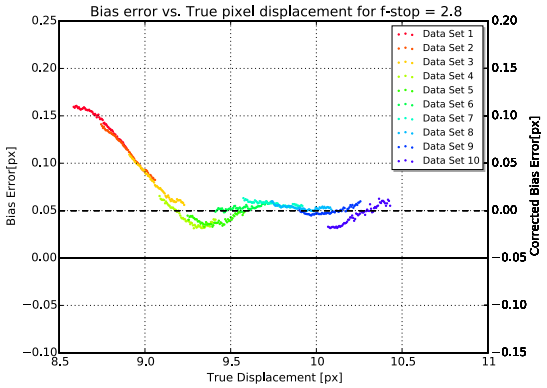

(b) *f-stop* = 2.8

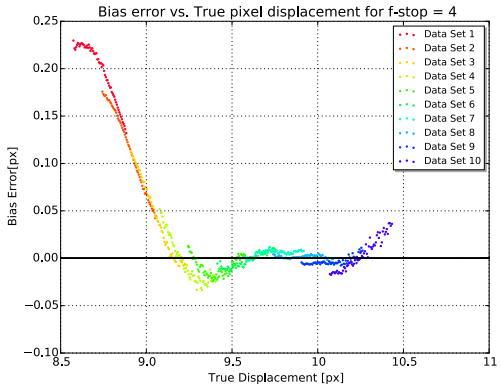

(c) *f-stop* = 4

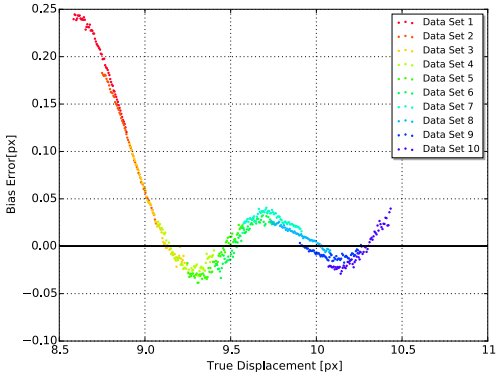

(d) *f-stop* = 5.6

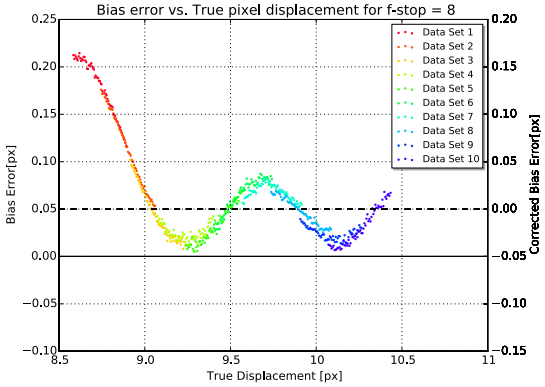

(e) *f-stop* = 8

Figure A.5: Bias Error for *PCO Sensicam* with 100 mm lens

A.2.2 Random Error

The random error effects on the three different camera-lens settings are as follows:

PCO 2000 camera with 200 mm focal length lens

The random error as function of sub-pixel displacement for $f_{\#}$ between 2 and 11 is shown in Fig. A.6. Each data set represents the nature of the random error present over the mean of vector field at a particular time separation. Due to reduced influence of spherical aberration the amplitude of random error increases from 0.06 pixels for $f_{\#}$ of 2 until 0.08 pixels for $f_{\#}$ of 5.6. For $f_{\#}$ of 8 and 11, the random error starts to decrease from 0.07 pixels to 0.05 pixels respectively due to the diffraction limit of the lens. For higher $f_{\#}$, the laser power should be high enough for the light to pass by through the small aperture size and into the image sensor to capture the scattered light from the seeding particles.

PCO 2000 camera with 100 mm focal length lens

The random error as function of sub-pixel displacement for *f-stop* between 2 and 8 is shown in Fig A.7. The amplitude of random error increases from 0.08 pixels to 0.12 pixels for $f_{\#}$ of 2 and 2.8 respectively. For $f_{\#} \geq 5.6$, the random error starts to decrease due to the diffraction limit of the lens is reached. In case of *f-stop* = 8, the random error for the data set 4 and 5 is approximately 0.13 pixels which might be due to some outliers in the data.

PCO Sensicam camera with 100 mm focal length lens

The random error as function of sub-pixel displacement for *f-stop* between 2 and 8 is shown in Fig A.8. The reduced influence of spherical aberration causes the amplitude of random error gradually increases from 0.08 pixels for $f_{\#} = 2$ up to 0.21 pixels for $f_{\#} = 5.6$. For *f-stop* $\geq$ 8, the random error starts to decrease due to the diffraction limit of the lens is reached. The magnitude of error because the image density for *PCO Sensicam* was approximately 0.03 particles per pixels (ppp) compared to 0.11 ppp and 0.17 ppp for *PCO 2000* with 200 mm lens and 100 mm lens respectively.

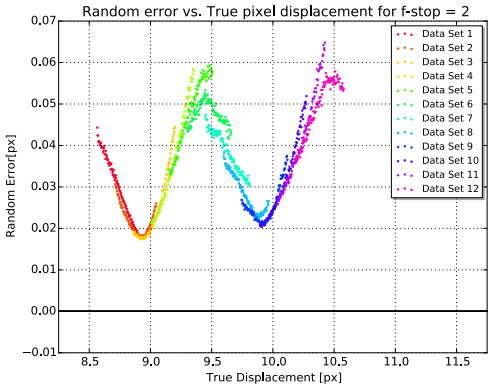

(a) *f-stop* = 2

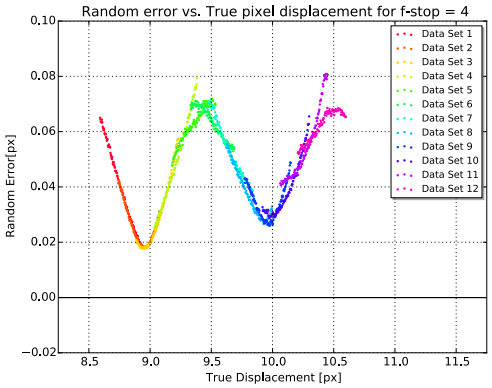

(b) *f-stop* = 4

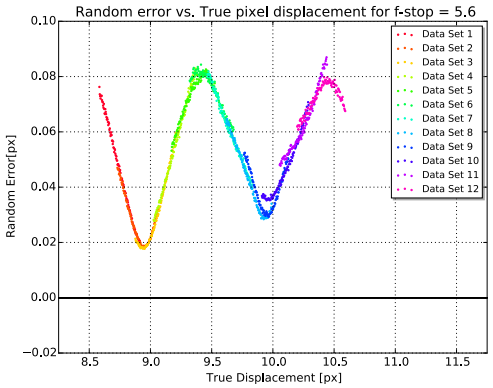

(c) *f-stop* = 5.6

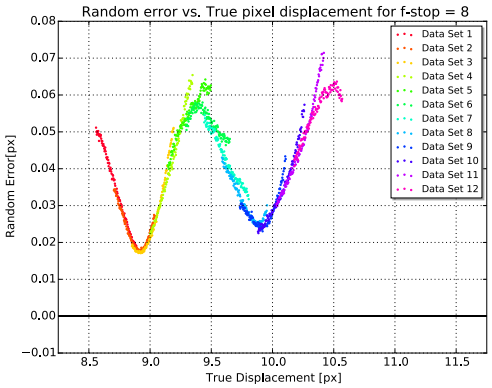

(d) *f-stop* = 8

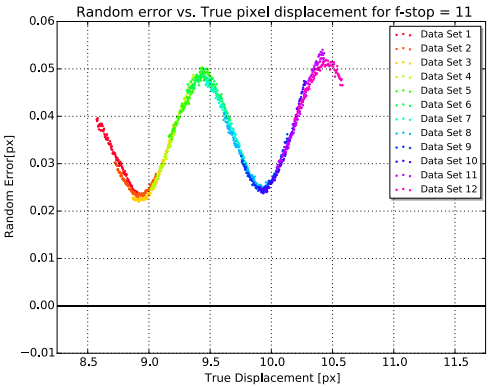

(e) *f-stop* = 11

Figure A.6: Random Error for *PCO 2000* with 200 mm lens

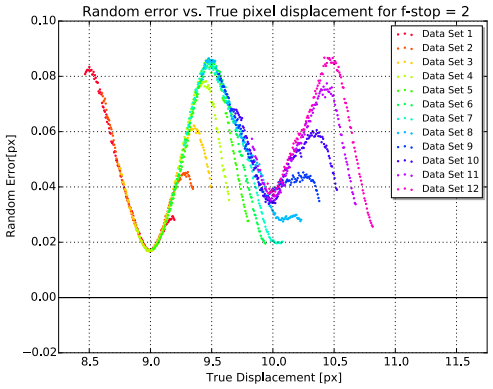

(a) *f-stop* = 2

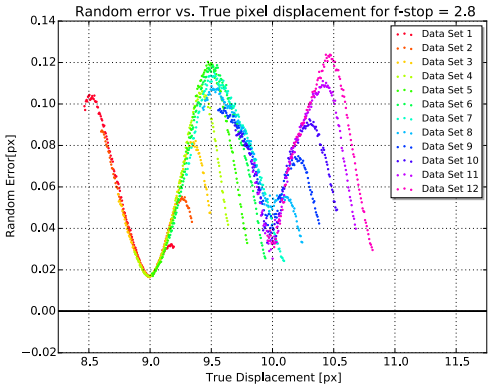

(b) *f-stop* = 2.8

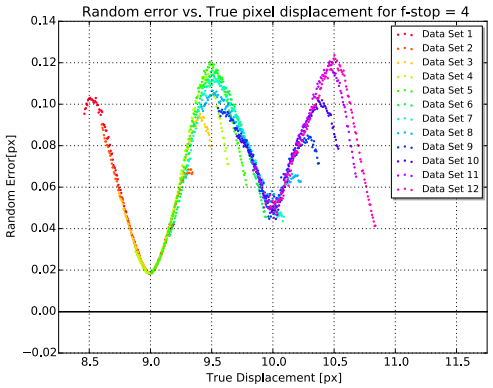

(c) *f-stop* = 4

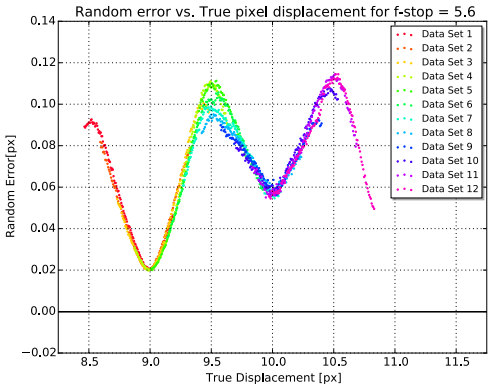

(d) *f-stop* = 5.6

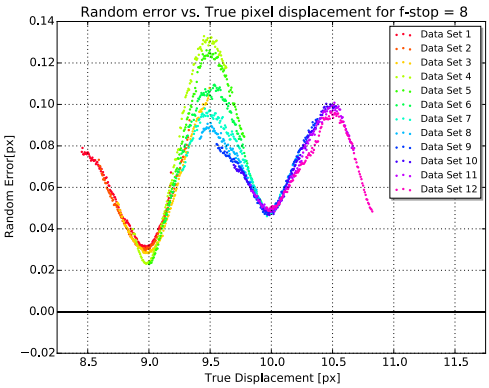

(e) *f-stop* = 8

Figure A.7: Random Error for *PCO 2000* with 100 mm lens

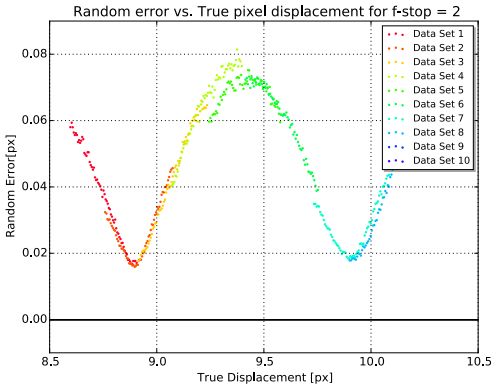

(a) *f-stop* = 2

(b) *f-stop* = 2.8

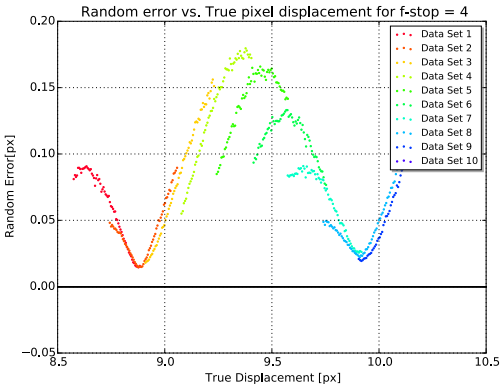

(c) *f-stop* = 4

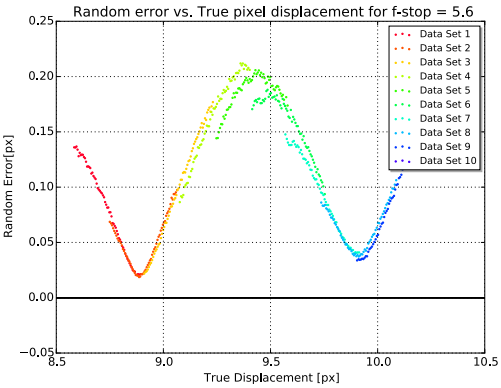

(d) *f-stop* = 5.6

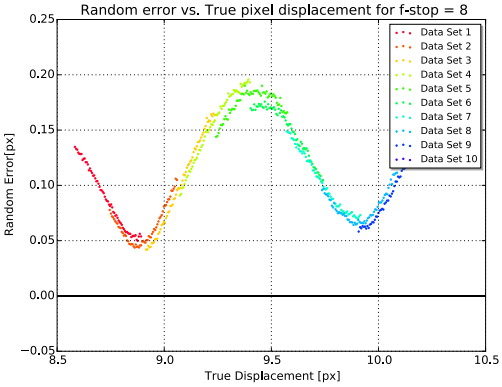

(e) *f-stop* = 8

Figure A.8: Random Error for *PCO Sensicam* with 100 mm lens